Opto-Electronic Technology

Terahertz imaging technology: progress and applications

Yuyuan Tian†, Xiaoyin Chen†, Zhuocheng Zhang†, Qianze Yan†, Yiming Liu, Chengliang Deng, Min Wan, Jiang Li, Xiaoqiuyan Zhang, Lu Rong*, Elizaveta Tsiplakova, Nikolay Petrov*, Xinke Wang*, Liguo Zhu*, Min Hu* and Yan Zhang*

https://doi.org/10.29026/oet.2026.250009

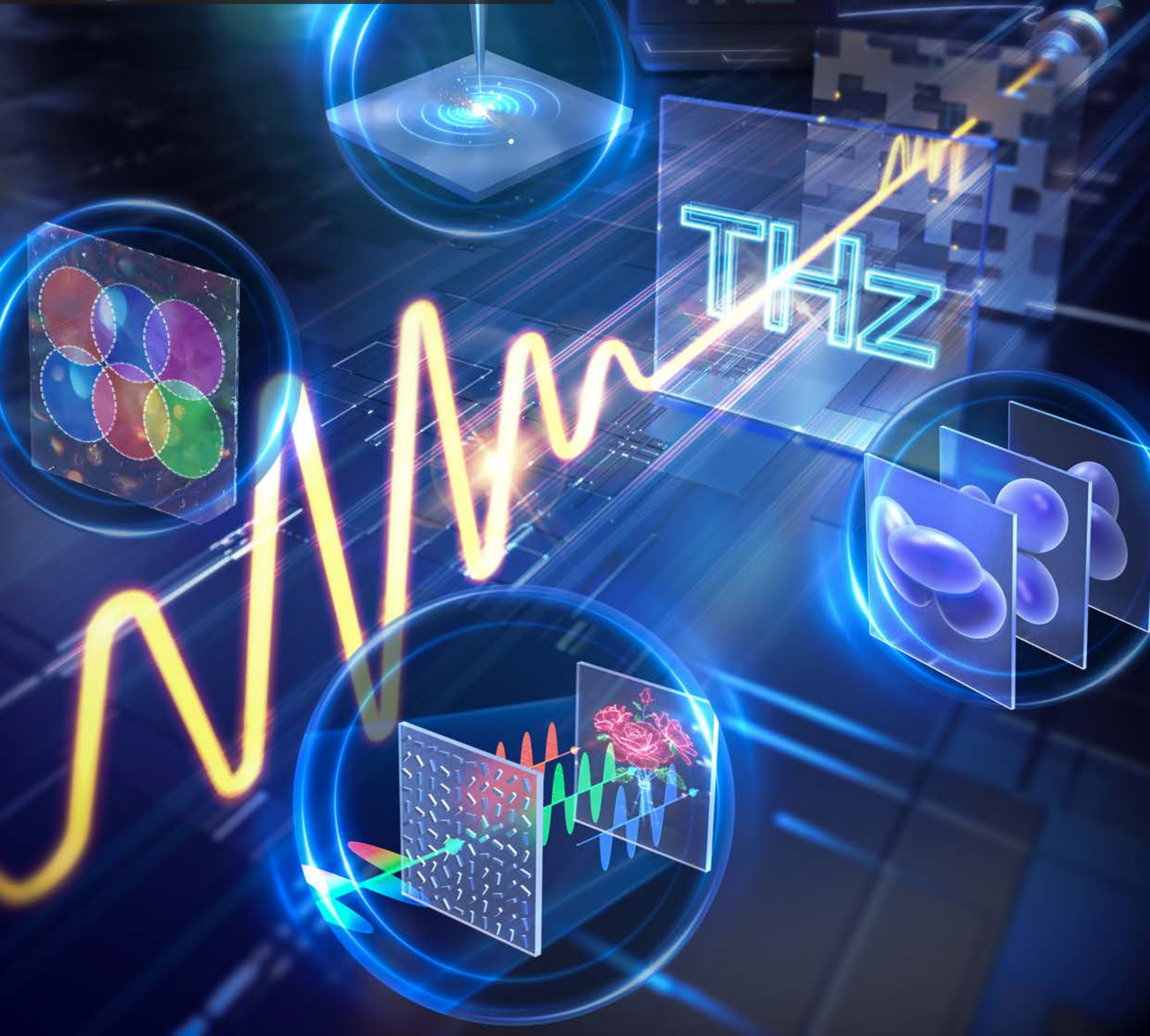

Opto-Electronic Technology

CN 51-1811/O4 ISSN (Print) 2097-6003 ISSN (Online) 2097-8006

Terahertz imaging technology: progress and applications

Yuyuan Tian, Xiaoyin Chen, Zhuocheng Zhang, Qianze Yan, Yiming Liu, Chengliang Deng, Min Wan, Jiang Li, Xiaoqiuyan Zhang, Lu Rong*, Elizaveta Tsiplakova, Nikolay Petrov*, Xinke Wang*, Liguo Zhu*, Min Hu* and Yan Zhang*

Citation: Tian YY, Chen XY, Zhang ZC, Yan QZ, Liu YM, Deng CL, Wan M, Li J, Zhang XQY, L Rong, Elizaveta T, N Petrov, XK Wang, LG Zhu, M Hu, Y Zhang. Terahertz imaging technology: progress and applications. *Opto-Electron Technol* **2**, 250009 (2026).

https://doi.org/10.29026/oet.2026.250009

Received: 1 November 2025; Accepted: 26 December 2025; Published online: 19 March 2026

Related articles

Physics and applications of terahertz metagratings

Shreeya Rane, Shriganesh Prabhu, Dibakar Roy Chowdhury

Opto-Electronic Science 2024, **3**(11): 230049 doi: 10.29026/oes.2024.230049

Efficient generation of vectorial terahertz beams using surface-wave excited metasurfaces

Zhuo Wang, Weikang Pan, Yu He et al

Opto-Electronic Science 2025, **4**(1): 240024 doi: 10.29026/oes.2025.240024

Terahertz active multi-channel vortices with parity symmetry breaking and near/far field multiplexing based on a dielectric-liquid crystal-plasmonic metadevice

Yiming Wang, Fei Fan, Huijun Zhao et al

Opto-Electronic Advances 2025, **8**(5): 240250 doi: 10.29026/oea.2025.240250

More related articles in Opto-Electronic Journals Group website

Opto-Electronic Technology

Review

March 2026, Vol. 2, No. 1

Open Access

Terahertz imaging technology: progress and applications

Yuyuan Tian[1†], Xiaoyin Chen[2,3†], Zhuocheng Zhang[4,5†], Qianze Yan[6†], Yiming Liu[1], Chengliang Deng[1], Min Wan[7,8], Jiang Li[2,9], Xiaoqiuyan Zhang[4,5], Lu Rong[1,10]*, Elizaveta Tsiplakova[11,12], Nikolay Petrov[11,13]*, Xinke Wang[6]*, Liguo Zhu[2,9]*, Min Hu[4,5]* and Yan Zhang[6]*

Abstract: Terahertz imaging, operating within the 0.1–10 THz frequency range, leverages unique properties such as non-ionizing radiation, sensitivity to polar molecules, and material-specific spectral fingerprints. This review comprehensively surveys major terahertz imaging modalities, highlighting significant progress and applications. Key methodologies, including continuous-wave holography, lensless ptychography, and computed tomography, provide quantitative phase contrast and three-dimensional structural information. Notably, terahertz pulse time-domain holography leverages the broadband nature of pulsed sources to achieve depth-resolved imaging through time-gated analysis. The development of focal-plane and single-pixel imaging addresses challenges related to detector availability, enabling high-speed and cost-effective systems. A major breakthrough is observed in near-field imaging, which surpasses the diffraction limit to achieve nanoscale resolution for probing materials, biomolecules, and plasmonic phenomena. While challenges in signal-to-noise ratio, hardware integration, and imaging speed persist, ongoing innovations in laser sources, algorithms, and system design are driving adoption in security, biomedicine, and industrial inspection.

Keywords: terahertz; imaging; continuous-wave; focal-plane; time-domain holography; single-pixel; near-field

DOI: 10.29026/oet.2026.250009 | CSTR: 32419.14.oet.2026.250009

Citation: Tian YY, Chen XY, Zhang ZC et al. Terahertz imaging technology: progress and applications. *Opto-Electron Technol* **2**, 250009 (2026).

1 Introduction

Since the publication of the first paper on terahertz imaging by Hu BB and Nuss MC in 1995[1], terahertz imaging technology has garnered extensive attention, with numerous works reviewing and summarizing progress in this field[2–7]. Terahertz radiation occupies the electromagnetic spectrum between 0.1–10 THz, with wavelengths ranging from 30 μm to 3 mm. Compared to adjacent infrared and microwave radiation, terahertz radiation exhibits several unique properties: 1) high sensitivity to polar molecules such as water and hydrated states, resulting in strong absorption, whereas non-polar materials like paper and wood show minimal absorption. This allows terahertz imaging of soft tissues to achieve a better signal-to-noise ratio than X-rays. 2) Low photon energy, which avoids ionization damage in biological tissues, making it safer for biomedical imaging. 3) The vibrational and rotational energy levels of many biological

Received: 1 November 2025

Accepted: 26 December 2025

Published online: 19 March 2026

[1]School of Physics and Optoelectronic Engineering, Beijing University of Technology, Beijing 100124, China; [2]Institute of Fluid Physics, China Academy of Engineering Physics, Mianyang 621900, China; [3]Department of Optics and Optical Engineering, University of Science and Technology of China, Hefei 230026, China; [4]Terahertz Research Center, School of Electronic Science and Engineering, University of Electronic Science and Technology of China, Chengdu 611731, China; [5]Terahertz Radiation and Application Key Laboratory of Sichuan Province, Chengdu 611731, China; [6]Beijing Key Laboratory of Metamaterials and Devices, Key Laboratory of Terahertz Optoelectronics of Ministry of Education, Department of Physics, Capital Normal University, Beijing 100048, China; [7]Department of Electrical Engineering, Eindhoven University of Technology, Eindhoven, Netherlands; [8]School of Electrical and Electronic Engineering, University College Dublin, Belfield, Dublin 4, Ireland; [9]Microsystem & Terahertz Research Center, China Academy of Engineering Physics, Chengdu 610200, China; [10]Beijing Engineering Research Center of Precision Measurement Technology and Instruments, Beijing 100124, China; [11]Digital and Display Holography Laboratory, ITMO University, Saint-Petersburg 197101, Russia; [12]Qingdao Innovation and Development Center, Harbin Engineering University, Qingdao 266000, China; [13]School of Physics, Harbin Institute of Technology, Harbin 150001, China.

†These authors contribute equally.

*Correspondence: L Rong, ronglu@bjut.edu.cn; N Petrov, n.petrov@itmo.ru; XK Wang, wxk82721@cnu.edu.cn; LG Zhu, zhuliguo@tsinghua.org.cn; M Hu, hu_m@uestc.edu.cn; Y Zhang, yzhang@cnu.edu.cn

macromolecules fall within the terahertz band, providing distinctive spectral fingerprints for material identification and even isomer discrimination. 4) Time-domain spectroscopy based on coherent detection captures the temporal electric field waveform of terahertz radiation. Fourier transformation yields both amplitude and phase information across frequencies, enabling determination of the sample's refractive index and absorption coefficient without relying on the Kramers-Kronig relations. These characteristics make terahertz imaging a vital tool in non-destructive testing, security screening, biomedical imaging, and cultural heritage preservation[8–11].

Figure 1 presents the timeline of several terahertz imaging approaches. The electronic methods for generating and detecting continuous terahertz radiation offer excellent stability and robustness. Using terahertz CCDs to capture field information, holograms can be acquired through interference techniques to reconstruct complex optical field information, or multiple measurements can be combined with algorithms to obtain complex field data and derive 3D information of samples. The team of Prof. Rong L at Beijing University of Technology has summarized advances in this field. Terahertz pulsed radiation can be generated via the interaction of ultrafast lasers with semiconductor materials. Employing electro-optic sampling methods, the temporal waveform of the terahertz electric field can be acquired,

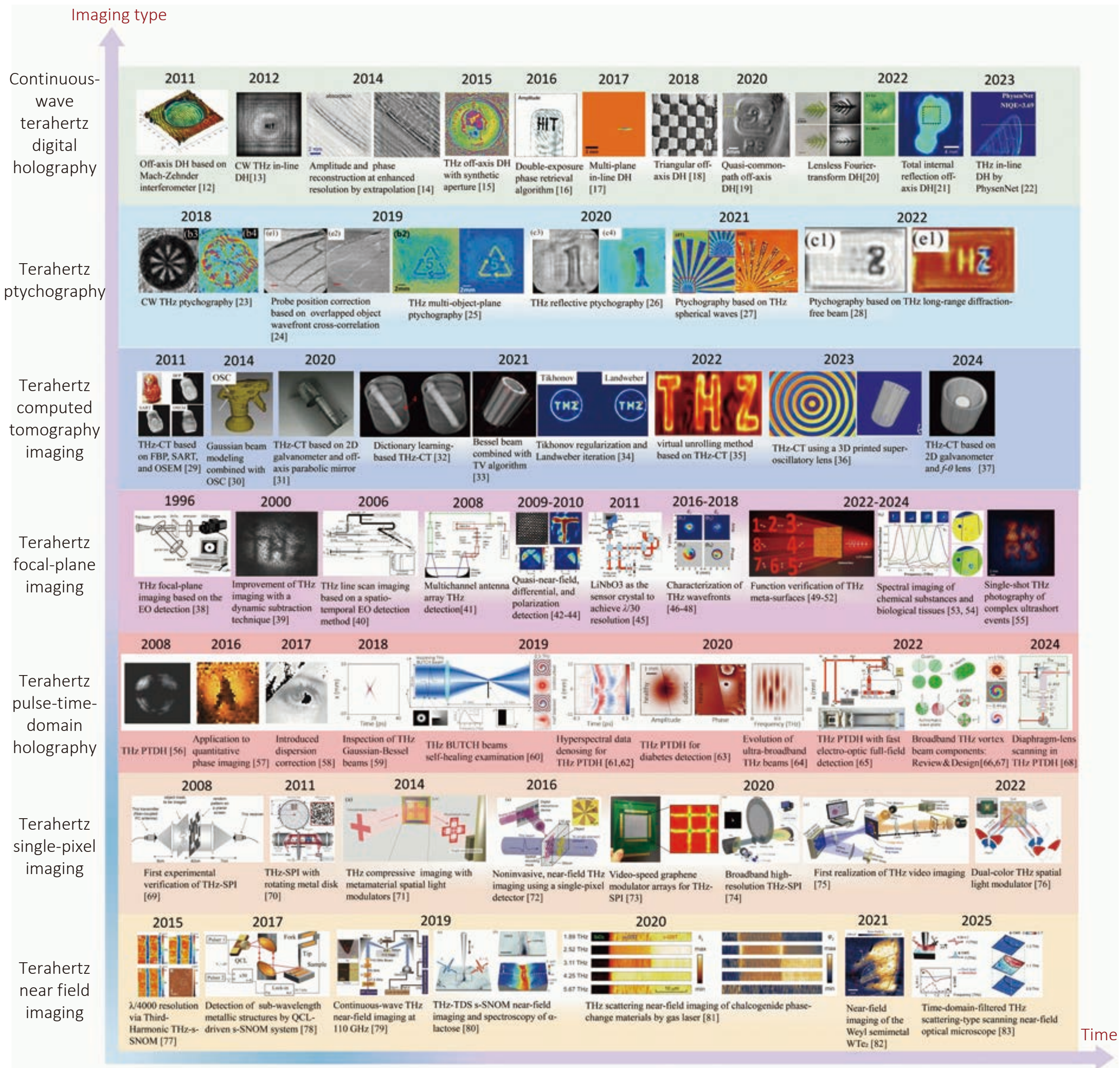

Fig. 1 | The timeline of terahertz imaging encompasses continuous-wave terahertz digital holography[12–22], terahertz ptychography[23–28], terahertz computed tomography[29–37], terahertz focal-plane imaging[38–55], terahertz pulse time-domain holography[56–68], terahertz single-pixel imaging[69–76], and terahertz near-field imaging[77–83].

enabling the extraction of amplitude and phase information across frequencies, and thus obtaining the distribution of the sample's refractive index and absorption coefficient. Prof. Wang XK's team at Capital Normal University has reviewed the development and applications of terahertz focal-plane imaging technology. Applying holographic wavefront propagation algorithms to the hyperspectral datasets, obtained in the temporal domain it is possible to study spatio-temporal dynamics of extremely short terahertz pulses. The team of Prof. Nikolay V. Petrov from ITMO University develops and reviewed the terahertz pulse time-domain holography. Due to the cost-performance limitations of terahertz sources and detectors, particularly array detectors, single-pixel imaging methods have been developed. These techniques modulate the terahertz optical field, use single-pixel detectors to capture signals, and employ compressed sensing algorithms to reconstruct images, achieving high-resolution terahertz imaging. Prof. Zhu LG from the China Academy of Engineering Physics has summarized the principles and implementation of terahertz single-pixel imaging technology and outlined its future directions. Breaking the diffraction limit in terahertz imaging, using near-field methods to obtain high-resolution images of samples along with spectral information, is highly significant for studying light-matter interactions with terahertz imaging technology. Prof. Hu M's team at the University of Electronic Science and Technology of China (UESTC) has reviewed the progress and applications of terahertz near-field imaging. Finally, future challenges and development opportunities of terahertz imaging technology are summarized and analyzed.

2 Continuous-wave terahertz imaging

2.1 Continuous-wave terahertz digital holography

Terahertz digital holography (TDH) imaging represents a significant application of terahertz waves. Digital holography involves two core processes: hologram recording and numerical reconstruction. The recording of digital holograms is accomplished by pyroelectric detector, which record the interference fringes of object light and reference light to generate digital holograms. Using computer-based diffraction propagation and numerical reconstruction techniques, it provides quantitative amplitude and phase information. It features full-field imaging, non-contact scanning, and real-time imaging, having achieved fruitful research results in biomedical imaging, non-destructive testing, and other fields[84–86].

2.1.1 In-line digital holography

In-line digital holography, also known as Gabor holography, features a common optical path for the reference and object beams[87]. This configuration maximizes the spatial-bandwidth product utilization of the detector, offering significant advantages in terms of optical simplicity and imaging efficiency. Continuous-wave terahertz in-line digital holography was demonstrated using a 2.52 THz source and a pyroelectric array detector (124 pixel×124 pixel, ~100 μm pitch)[88]. This setup enabled the imaging of a patterned sample on a dielectric substrate, achieving high-quality amplitude reconstructions with a lateral resolution of approximately 0.2 mm. However, these initial studies focused solely on amplitude imaging and did not retrieve phase information[88,89].

Phase retrieval is achieved through dedicated algorithms. Most phase retrieval algorithms impose constraints on the object plane, such as positive absorption[14], support constraint[90,91], spatial sparsity[92], or gradient-domain sparsity[93]. In addition, advanced denoising models[94] can also serve as constraints for the object plane to achieve high-fidelity reconstruction. Furthermore, advanced denoising models can be integrated as object-domain constraints to achieve high-fidelity reconstructions. Physics-enhanced

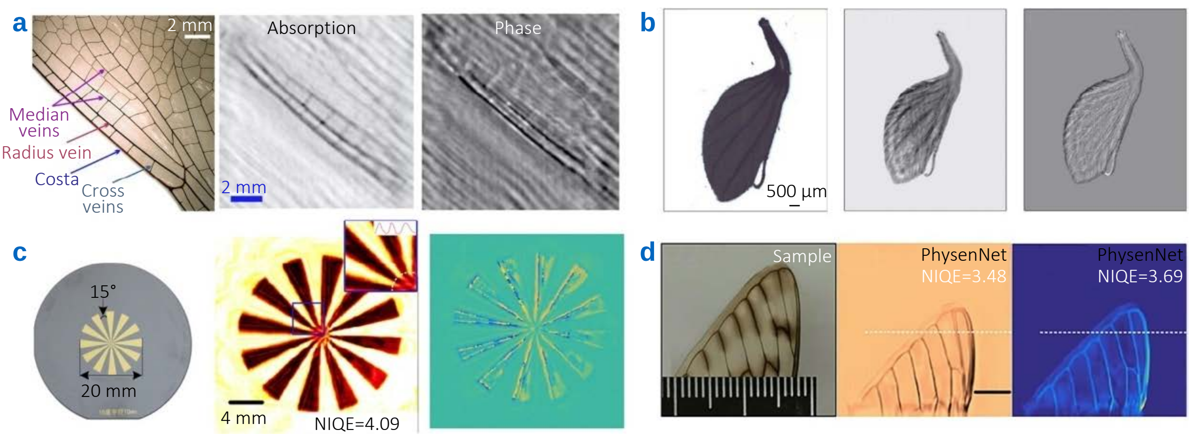

Fig. 2 | Reconstruction results of THz in-line digital holographic under various object-plane constraints, including object photos, amplitude distribution and phase distribution. (a) Positive absorption. (b) Spatial sparsity. (c) Denoising models. (d) Unconstrained neural network. Figure reproduced with permission from: (a) ref.[14], (b) ref.[92], under a Creative Commons Attribution License; (c) ref.[94], Elsevier; (d) ref.[22], under a Creative Commons Attribution License.

neural networks were also developed for phase retrieval, requiring neither extensive training data nor explicit constraints[22]. Figure 2 compares reconstruction results obtained under various object-plane constraints.

Multi distance iterative phase retrieval algorithms resolve phase distributions by recording intensity images at varying sample-to-detector distances and propagating optical fields iteratively between the object plane and multiple recording planes. This approach addresses scenarios involving absorptive samples or inhomogeneous backgrounds. Multi distance phase retrieval was first applied to terahertz digital holography using two systems: a 186 GHz millimeter-wave heterodyne setup and a 580 GHz source-detector configuration[95]. Experiments demonstrated successful amplitude and phase reconstruction of low-contrast biological samples and metallic objects by varying the detection distance. Subsequent work compared single-plane and dual-plane reconstruction algorithms[16]. Further research implemented multi distance recording across 27 detection planes to reconstruct phase images in reflection mode[96]. To overcome detector saturation from high-intensity reflections, a modified reconstruction algorithm was developed to accommodate dynamic range limitations[97]. The use of disordered wavefront propagation significantly improves multi-plane THz phase retrieval by ensuring high-contrast and high-resolution image reconstruction without the need for manual parameter tuning[98]. An extrapolation algorithm was developed to numerically extend the effective detector size through iterative wavefield propagation between object and recording planes[99,100]. This approach simultaneously retrieves object phase information and reconstructs higher-frequency components from digital holograms, yielding complex amplitude distributions with enhanced lateral resolution. This method was subsequently applied by multiple research groups[101−103], consistently achieving resolution improvements. Due to the non-isotropic resolution of rectangular detectors, diagonal directions exhibit superior resolution. By rotating the detector and combining high-resolution regions, reconstructed images with universally enhanced resolution can be obtained[104]. Beyond techniques that broaden the frequency spectrum for resolution enhancement, sub-pixel shifting[101,105] and synthetic aperture methods[106−108] constitute widely adopted alternative approaches.

Beyond advances in single-plane reconstruction, multi-plane TDH introduced autofocusing algorithms that autonomously optimized recording distances by evaluating reconstructed image clarity. These developments enable successful multi-planar object reconstruction through specialized evaluation metrics[17,109,110]. Recent innovations address multi-depth synchronization challenges through pre-propagation diffraction decomposition for artifact suppression, adaptive Otsu filtering, and automated target-merged reconstruction[111]. Complementary compressed sensing approaches enable twin-image suppression, multi-plane reconstruction, and parameter optimization for continuous samples[112,113].

2.1.2 Off-axis digital holography

Off-axis digital holography mitigates twin-image artifacts inherent in in-line configurations by introducing a reference beam. This spatial frequency shift separates twin images spectrally, eliminating background superposition and enhancing image contrast. Unlike in-line holography, it relaxes sample constraints—accommodating opaque, reflective, and three-dimensional specimens without requiring high transparency. However, this approach imposes an inherent resolution constraint. Transmission off-axis digital holography was first extended to the terahertz band using a 100 GHz source and single-point detector, but suboptimal results were obtained due to uneven beam distribution[114]. Subsequently, the imaging resolution of approximately 9 mm (3λ) was achieved for structured objects[115]. Subsequent systems employing 2.52 THz sources achieved 0.4 mm lateral resolution[116], with systematic analysis of recording parameters (distance range, reference beam mode, incident angle)[117]. Further optimization through zero-order diffraction suppression improved resolution to 0.245 mm[118]. Alternative approaches included mirror-less off-axis digital holographic imaging using 3D-printed diffractive optics, which enabled 0.1 THz holography without fringe processing[119], and inverse-problem frameworks jointly reconstructing object/reference fields via wavelet-domain sparsity regularization optimized with alternating direction method of multipliers algorithms[120].

The commercialization of miniaturized, high-power terahertz quantum cascade lasers (QCLs) accelerated their adoption in off-axis digital holography. In pioneering work, a 3 THz QCL system incorporating Lloyd's mirror geometry achieved 0.28 mm lateral resolution and 0.5 rad phase accuracy when used to image metallic and polypropylene samples[121]. Concurrent studies demonstrated reconstruction resolutions at 0.495 THz and 0.71 THz, achieving 3.1 cycles/mm and 4.3 cycles/mm respectively[122]. Alternative configurations were developed, including triangular interferometric setups for transmissive/reflective samples[123] and systems that achieved 1.7 μm depth resolution in plastic/silicon wafer characterization[18]. Hybrid in-line/off-axis approaches leveraged off-axis reconstructions as initial values for enhanced resolution[124]. Further innovation applied inverse-problem reconstruction with total variation regularization, which suppressed boundary artifacts while improving noise/undersampling tolerance[125].

Off-axis digital holography was first integrated with synthetic aperture techniques in the terahertz band to image reflective specimens, achieving 200 μm lateral resolution, 6 μm axial resolution, and 0.4 rad phase accuracy[15]. Subsequent developments introduced signal separation methods for recovering amplitude/phase distributions from obscured objects[126]. Concurrently, novel reconstruction algorithms employing Fourier-Hermite polynomial functions enhanced film thickness edge definition[127], while real-time video imaging methods accelerated reconstruction speeds tenfold at

250 μm resolution[128]. Further innovations included sparse-sampling hologram compression with digital mask speckle noise suppressing, validated through metallic coin topography detection[129], later extended via sub-pixel registration to enable non-destructive inspection of concealed structures[130]. Figure 3 shows the results of various terahertz off-axis digital holographic reconstruction samples.

Continuous-wave terahertz off-axis digital holography typically employs triangular configurations with beam-splitting optics used to separate object and reference beams. This conventional approach suffers from differential environmental disturbances (mechanical vibrations and air turbulence), which compromised optical path stability. To overcome this limitation, common-path geometries were developed. One implementation using Lloyd's mirror systematically investigated four resolution-critical parameters: object-detector distance, source spectral bandwidth, detector pixel pitch, and phase retrieval methodology[131]. Alternative designs adopt Fresnel mirror interferometers where angularly separated reflections generate off-axis holograms. Validation through resolution targets, biological specimens, and polymer materials confirmed both imaging fidelity and enhanced stability, the reconstruction results of the polymer material are shown in Fig. 4(a)[19]. Further innovation led to a Fresnel total internal reflection (TIR) prism architecture, establishing TIR-based terahertz holography. This advancement enables dynamic refractive index mapping in solid/liquid phases. The refractive index measurement results of a soybean wax droplet are shown in Fig. 4(b), which significantly expanding measurable sample diversity while providing new insights into spontaneous terahertz phenomena[21].

Michelson interferometric configurations have been implemented for phase-shift terahertz holography, where samples undergo controlled translation while recording sequential interference patterns. This approach achieves

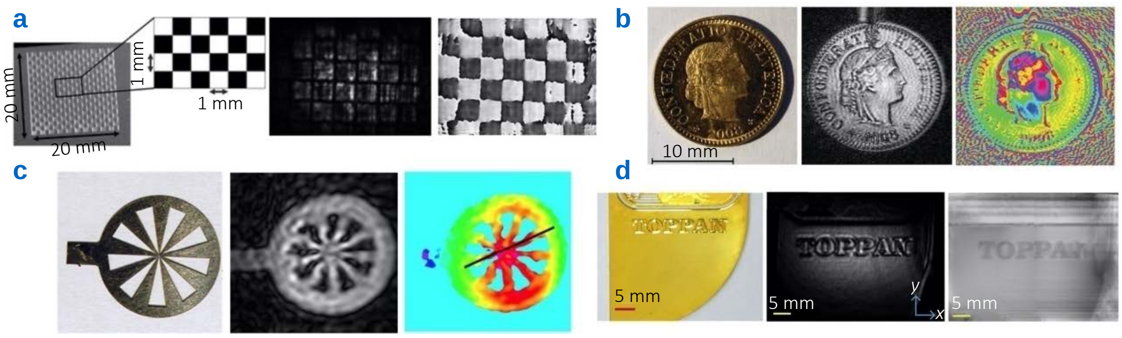

Fig. 3 | Reconstruction results of terahertz off-axis digital holographic imaging, including the object image, amplitude distribution and phase distribution. (a) Silicon sample with a checker pattern. (b) The coin. (c) Metallic resolution target. (d) Metallic bookmark. Figure reproduced with permission from: (a) ref.[18], Springer Nature; (b) ref.[15], (c) ref.[126], under a Creative Commons Attribution License; (d) ref.[130], SPIE.

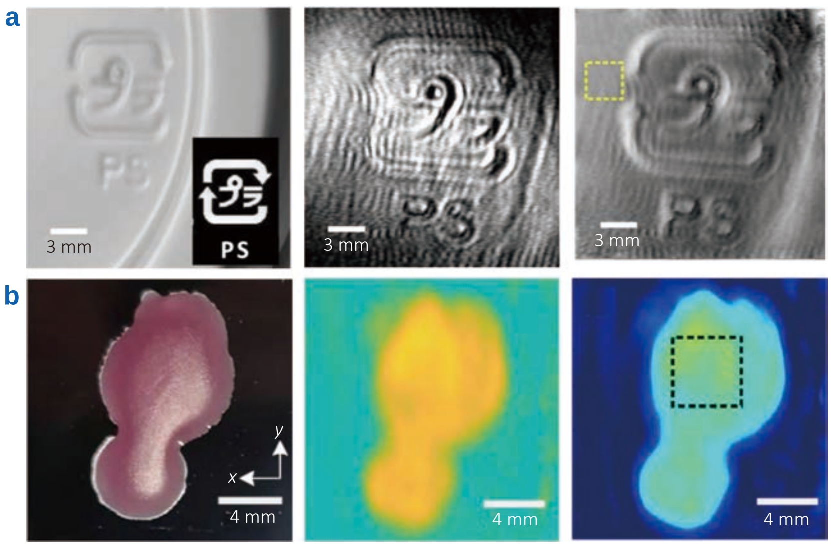

Fig. 4 | Reconstruction results of terahertz quasi-common-path off-axis digital holography and total internal reflection off-axis digital holography. (a) Amplitude and phase distribution of the polymer material. (b) Phase and refractive index distribution of a soybean wax droplet. Figure reproduced with permission from: (a) ref.[19], Optica Publishing Group; (b) ref.[21], under a Creative Commons Attribution License.

enhanced phase accuracy and suppresses stray reflections through complex amplitude reconstruction[132]. Concurrently, Mach-Zehnder interferometry demonstrated high-precision reconstruction of diverse samples including polymer plates and silicon wafers, revealing internal stress transformations in opaque materials[133]. Phase-shift methodologies advanced significantly with the introduction of two-step and four-step techniques. The two-step approach doubled reconstruction speed/contrast while reducing background noise fivefold compared to single-hologram methods, enabling bilayer sample imaging. The four-step technique proved superior for phase specimen reconstruction[134]. Comparative studies established phase-shifting holography's superior practicality and fidelity over off-axis methods when commercial terahertz systems were used[135]. This capability enabled real-time near-field mapping of polymer lens antennas at 290 GHz with ~1 Hz refresh rates, facilitating far-field pattern estimation[136].

Terahertz dual-wavelength digital holography utilizes distinct frequency sources for simultaneous sample imaging, enabling precise phase retrieval of complex surface structures and steep gradients. This approach was implemented in Michelson interferometric configurations to characterize continuously varying surfaces in polymeric specimens[137]. Mach-Zehnder implementations further demonstrate capabilities for quantitative metrology—resolving reconstruction ambiguities while enhancing resolution and suppressing coherent noise—to measure physical thickness, surface topography, and refractive index variations in metallic and dielectric samples[12]. Subsequent theoretical investigations established fundamental limitations of wavefront reconstruction via two-dimensional Fresnel transformation, identifying the sampling theorem as the primary constraint. Crucially, neglecting third- and higher-order terms in the Fresnel approximation maintains reconstruction fidelity even at minimal propagation distances[138].

2.1.3 Lensless Fourier-transform digital holography

Terahertz lensless Fourier-transform digital holography records the spatial frequency spectrum of object waves, enabling direct sample reconstruction through a single inverse Fourier transform of the captured hologram without requiring precise knowledge of the recording distance.

Figure 5 shows the schematic setup of terahertz lensless Fourier transform digital holography[20]. Similar to the triangular optical path commonly used in terahertz off-axis digital holography, this configuration replaced the mirror in the reference beam with an off-axis paraboloidal mirror, aligning the sample and focal point in the same plane. The two beams interfere on the detector to record the hologram. Employing this system, a Siemens star target was imaged, achieving a lateral resolution of approximately 346 μm in the diagonal direction. By applying sub-pixel image registration and stitching algorithms, the effective field of view was expanded from 18.3 mm to 44.2 mm, doubling the imaging area. Dynamic monitoring capabilities were demonstrated through 0.6 s interval capture of aquatic plant dehydration over 5 minutes, revealing rapid hydro morphological changes and providing novel insights into plant hydraulics. Subsequent refinements introduced tilt-correction to compensate non-parallel plane aberrations for reflective specimen[139]. Validation with metallized samples confirmed the efficacy of reflective lensless Fourier transform terahertz digital holography.

In summary, continuous-wave terahertz digital holography offers distinct advantages in biomedical sensing and non-destructive testing through non-contact, full-field imaging, and quantitative phase retrieval. Current advancements achieved submillimeter resolution (e.g., 0.1 mm in off-axis holography) and video-rate imaging (e.g., ~1 Hz refresh rate in phase-shifting holography), with enhanced stability and field-of-view via synthetic aperture, sub-pixel registration, and common-path geometries. Nevertheless, suppressing environmental disturbances, optimizing real-time phase retrieval algorithms, and integrating high-throughput detectors remain critical challenges. Future trends are expected to focus on adaptive reconstruction driven by deep learning, efficient synergy between

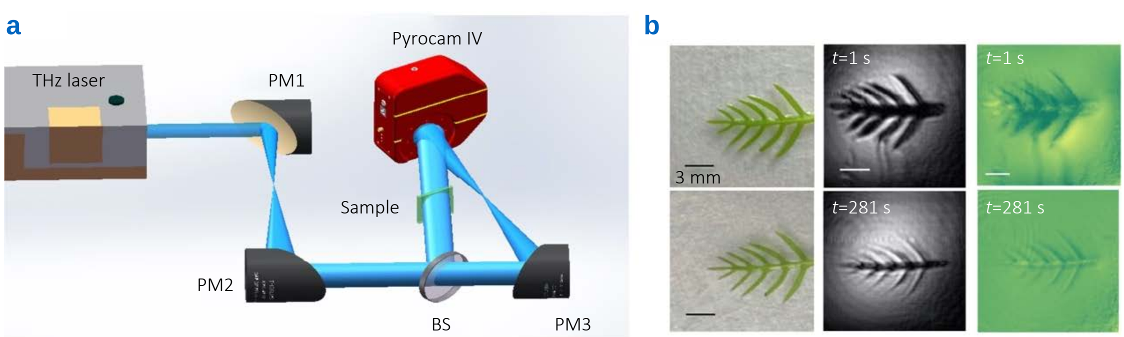

Fig. 5 | Experimental results of terahertz lensless Fourier-transform digital holography. (a) Schematic diagram of the experimental layout. (b) Photos, amplitude, and phase distributions of the aquatic leaf before and after dehydration. Figure reproduced with permission from ref.[20], under a Creative Commons Attribution License.

miniaturized QCLs and array detectors, and multi-modal integration (e.g., with tomography) for 3D dynamic monitoring, advancing applications in vivo diagnostics and industrial inline inspection.

2.2 Terahertz ptychography

2.2.1 Plane-wave terahertz ptychography

Compared with other terahertz imaging technologies, continuous wave terahertz ptychography is a lensless coherent diffraction imaging method with a large field of view and phase contrast. It can robustly retrieve the complex amplitude distribution of a sample from a set of diffraction patterns derived from overlapping sample illumination areas. Both the probe function and the transmittance function of the sample can be retrieved separately by the extended ptychographic iterative engine (ePIE) algorithm without the need for a reference beam. The terahertz ptychography system demonstrates advantages of a simple optical path, a compact structure, and full utilization of the spatial bandwidth product of the detector, and can perform scanning imaging on large-size samples.

In 2018, ETH Zurich (Swiss Federal Institute of Technology Zurich) successfully conducted the first ptychography experiment in the terahertz band[23]. A lensless ptychographic imaging system is constructed using an optically pumped continuous-wave terahertz laser with a wavelength corresponding to 3.1 THz and an area-array microbolometer. Both simulation and experiment are performed to reconstruct a Siemens star and a polypropylene ring, achieving a lateral resolution of 2λ and a longitudinal resolution of 0.03λ, respectively. Figure 6 shows the experimental optical path and results. In 2019, a continuous-wave terahertz ptychographic imaging system composed of a 2.52 THz far-infrared laser (FIRL) 295 and a Pyrocam III detector was applied to image the forewing of a cicada[24], as shown in Fig. 7. During the process of recording diffraction information, incorrect probe positions were found to severely affect the reconstruction quality. A probe position correction method based on cross-correlation registration of overlapping regions of the object wavefront is employed to minimize the translation error to 0.01 pixels. After correction, the subcostal vein and the first radial vein were easily distinguished. The measured optical thickness of the fourth meridian (R_4) is 9.30 μm.

Given the high penetrability of terahertz waves, which could also be applied to multi-object-plane ptychography. In 2020, Wang DY et al. pioneered the application of multi-object-plane ptychography in the terahertz band[25]. The 3D-ePIE algorithm was utilized to reconstruct the complex amplitude distributions of the object planes and the probe, effectively suppressing inter-layer crosstalk. An experimental system based on a 2.52 THz FIRL 295 continuous-wave laser and a PY-III pyroelectric area-array detector, as illustrated in Fig. 8(a), is employed for transmission ptychography of a two-layer polypropylene sample. Two control experiments are conducted with the front and rear sample sets being (S11, S2) and (S12, S2) respectively, as shown in Fig. 8(b). Figure 8(c) and 8(d) show the reconstructed amplitudes of the upper and lower layers of the sample, while Fig. 8(e) and 8(f) show their reconstructed phases. The numerical subscripts 1 and 2 represent the experimental

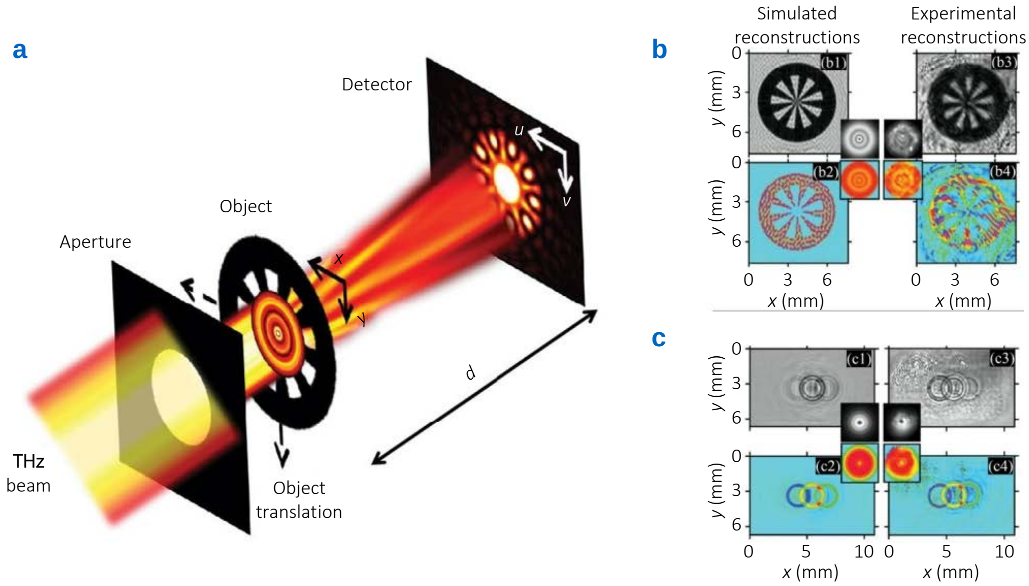

Fig. 6 | Continuous-wave terahertz ptychography. (a) Schematic experimental setup for transmission ptychography. (b, c) Simulated reconstructed: (b1, c1) amplitude and (b2, c2) phase. Experimentally reconstructed: (b3, c3) amplitude and (b4, c4) phase. Insets show the probe (top, amplitude; bottom, phase; left, simulation; right, experiment). Figure reproduced with permission from ref.[23], Optica Publishing Group.

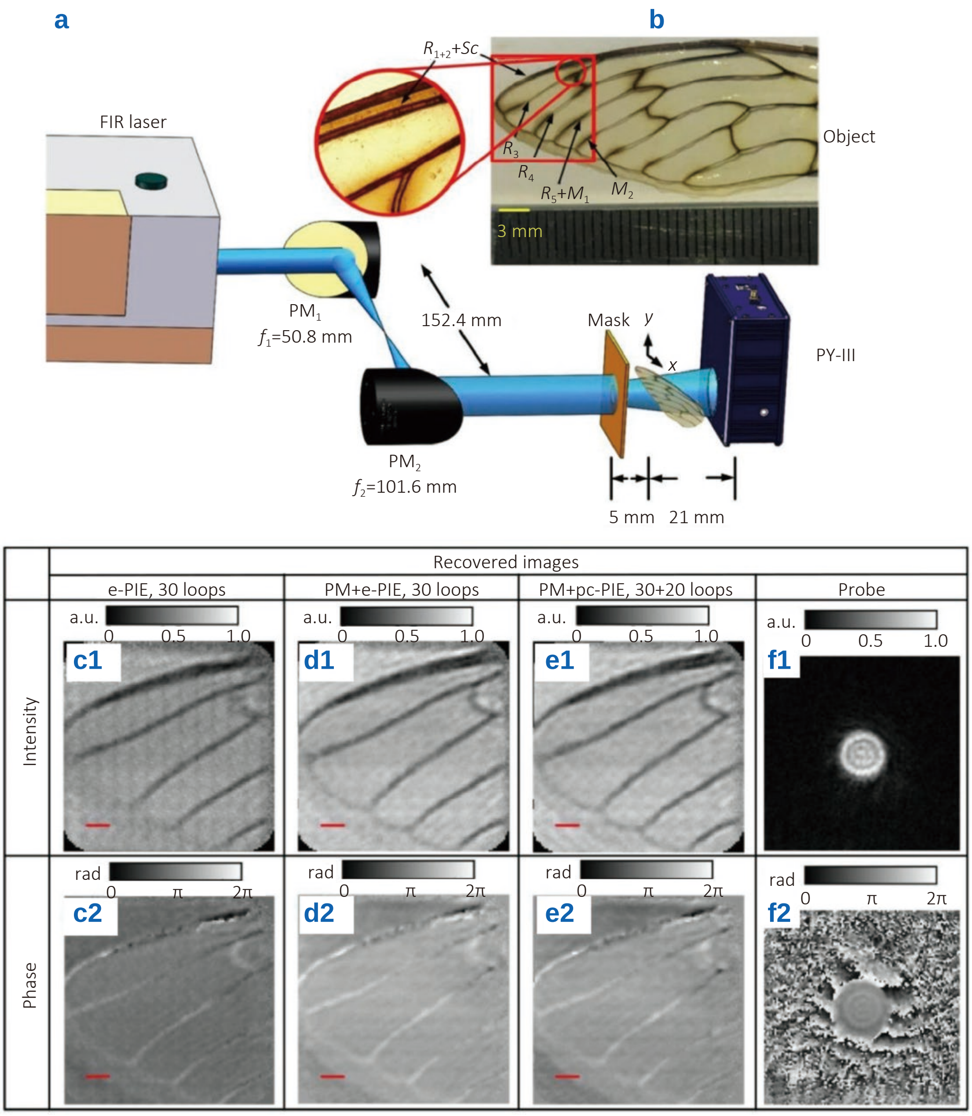

Fig. 7 | Probe position correction based on overlapped object wavefront cross-correlation for continuous-wave terahertz ptychography. (a) Optical path diagram of continuous-wave terahertz ptychography. (b) Cicada wing sample. (c–e) Terahertz ptychographic reconstruction result of the forewing of a cicada. (f) The reconstructed probe intensity and phase with position refinement. Scale bars: 1 mm. Figure reproduced with permission from ref.[24], under a Creative Commons Attribution License.

results of the two groups of samples (S11, S2) and (S12, S2) respectively. The results demonstrate that for samples with high terahertz transmittance, the phase reconstruction is more distinct. A comparison between the two experiments reveals that when the pattern of the first-layer sample contains more abundant detailed information, it induced a stronger diffraction effect. Consequently, the probe beam at the object plane where the second-layer sample is located is significantly expanded compared to that at the first object plane. The expansion of the probe beam area leads to an enlargement of the illuminated region of the second-layer object, thus resulting in a significantly larger reconstructed area of the second-layer object compared to the first-layer one. Additionally, the scattering effect of the first-layer object was found to eliminate the zero-order image in the diffraction pattern, thereby reducing the requirement for the dynamic range of the detector in the experiment.

Compared with terahertz transmissive ptychography, reflective ptychography is often used for imaging the surface of opaque samples. In 2020, Rong L et al. introduce reflective ptychography into the terahertz band[26], expanding the types of samples that can be imaged and achieving a greater measurement depth. Figure 9(a) shows the experimental setup for oblique-incidence reflective imaging, which adopts a FIRL 295 light source and a bolometer detector (Microxcam-384i-THz, INO). The diffraction patterns are corrected using the tilted plane correction algorithm, and then

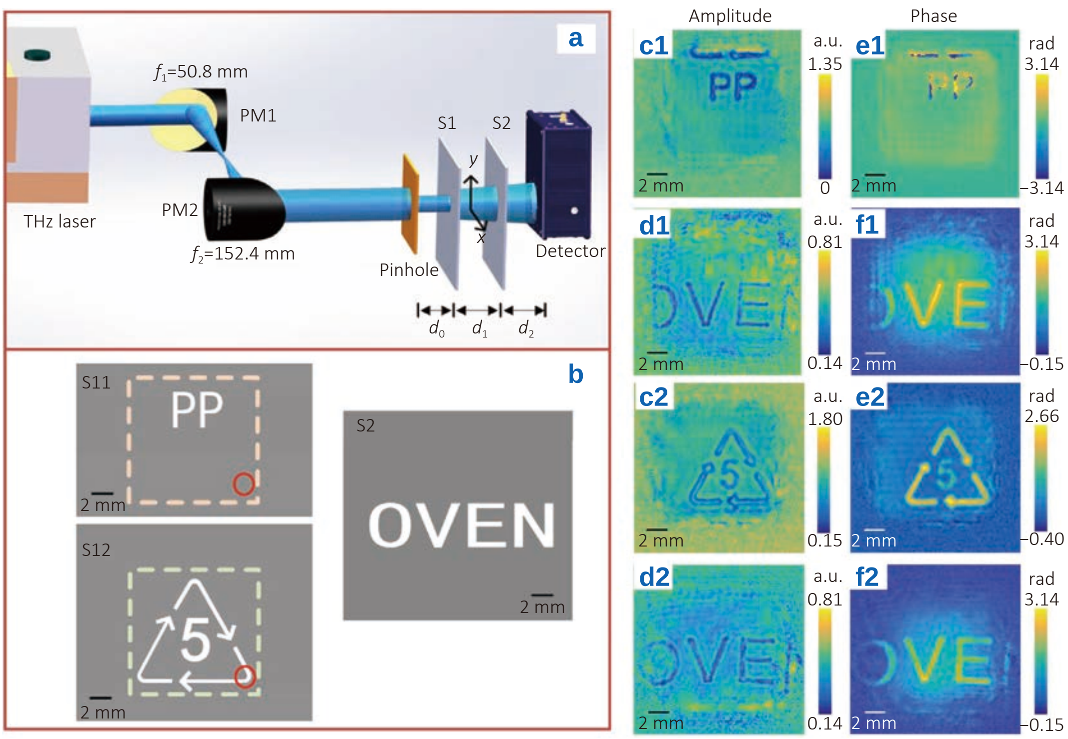

Fig. 8 | Multi-layered full-field phase imaging using continuous-wave terahertz ptychography. (a) Schematic diagram of the terahertz multi-object-plane ptychography system and samples. (b) First-layer sample S11 or S12, second layer sample S2. (c, d) Show the reconstruction amplitude results with the layers set to (S11, S2) and (S12, S2) respectively. (e, f) Represent the reconstructed phase results. Figure reproduced with permission from ref.[25], Optica Publishing Group.

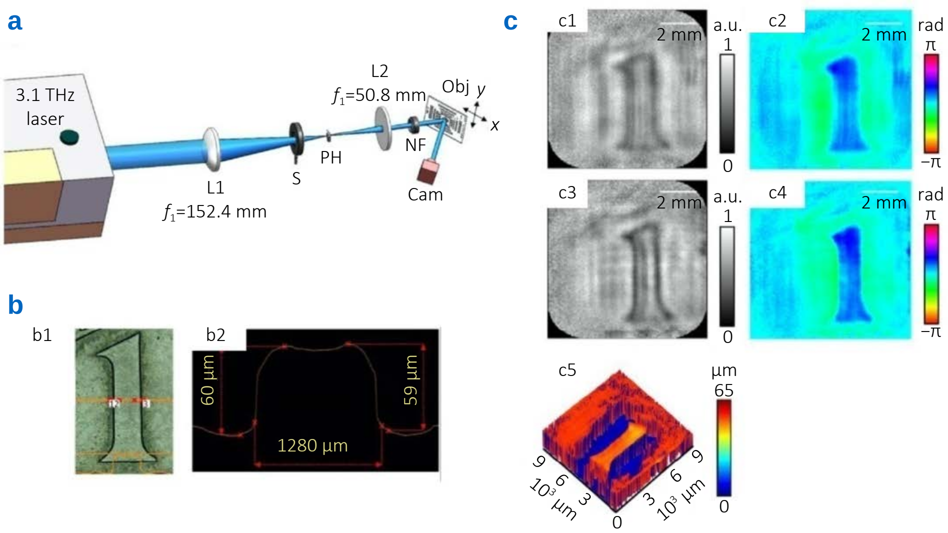

Fig. 9 | Terahertz reflective ptychography. (a) Experimental setup for CW-THz reflective ptychography. (b) Polish one-cent coin. (b1) The image of the illuminated area. The profile of the cutting line is given in (b2). (c1, c2) The reconstructed amplitude and phase images without tilted plane correction. (c3, c4) The reconstructed images after correction. (c5) The topography extracted from (c4). Figure reproduced with permission from ref.[26], Optica Publishing Group.

reconstructed using the ePIE algorithm. The object is exhibited in Fig. 9(b). Figure 9(c) presents the reconstruction result after 15 iterations. Figure 9(c1) and 9(c2) show the intensity and phase reconstructed using uncorrected diffraction patterns, respectively, with geometric distortion observed in the intensity image. Figure 9(c3) and 9(c4) display the reconstructed intensity and phase using corrected diffraction patterns, respectively, where the geometric compression is improved. The shortest width of the number "1" is compressed from 47 pixel to 38 pixel, which is closer to the true value. Figure 9(c5) is the 3D topography maps extracted from Fig. 9(c4) with tilted plane correction. By selecting the central area of the number and its left-right symmetric areas, the average height difference is calculated to be (59±1) μm. The depth value is not significantly different from the actual value, verifying the feasibility of the method.

2.2.2 Spherical-wave terahertz ptychography

In ptychography, the diversity of the probe's amplitude or phase can improve the quality of image reconstruction. Currently, ptychographic probes in the continuous terahertz waveband are generated either by-passing plane waves through small apertures or by collimating and beam-shrinking plane waves using two lenses, which results in significant energy loss. To enhance the signal-to-noise ratio of diffraction patterns, divergent spherical waves can be employed as probe beams. In ptychography, the theoretical resolution of ptychography based on a divergent spherical wave probe is $\lambda/(2\sin(\theta+\alpha))$, which is higher than that of the plane wave probe ($\lambda/(2\sin\theta)$).

In 2021, Rong L et al. conducted a comparative study of plane-wave and spherical-wave imaging on a cluster of cladodes of asparagus fern (scientific name: Asparagus setaceus) using divergent spherical waves[27], as shown in Fig. 10. Figure 10(a) is a schematic diagram of ptychographic imaging with divergent spherical waves. A plane wave is focused by a lens and then diverges again at the focal point to form spherical wave illumination. The diffraction pattern generated when the sample is illuminated by a plane-wave probe is presented in Fig. 10(b3). Corresponding to the same scanning probe position, Fig. 10(b4) shows the diffraction pattern using a divergent spherical wave as the probe. A comparison between two figures reveals that Fig. 10(b4) has a higher absolute intensity value and a wider distribution range. The intensity values at the dashed positions in Fig. 10(b3) and 10(b4) are extracted, as shown in Fig. 10(b2), where the red dashed line represents the intensity curve of the diffraction pattern under plane-wave illumination, and the blue solid line represents the corresponding curve under

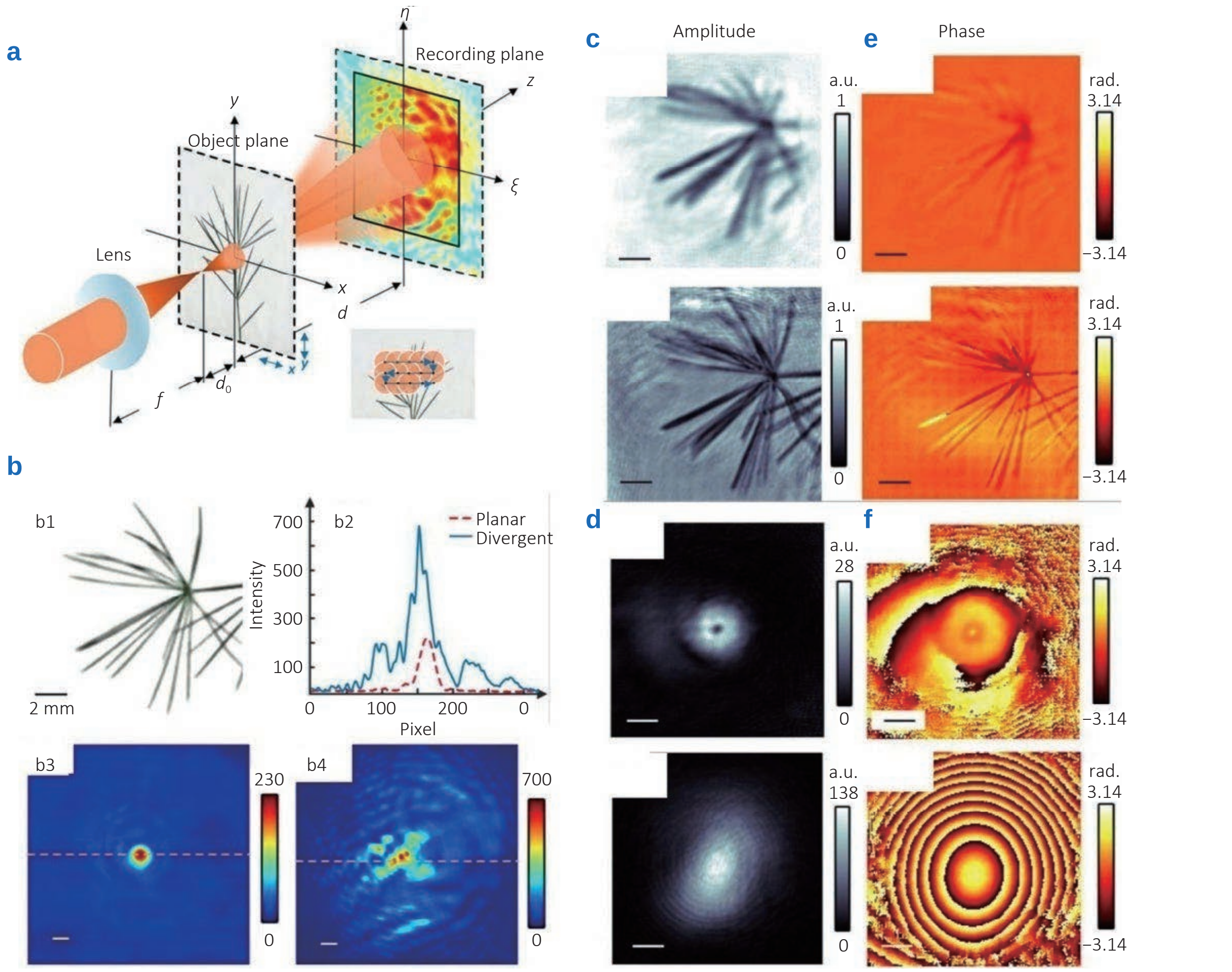

Fig. 10 | Terahertz ptychography using divergent spherical probe. (a) Schematic diagram of ptychography using divergent spherical probe. (b1) Imaging area of Asparagus setaceus; (b3) and (b4) terahertz diffraction patterns at the 13th probe position when the sample is illuminated by plane-wave and divergent spherical-wave probes, the profile of the cutting line is given in (b2), respectively. (c, d) Reconstructed amplitudes of the sample and probe. (e, f) Their reconstructed phases. Subscripts 1 and 2 denote plane and divergent spherical wave illumination, respectively. Scale bars: 2 mm. Figure reproduced with permission from ref.[27], Elsevier.

divergent spherical-wave illumination. Since the small aperture generating the probe can transmit more energy when the spherical wave is incident, it can be seen that the absolute intensity value of the diffraction pattern under divergent spherical-wave illumination is 2.8 times that under plane-wave illumination, indicating an improvement in energy utilization efficiency. As shown in Fig. 10(c) and 10(d) are the reconstructed amplitudes of the sample and the probe, while Fig. 10(e) and 10(f) are the reconstructed phases. The subscript 1 indicates illumination with a plane wave, and 2 indicates illumination with a divergent spherical wave. It can be seen from the reconstruction results that under the illumination of the divergent spherical wave, more details of the sample can be distinguished with higher resolution. Under divergent spherical-wave illumination, the beam energy is scattered to a larger area of the recording plane, which enhances the intensity distribution of high-order diffraction information and improves the signal-to-noise ratio of high-frequency information. In addition, based on the ePIE algorithm, the team proposed an extrapolated EE-PIE algorithm, which not only improves the resolution of the reconstructed image but also expands the effective size of the reconstructed image.

2.2.3 Terahertz ptychography with special beams as probes

In traditional ptychography, the probe beam controls the position and size of the light spot on the sample surface through a small aperture. Although the divergent spherical wave behind the aperture can be used to increase high-frequency spatial components, the light flux in this case is very low. Long-range diffraction-free beams (DFBs) are similar to Airy beams behind small apertures, featuring a main lobe with high intensity and a series of divergent side lobes, thus making DFBs suitable as probes. The following discussion focuses on the imaging performance of this beam for phase samples. In 2022, Xiang FD et al.[28] performed ptychographic imaging of a phase sample using a long-distance DFBs, where the phase object is a 5-mm-thick polypropylene plate with three uppercase letters "THZ" fabricated at different depths, specifically 0.75 mm for "T", 1.5 mm for "H", and 3 mm for "Z". As shown in Fig. 11(a), a

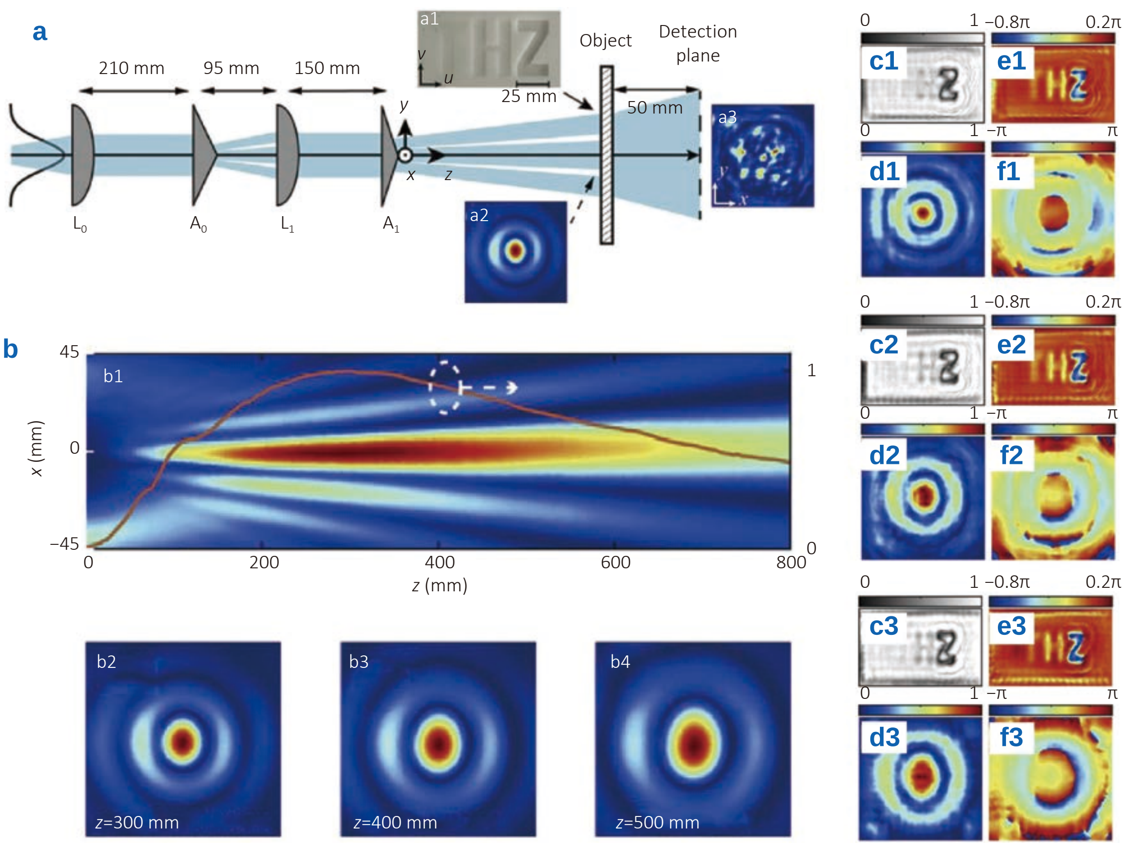

Fig. 11 | Terahertz ptychography using a long-distance diffraction-free probe. (a) Schematic of terahertz transmission ptychography with long-distance DFB. (a1–a3) The sample, probe, and diffraction pattern, respectively. (b1–b4) The intensity distributions of the *x*-*z* cross-section and *x*-*y* cross-sections of DFBs at three different *z* positions, respectively. (c, d) The reconstructed amplitudes of the sample and probe. (e, f) Their reconstructed phases. The subscripts (1, 2, 3) correspond to the reconstruction results at *z* positions of 300 mm, 400 mm, and 500 mm, respectively. Figure reproduced with permission from ref.[28], Optica Publishing Group.

long-distance DFBs can be generated by cascading two sets of lens-pyramid lenses. The following discussion focuses on the imaging performance of this beam for phase samples. The phase object is a 5-mm-thick polypropylene plate with three uppercase letters "THZ" fabricated at different depths, specifically 0.75 mm for "T", 1.5 mm for "H", and 3 mm for "Z". Figures 11(c–f) shows the reconstruction results of the sample at z = 300 mm, 400 mm, and 500 mm, respectively[28]. The quality of the reconstructed images at these three positions is almost identical, indicating that DFBs can extend the depth of field in ptychography.

Another common type of special beam is the Pearcey beam. In the terahertz band, there is currently no spatial light modulator (SLM) suitable for generating Pearcey beams. Therefore, quasi-Pearcey beams are usually generated using a parabolic slit plate and a Fourier transform lens[140]. The parabolic slit plate is placed at the front focal plane of the lens, where p is the parabolic parameter. The notched depths of the letters "THZ" in the sample used by the team are 0.57 mm, 1.14 mm, and 2.29 mm, respectively. As shown in Fig. 12(a), in the experiment, a parabolic amplitude modulation slit plate with a parameter p=0.5 was selected. The generated Pearcy beam self-focuses at 100 mm from the Fourier transform (FT) lens. The sample was placed at this position for ptychographic scanning. Figure 12(b) and 12(c) shows the slit shapes under three p parameters, and the x-z cross-sectional intensity distributions of the generated Pearcy beams are presented in Fig. 12(c). The smaller the parameter p, the shorter the distance between the slits, and the stronger the double-slit diffraction effect, with two bright stripes visible. The reconstruction results of the phase sample are shown in Fig. 12(d), where both the amplitude and phase can be successfully reconstructed.

Terahertz ptychography combines the characteristics of the terahertz waveband with the large-field-of-view and high-resolution phase reconstruction technology of ptychography, emerging as a promising approach in label-free in vivo medical imaging. As a computational imaging system, it is necessary to integrate various components of the system to enhance imaging capabilities. There is significant room for innovation in aspects such as coded illumination, algorithm optimization, and research on bolometer detectors. It can also be combined with deep learning to achieve automatic system optimization and high-speed dynamic imaging, as well as with optical coherence tomography for depth-resolved volumetric imaging. Currently, the pursuit of imaging technology focuses on higher speed, higher resolution, and larger field of view. Although terahertz ptychography has not garnered the same level of research attention as ptychography in the short-wave bands such as X-ray and extreme ultraviolet, the integration of ptychography technology undoubtedly marks a promising beginning, supported by the growing demand for terahertz wave imaging in industrial and medical fields.

2.3 Terahertz computed tomography imaging

Terahertz computational tomography (THz-CT) is based on the Fourier central slice theorem and linear propagation model. By recording intensity data at different projection angles and using reconstruction algorithms such as filtered back projection, it obtains the three-dimensional absorption coefficient distribution and internal/external structural information of samples. Developments in devices have led to diverse illumination modes, configurations, and algorithms, with applications in cultural relics protection and non-destructive testing, focusing on improving reconstruction quality, resolution, and data efficiency.

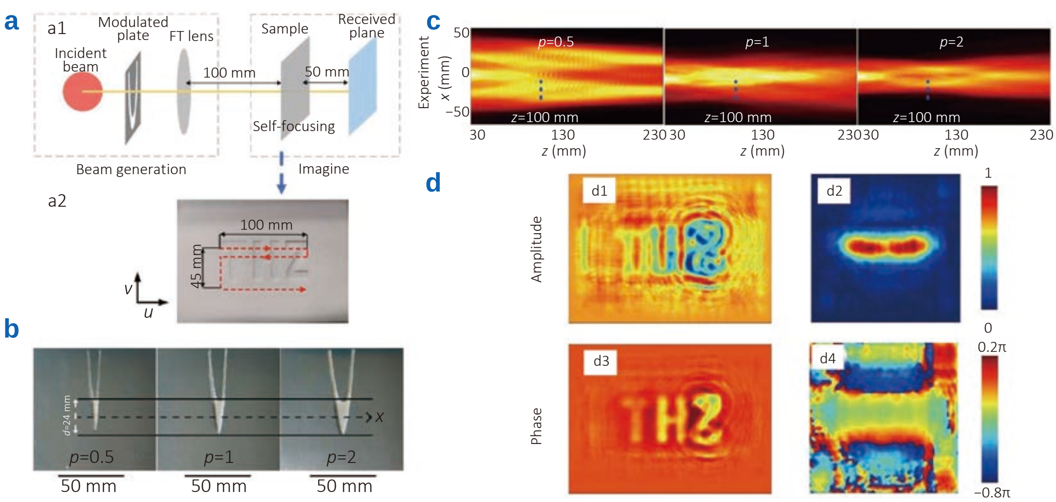

Fig. 12 | Terahertz ptychography using a quasi-pearcey beam as the probe. (a1) Schematic of ptychography of the quasi-Pearcey beam. (a2) The ptychography sample with the illuminating trace. (b) The parabola-slit amplitude modulated plates with different parameters p. (c) Show the x-z cross-sectional intensity distribution of the Pearcy beam under the parameters in (b). (d) Reconstruction (d1, d2) amplitude and (d3, d4) phase of the sample and the probe when p = 0.5 and z = 100 mm. Figure reproduced with permission from ref.[140], under a Creative Commons Attribution License.

2.3.1 Methods for improving quality of reconstruction

The different reconstruction algorithms for THz-CT yield varying results. Using a 110 GHz Gunn diode source, comparisons of filtered back projection (FBP), simultaneous algebraic reconstruction technique (SART), and ordered subset expectation maximization (OSEM) in reconstructing nested objects confirmed terahertz's non-ionizing advantage over X-rays for imaging fragile, unique specimens[29], as shown in Fig. 13(a). Further integrating Gaussian beam properties, when reconstructing polymethacrylimide (PMI) samples with embedded screws (Fig. 13(b)), OSEM coupled with Gaussian beam modeling yielded significantly superior accuracy over alternative algorithms[141].

Combining Gaussian beam modeling with the ordered subsets convex (OSC) algorithm enables reconstruction of plastic spray nozzles[30], as shown in Fig. 13(c). This approach exhibited efficient convergence even under noisy and sparse data conditions. Meanwhile, considering the beam refraction and reflection losses on the sample surface, the improved algebraic reconstruction technique (ART) was employed to reconstruct the complex refractive index distributions based on path-length differences and transmission coefficients—though diffraction effects were not fully addressed[142]. Broadband THz-CT system with single-pixel detection implemented a ray-tracing algorithm integrated with SART to reduce artifacts in cylindrical and cubic samples, despite high computational demands[143]. Wavelet transform-based reconstruction algorithm to image a polystyrene cube embedded with metal screws and hollow plastic tubes, with fewer projections, they enable faster reconstruction without compromising visual quality[144]. Subsequently, tomography of ceramic pots using a low-coherence broadband continuous terahertz source minimized sample-induced interference and enhanced signal intensity[145]. To mitigate reflection and refraction artifacts, samples immersed in refractive-index-matched paraffin oil during terahertz tomographic scans yielded reconstructions clearly revealing interfaces between embedded needles and the paraffin matrix, with detection of internal defects as small as 0.5 mm in diameter[146].

Validation studies confirmed THz-CT's non-destructive testing capabilities through Tikhonov-regularized Landweber iteration reconstructions of 3D-printed structures[34], as shown in Fig. 13(d). Further development incorporated L1-regularized geometric forward modeling, effectively suppressing refractive artifacts to resolve 2–5 mm defects with defined boundaries[147]. Independent research demonstrated broadband THz-CT (230–320 GHz) imaging of irregular polyethylene geometries containing cylindrical defects. The computationally efficient conjugate gradient least squares (CGLS) method with early-stopping procedure enabled high-fidelity reconstructions from limited datasets[148]. Deep learning breakthroughs expanded neural network applications in CT denoising. Beyond traditional methods requiring material priors, a THz-DL-CT framework integrates convolutional neural networks with

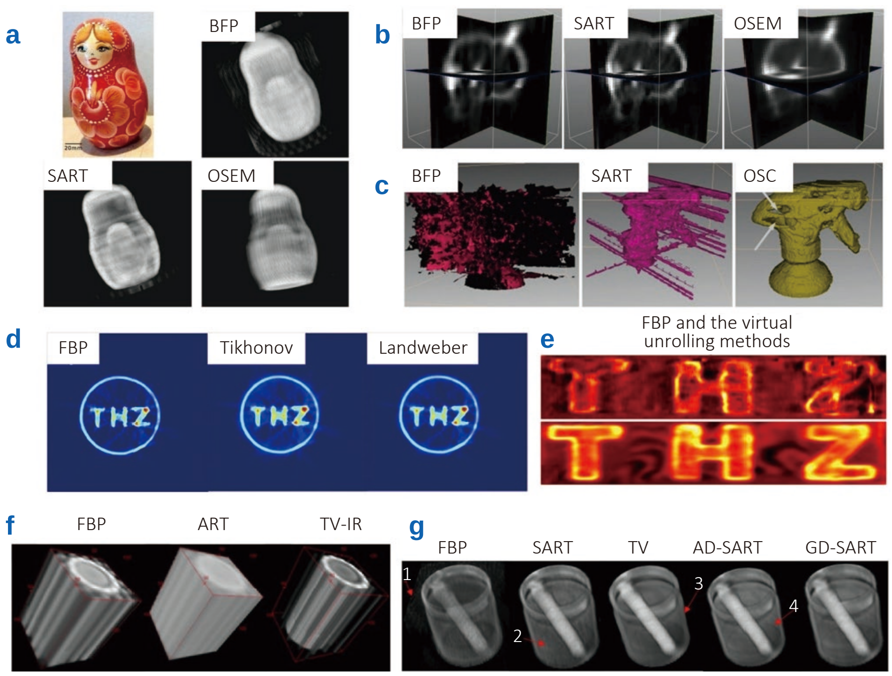

Fig. 13 | Reconstructed results obtained by different THz-CT reconstruction algorithms. (a) Russian nesting dolls. (b) PMI samples with embedded screws. (c) Plastic spray nozzles. (d) 3D-printed letters. (e) Curved canvas. (f) Acrylonitrile butadiene styrene tube. (g) Metal rod packaged with a plastic cup. Figure reproduced with permission from: (a) ref.[29], under a Creative Commons Attribution License; (b) ref.[141], SPIE; (c) ref.[30], (d) ref.[34], (e) ref.[35], under a Creative Commons Attribution License; (f) ref.[33], Optica Publishing Group; (g) ref.[32], Springer Nature.

asynchronous optical sampling THz-TDS. This method extracts material dielectric and geometric-governed time-domain features to resolve structural information. Multi-cycle signal accumulation autonomously encodes object spatiotemporal characteristics, eliminating material priors[149]. Advancements in reconstruction methodologies include virtual unfolding algorithms for imaging curved specimens (Fig. 13(e)), demonstrating applicability in cultural conservation and security screening[35]. Concurrently developed total-variation gradient descent iterations reduced acquisition time while suppressing artifacts[33], as shown in Fig. 13(f). Further innovations implemented dual dictionary-learning for sparse-data reconstruction, preserving local textures and structural details[32], as shown in Fig. 13(g).

Non-diffracting beams, particularly Bessel beams, enhance THz-CT through extended depth of focus. Replacing Gaussian beams with Bessel illumination significantly improves focal depth in continuous-wave systems. Given sparse optical components in this spectral regime, terahertz zero-order Bessel beams primarily employ axicon configurations. Studies demonstrate Teflon axicons (26° base angle) generating beams with 2.6 mm diameter and ~100 mm non-diffracting range, yielding superior reconstruction quality[150]. Alternative implementations include 3D-printed axicons (160° apex-angle, refractive index n=1.655, absorption coefficient α=1.5 cm^{-1}) for metallic object imaging[151], and polyethylene axicons (150° apex-angle) producing 3.7 mm diameter beams with 40.2 mm non-diffracting distance for foreign body detection[152]. Systematic characterization of polytetrafluoroethylene axicons at 2.52 THz via optically pumped lasers[153] further enabled THz-CT implementations achieving 8 mm beam diameter with 45 mm non-diffracting propagation[33]. Figure 14 shows the system diagram.

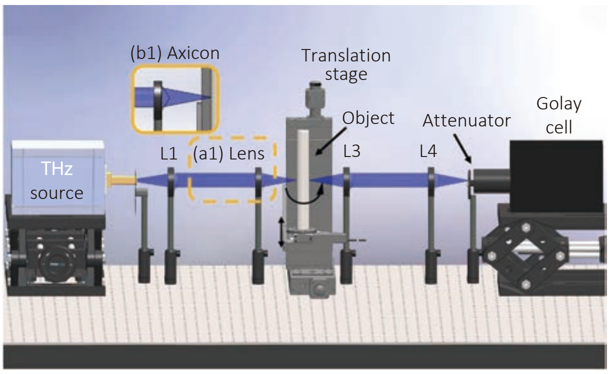

Fig. 14 | Device diagram of the terahertz CT system based on Bezier beams. Figure reproduced with permission from ref.[33], Optica Publishing Group.

2.3.2 Methods for improving imaging resolution

Terahertz computed tomography resolution is governed by transverse spot dimensions and depth of focus (DOF), where full-width-at-half-maximum (FWHM) defines spatial resolution. Terahertz super-oscillatory lenses (TSOLs) enable sub-diffraction transverse focusing with extended DOF. Phase-type TSOLs employing concentric ring arrays achieved 1.212λ transverse spots with 19.7λ DOF through deep reactive ion etching[154]. Subsequent designs combining vectorial angular spectrum theory and swarm optimization reduced transverse spots to 0.67λ while mitigating focus broadening and asymmetry[155]. Binary phase plates integrated with conventional lenses produced 0.8λ focal spots, achieving ~0.85× Rayleigh-limited resolution[156]. Amplitude-type TSOLs fabricated via annular metal slits demonstrated ~0.5λ resolution and 16λ DOF—10.8× greater than traditional lenses[157]. Photosensitive resin-based phase TSOLs attained 0.97λ spots with 25λ DOF and <15% sidelobe ratios[36]. Strategic TSOLs ring-array designs enable versatile light-field manipulation—reducing focal spots, extending axial DOF, and suppressing sidelobes. Representative research fabricated phase-type Fresnel lenses producing dual focal planes (5 mm/10 mm) with 0.55 mm/0.43 mm spots and 2.13 mm/1.55 mm DOF[158]. Subsequent Fibonacci lens implementations achieved focused planes at 6.7 mm/13.4 mm with 0.46 mm/0.55 mm spots, resolving 1.6λ features in point-scan imaging[159]. Advanced multi-step Fresnel zone plates generated 0.43 mm spots with 20 mm non-diffracting propagation, enabling wavelength-resolved 3D imaging via extended-DOF fields[160].

2.3.3 Methods for improving imaging speed

THz-CT data acquisition typically requires time-intensive mechanical translation/rotation. Sparse-angle reconstruction algorithms address this by reducing projection requirements. Research groups combined modified SART with Gaussian filtering and morphological processing, achieving 75% acquisition time reduction[161]. Parallel work employed total variation iterative reconstruction, maintaining image quality while significantly shortening acquisition time[33]. Beam steering via galvanometric and rotating mirrors accelerates terahertz imaging beyond mechanical stage limitations. Early implementations utilized cylindrical-lens THz-TDS systems with 2D line beams, completing 36-angle projections of centimeter-scale samples in 6 min[162]. Parallel developments integrated aspheric f-θ lenses with 2D galvanometric mirrors for continuous-wave scanning, achieving 4 mm spatial resolution over 100 mm fields of view[163]. Subsequent developments using polygon-mirror scanning combined with f-θ optics enabled capturing 250 pixel×180 pixel transmission images at 0.32 f/s (with an 80 mm/s scan speed and 2.83 mm resolution)[164]. Further progress includes high-speed rotating mirrors for 10000 pixel acquisitions within 1 s (imaging pen caps and TPX-particle bags)[165], as well as systems combining large off-axis paraboloids with galvanometers to scan 15 mm×15 mm×34 mm polypropylene pen caps in <15 min[31]. Advancements in imaging systems included replacing single-pixel detectors with pyroelectric arrays to accelerate holographic recording[166], along with developing full-field galvanometer scanning imaging methods. These integrate f-θ lens spot correction and LABVIEW-controlled triangular wave signals for ultra-stable, low-noise illumination, as shown in Fig. 15[167]. Such systems can image metal rods in paper straws, with imaging speed 98% faster than traditional point-scanning systems, and reconstructed results detailed in Fig. 16[37].

In summary, terahertz computed tomography is indispensable for cultural heritage preservation and non-destructive 3D inspection due to its high penetration and non-ionizing nature. State-of-the-art techniques leverage super-oscillatory lenses (0.5λ resolution), Bessel beams for extended depth-of-field (~100 mm), and sparse-angle reconstruction (75% faster acquisition) to enhance quality, resolution, and efficiency, while deep learning and compressed sensing mitigate limited projections. Challenges remain in suppressing refractive artifacts, high-speed scanning of large samples, and quantitative reconstruction of complex internal structures. Future directions will focus on multi-spectral beam shaping via diffractive optics (e.g., multi-step Fresnel zone plates), galvanometer-f-θ systems, and end-to-end neural networks to establish dynamic multi-physics tomography platforms, accelerating clinical pre-imaging and integrated circuit inspection applications.

3 Terahertz focal-plane imaging technology

3.1 Invention of terahertz focal-plane imaging

As an important development branch of terahertz imaging, a terahertz focal-plane imaging technique has been widely concerned and improved since it was proposed. In traditional terahertz imaging, the terahertz beam had to be focused on the surface of a sample. By successively varying the position of the sample, a series of transmitted or reflected terahertz signals were measured to build a terahertz image[1,168], as shown in Fig. 17(a). The drawbacks of the measurement scheme were apparent, including low data acquisition speed and sampling rate. The invention of a

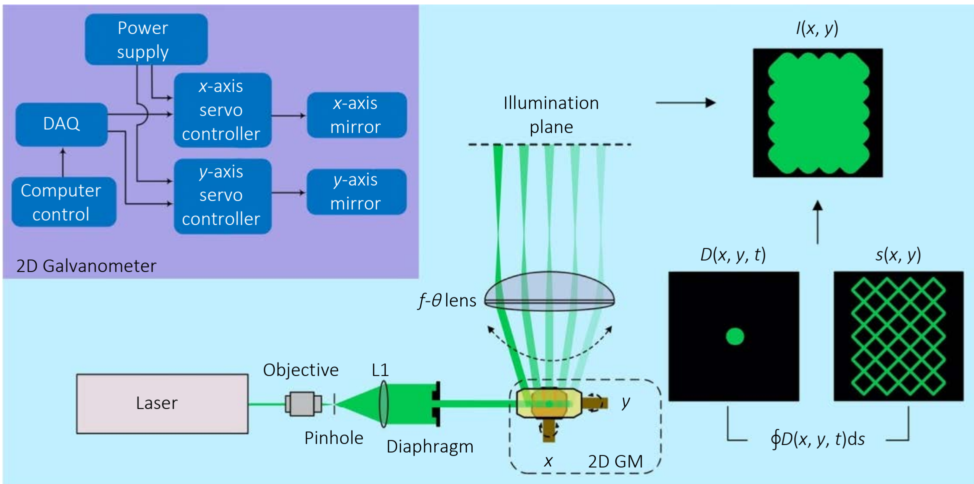

Fig. 15 | Schematic of dual-axis galvanometer scanning illumination setup. 2D GM represents the two-dimensional galvanometer, L1 is a long focal lens. Figure reproduced with permission from ref.[167], Elsevier.

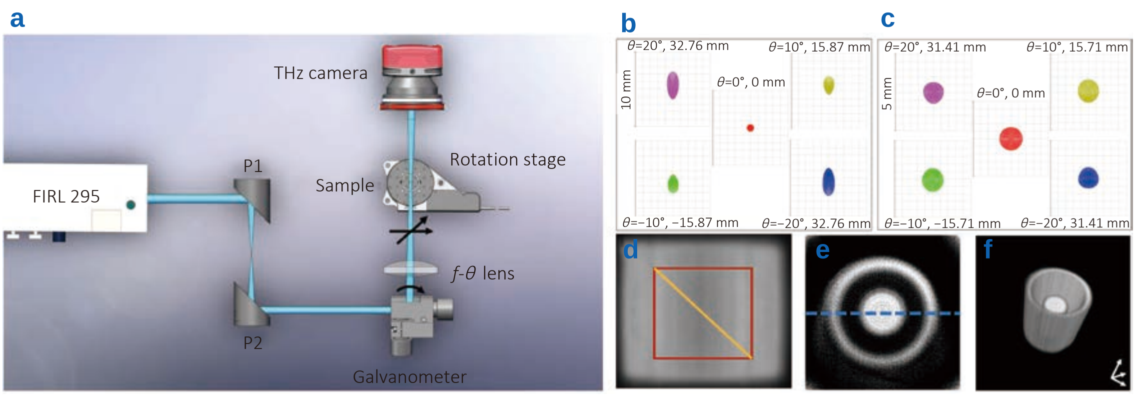

Fig. 16 | Terahertz CT rapid imaging system employing 2D galvanometer mirror and f-ϑ lens with reconstruction results. (a) Device schematic diagram. (b, c) Schematic diagrams of the focused spot shapes before and after optimization of the f-ϑ lens. (d) Scanning light field distribution. (e) 2D cross-section diagram of the paper straw containing a metal rod. (f) 3D reconstruction result. Figure reproduced with permission from ref.[37], Elsevier.

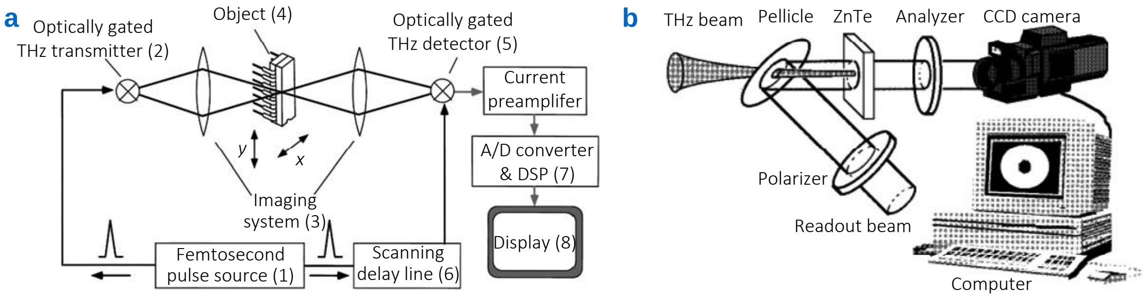

Fig. 17 | Comparison between terahertz raster scan and focal-plane imaging. (a) Traditional terahertz raster scan imaging technique. (b) Terahertz focal-plane imaging technique. Figure reproduced with permission from: (a) ref.[1], Optica Publishing Group; (b) ref.[38], AIP Publishing.

terahertz electro-optic (EO) detection method provided possibility for solving with the problems. In the method, a terahertz field acted as a transient bias to modulate the birefringence of an EO crystal via the Pockels effect[169]. After traveling through the crystal, the polarization of a synchronous probe beam was modulated to carry the terahertz information and a terahertz temporal signal was extracted by analyzing the probe polarization. In 1996, Wu Q et al. demonstrated the high dynamic range of the EO detection method and firstly proposed the concept of terahertz focal-plane imaging[170]. Subsequently, Wu Q et al. achieved terahertz focal-plane imaging on the experiment based on the EO detection method[38], as shown in Fig. 17(b). In the measurement scheme, an unfocused terahertz beam co-propagated with a collimated probe beam to illuminate a large-scale EO crystal. In the crystal, the two-dimensional (2D) terahertz spatial information was loaded on the wave front of the probe beam. Before and after the EO crystal, a pair of cross-polarizers were utilized to remove the background intensity of the probe beam. Then, a high-performance CCD camera was used to capture the probe beam and extract a terahertz image. In the technique, terahertz signals on all pixels were parallel measured, so the data acquisition speed was greatly enhanced. When an object was inserted into the path of the terahertz beam, its transmission terahertz image could be obtained without raster scanning. In addition, the sampling rate was also significantly increased based on the detection array of the CCD. Undoubtedly, the invention of the technique remarkably upgraded the practicability of terahertz imaging. Therefore, the technique rapidly became a research hot spot in terahertz imaging.

3.2 Performance enhancement of terahertz focal-plane imaging

Although superiorities of terahertz focal-plane imaging were significant, an intrinsic problem of the technique had to be confronted. Unlike traditional terahertz imaging, a lock-in amplifier could not be used to extract a terahertz signal in the technique so that the signal-to-noise (SNR) of a terahertz image is lower. To solve with the problem, Jiang ZP et al. proposed a dynamic subtraction method in 2000[39]. In the method, the output of a terahertz beam and the exposure of a CCD were synchronously controlled, as shown in Fig. 18(a). The images of the probe beam with and without the terahertz modulation were successively captured and their subtraction operation was implemented to remove the long-term drift of the background intensity. Utilizing the method, an improvement of SNR by approximately 2 orders and a frame rate of 69 FPS were achieved. Since then, researchers tried various methods to improve the performances of the imaging technique and explored its applications in different fields.

In 2009, Wang XK et al. comprehensively analyzed the spatial resolution of a terahertz focal-plane imaging system with a quasi-near-field detection scheme[42], as shown in A region of Fig. 18(b). In the scheme, the terahertz and probe beams irradiated a ZnTe sensor crystal from both sides by using a non-polarizing beam splitter (BS). An anti-reflection coating was fabricated on the right surface of the crystal so that the probe beam could enter the crystal with a high transmittance. Then, the probe beam was reflected by the left surface of the crystal and was collinear with the terahertz beam in the crystal to carry the terahertz information via the EO detection. In this way, a sample could be mounted close to the crystal and the terahertz beam transmitted from the sample was directly measured. In the measurement mode, the sub-wavelength probing capability of the imaging system was fulfilled because the diffraction of the terahertz beam was weakened as far as possible. To further upgrade the SNR of the imaging technique, Wang XK et al. introduced a differential detection technique in 2010[43], as shown in B region of Fig. 18(b). In this work, two cross-polarizers were replaced by a quarter wave plate (QWP) and a Wollaston prism (WP) for extracting a terahertz signal from the probe beam. The method was very similar to a detection technique which was widely applied in terahertz time domain spectroscopy (THz-TDS)[171,172]. The QWP was used to impart a π/2 optical bias on the probe beam and the WP was used to split the probe beam into two mutually orthogonal linearly polarized beams. The two spots were projected onto a CCD by a lens combination consisted of L2 and L3. The terahertz modulations on the two spots

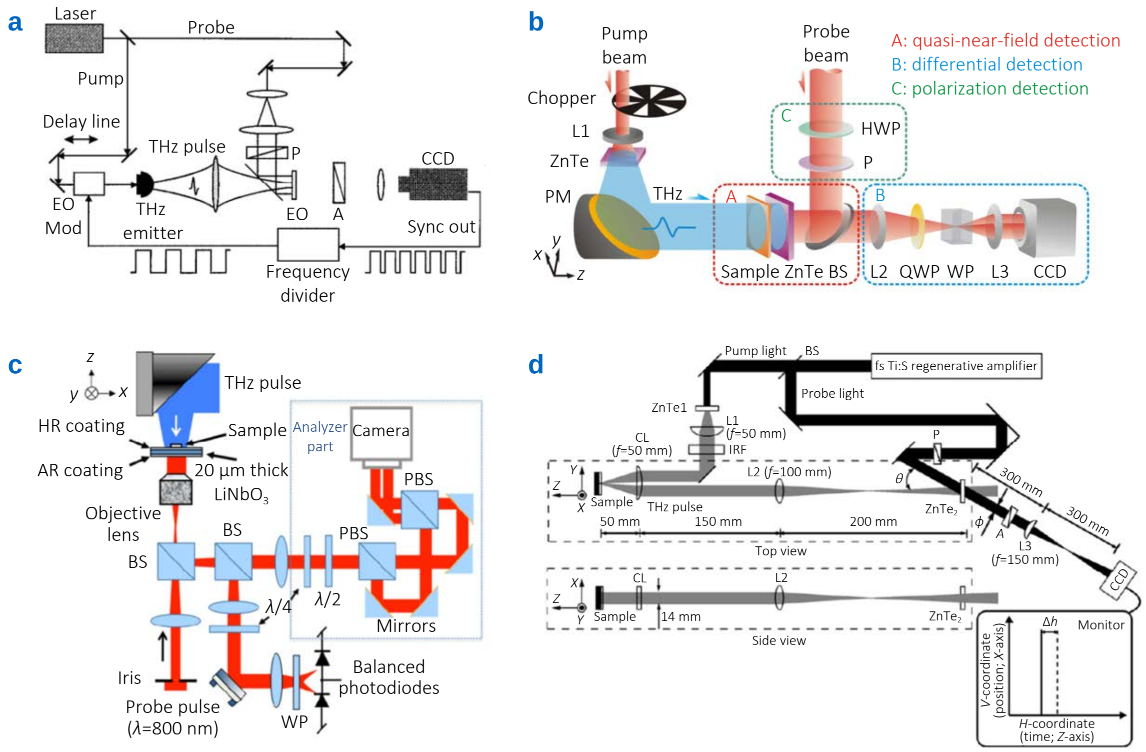

Fig. 18 | Improvements of terahertz focal-plane imaging. (a) A dynamic subtraction method was introduced to remove the long-term drift of the background probe intensity. (b) Quasi-near-field, differential, and polarization detection techniques were introduced to improve the spatial resolution and signal-to-noise (SNR) as well as add a polarization measurement function for the imaging system. (c) A very thin sensor crystal was utilized for approaching the resolution limitation of the imaging system. (d) Terahertz line scan imaging based on a spatio-temporal EO detection method. Figure reproduced with permission from: (a) ref.[39], Optica Publishing Group; (b) ref.[42–44], Optica Publishing Group; (c) ref.[45], under a Creative Commons Attribution License; (d) ref.[40], Elsevier.

were opposite, so a terahertz signal was extracted and amplified by 2 times by subtracting the two spots. By combining the differential detection and dynamic subtraction methods, the background intensity of the probe beam was more effectively removed and the SNR of the imaging system was further enhanced by approximately 4 times. In 2010, Wang XK et al. also introduced a polarization detection function into the imaging system[44], as shown in C region of Fig. 18(b). According to ref.[171], a ZnTe crystal with a <110> orientation could respond different terahertz polarization components by adjusting the angle between its crystalline axis and the probe polarization. Therefore, a half wave plate (HWP) and a polarizer (P) were inserted into the path of the probe beam to vary the probe polarization. When the probe polarization was parallel or perpendicular to the <001> axis of the crystal, a terahertz horizontal component (E_x) was measured. When the angle between the probe polarization and the <001> axis of the crystal was 45°, a terahertz vertical component (E_y) was measured. Using the method, different terahertz polarization images could be separately obtained without varying the azimuth angle of the ZnTe crystal[173] and the measurement accuracy of the imaging system was not influenced. By measuring properties of a common glass, a fused quartz, and a monocrystalline quartz, the polarization detection function of the system was demonstrated.

To further approach the resolution limitation of the imaging technique, Blanchard F et al. utilized a 20 μm thick $LiNbO_3$ as the sensor crystal to achieve a 14 μm resolution for a center frequency at 0.7 THz (corresponding to $\lambda/30$)[45], as shown in Fig. 18(c). In this way, the diffraction of a terahertz wave could be substantially avoided in the crystal. Of course, the method caused a small EO response due to the very thin EO crystal. To ensure enough SNR, the terahertz radiation was generated by the optical rectification in a $LiNbO_3$ prism with titled-pulse-front excitation[174]. Utilizing the system, an electric field enhancement effect of a metallic dipole antenna was clearly characterized after the excitation of an intense terahertz pulse. In 2016, Blanchard F et al. improved the performances of the system to a greater extent[175]. They utilized a 1 μm thick $LiNbO_3$ as the sensor crystal to more effectively acquire the terahertz near-field information. In addition, 842 nm and 776 nm shortpass filters were placed before and after the sensor crystal on the path of the probe beam. In this way, they selected probe photons that contributed to a terahertz signal and suppressed the noise. By using the method, a 5 μm resolution was achieved and the effective frequency range could reach from 100 GHz to 4 THz. By characterizing the morphology of a gold Sierpinski fractal antenna, the probing capability of the system was fully demonstrated.

In general terahertz systems, a ZnTe or GaP crystal with a <110> orientation was commonly used in terahertz generation and detection. With the maturation of the EO detection technique, researchers realized that the EO crystal with a <100> orientation could respond a longitudinal component (E_z) of a terahertz field. Utilizing the property, a <100> ZnTe or GaP crystal could be used to coherently measure E_z for a terahertz converging field in free-space[176] or a terahertz surface plasmon wave on a metallic sub-wavelength structure[177]. In 2014, Wang XK et al. introduced a <100> ZnTe crystal into a terahertz focal-plane imaging system to measure E_z components of terahertz converging fields with different polarizations[178]. E_z with a linear polarization (LP) presented a dipole-like distribution, while E_z with circular and cylindrical vortex polarizations showed annular amplitude and vortex phase patterns. This work further strengthened the acquisition ability of the imaging system for the terahertz polarization information and provided more application possibilities for the technique. So far, the terahertz focal-plane imaging technique possessed powerful probing capabilities, which ensured sufficient SNR and resolution as well as enabled the acquisition of different polarization information.

Notably, Yasuda T et al. proposed a novel terahertz line scan imaging system based on a spatio-temporal EO detection method in 2006[40], which was similar to terahertz focal-plane imaging. As shown in Fig. 18(d), a terahertz beam was first line focused on a sample surface in the system. The terahertz focal line reflected by the sample was imaged by a biconvex terahertz lens onto a <110> $ZnTe_2$ crystal. Then, a probe beam was incident on the crystal at a crossed angle θ. The non-collinear overlapping of the terahertz and probe beams enabled that the terahertz fields at different time delays were translated into different spatial positions across the transverse profile of the probe beam. It meant that a 2D spatio-temporal terahertz image was loaded on the probe wave front, in which the terahertz temporal signal and the terahertz one-dimensional (1D) transverse distribution could be separately extracted from the horizontal and vertical profiles of the probe beam. Finally, a CCD was used to capture the probe beam and two cross-polarizers was used to extract the terahertz information. In the scheme, the high-speed single-shot measurement of a terahertz temporal signal was fulfilled so that the technique could be readily applied to fast scan a moving object. Using the technique, the research group achieved diagnosing of crystallinity for a human dental tissue[179] and a fast three-dimensional (3D) computed tomography for a gelatin soluble capsule[162]. It could be said that the technique provided a new insight for the development of terahertz focal-plane imaging.

3.3 Applications of terahertz focal-plane imaging technology

3.3.1 Characterization of terahertz wave fronts

By virtue of the advantages of terahertz focal-plane imaging, many applications have been explored in various fields. An immediate application was to observe the wave front distribution of a terahertz diffraction field in free-space. In 1999, Jiang ZP et al. firstly used the imaging technique to characterize the spatio-temporal distribution of a focusing terahertz beam[180]. The terahertz main spot with the time delay of t=0 presented a Gaussian-like pattern on the focal-plane, as shown in Fig. 19(a1). Simultaneously, the terahertz spot showed varying ring structures with increasing the time delay. A spatio-temporal pattern of a terahertz field was extracted on the x-t plane, which exhibited a typical X-shape, as shown in Fig. 19(a2). The spatio-temporal property of the terahertz field was also exactly simulated by using a propagation equation. This work gave a direct observation of a terahertz wave front so that researchers could more intuitively analyze propagation features of a terahertz wave.

From 2016 to 2018, the diffraction processes of various terahertz special beams were comprehensively measured and analyzed by using the imaging technique, such as terahertz vortex, Bessel, and bottle beams[46–48]. In 2016, Wang XK et al. generated a converging terahertz vortex beam with a circular polarization by using a terahertz spiral phase plate and a terahertz QWP as well as characterized its vectorial field distributions[46]. Figure 19(b) shows E_x and E_z at 0.62 THz for a right-hand circularly polarized terahertz vortex beam with the topological charge of l=1 on the focal-plane. The E_x amplitude exhibited a typical doughnut shape due to the central phase singularity, as shown in Fig. 19(b1). The E_x phase presented an expected spiral pattern which monotonically increased along the azimuthal direction, as shown in Fig. 19(b3). Interestingly, the E_z amplitude exhibited a main focal spot and weak annular side-lobes; the E_z phase contained several concentric annular patterns, as shown in Fig. 19(b2) and 19(b4). The phenomena were very similar to those of a radially polarized beam, which was formed through the interference between orbital angular momentum (OAM) and spin angular momentum (SAM) of a terahertz photon[181]. Using a modified Richards-Wolf vector integration algorithm, the propagation features of E_z was accurately simulated. In 2017, Wu Z et al. used a Teflon axicon to generate a linearly polarized terahertz Bessel beam and measured its non-diffractive feature by applying the imaging technique[47]. Figure 19(c1) and 19(c2) give the amplitude distributions of E_x at 0.6 THz on the x-y and y-z planes. The terahertz field presented a central main peak and concentric ring side-lobes. Notably, the terahertz field showed a propagation invariance in the range of 24 mm. The size of the main peak was almost fixed in the diffraction-free region. The corresponding phase patterns of E_x were also acquired on the transverse and longitudinal cross-sections, as shown in Fig. 19(c3) and 19(c4). The phase was composed of several concentric circles and a phase jump of π occurred on the interface between adjacent circles. In the diffraction-free region, the phase always kept a flan plane around the optical axis, which ensured that the terahertz field consistently maintained the constructive interference

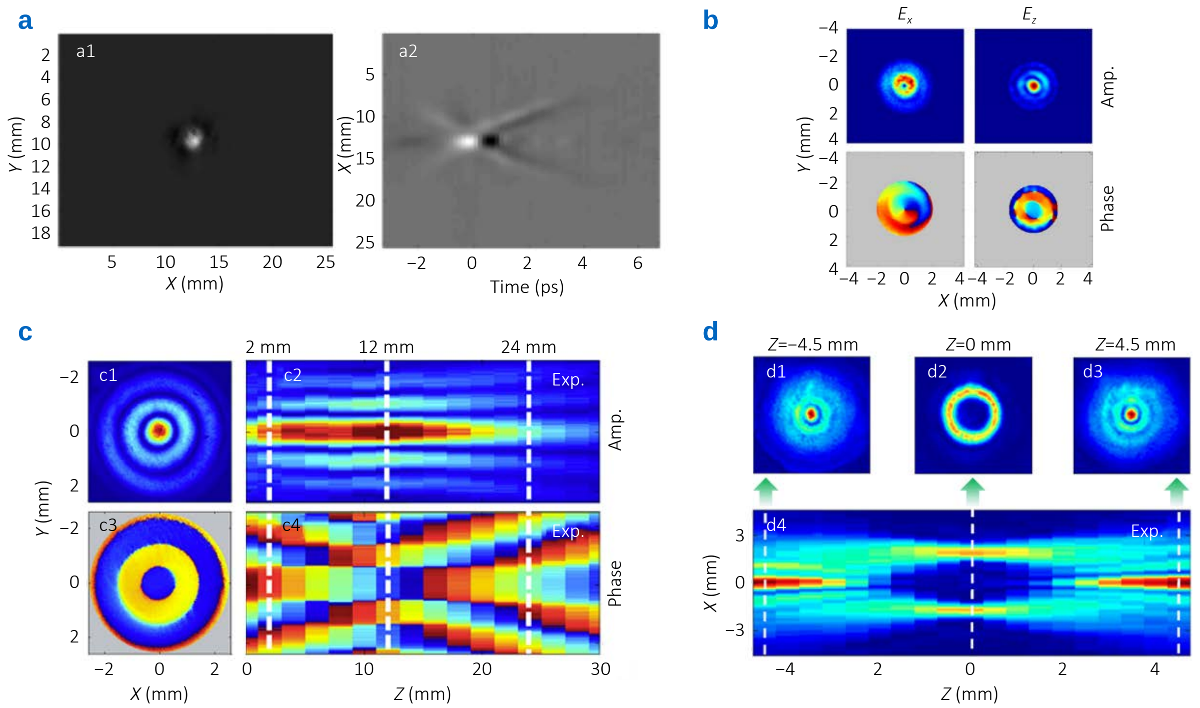

Fig. 19 | Characterization of terahertz wave fronts. (a) A focusing terahertz Gaussian beam. (a1) Tearahertz spot on the focal plane. (a2) Terahertz spatio-temporal distribution on the *x*-*t* plane. (b) A circularly polarized terahertz vortex beam. (b1, b2) The amplitude distributions of E_x and E_z. (b3, b4) The corresponding phase patterns. (c) A terahertz Bessel beam. (c1, c2) The amplitude distributions of E_x on the *x*-*y* and *y*-*z* planes. (c3, c4) The corresponding phase patterns. (d) A terahertz bottle beam. (d1–d3) The amplitude distributions of E_x on the *x*-*y* plane at *z*=−4.5 mm, 0 mm, 4.5 mm. (d4) The longitudinal amplitude cross-section of E_x on the *x*-*z* plane. Figure reproduced with permission from: (a) ref.[180], (b) ref.[46], (c) ref.[47], (d) ref.[48], under a Creative Commons Attribution License.

during propagation. The special phase distribution caused the non-diffractive feature of the terahertz Bessel beam. In 2018, Li HT et al. employed a combination of a Teflon axicon and a silicon lens to generate a terahertz bottle beam with a *x*-LP and observed its evolution by using the imaging technique[48]. Figure 19(d4) exhibits the longitudinal amplitude cross-section of E_x at 0.75 THz on the *x*-*z* plane. Obviously, both front and back parts of the terahertz bottle beam presented a main focal spot. However, a dark focus was formed at the central part of the terahertz bottle beam at *z*=0 mm. The 2D amplitude transverse distributions of E_x were extracted at *z*=−4.5 mm, 0 mm, and 4.5 mm, as shown in Fig. 19(d1–d3). Both amplitude images at *z*=−4.5 mm and 4.5 mm presented a circular central main spot and annular side-lobes, which was analogous to a Bessel-like beam. The amplitude image at *z*=0 mm exhibited a central dark focus surrounded by a uniform optical barrier. Overall, the terahertz bottle beam formed a 3D optical potential well. The diffraction features of these terahertz special beams were very valuable for particle acceleration[182], terahertz communications[183], terahertz imaging[28], and so on. The imaging technique provided a powerful platform for characterizing terahertz special beams. Besides, the wave front measurement function of the imaging technique could be also applied in other fields. For instance, a Gouy phase shift of a converging terahertz beam could be measured and analyzed[184]; distinctive patterns of E_z components could be coherently measured for terahertz fields with different polarizations, which were used to extract the corresponding terahertz polarization states[185]; an adaptive correction of geometrical aberrations on a terahertz beam could be fulfilled by combining the imaging technique and a deformable mirror[186].

3.3.2 Function verification of terahertz metasurfaces

As one of mainstream development directions for advanced optics, a metasurface device has attracted tremendous attentions since it was firstly proposed[187]. By properly designing and arranging sub-wavelength unit cells, metasurfaces could be used to arbitrarily control all features of a light wave. This kind of devices could possess multi-functions and only had light weight so that the miniaturization and integration of an optical system become possibility. In 2013, Hu D et al. firstly introduced metasurfaces into the terahertz field and achieved terahertz imaging and holography by using metasurfaces with a 100 nm thickness (1/4000th of the wavelength of the illuminating light)[188]. Since then, a large number of terahertz metasurfaces has been developed and the terahertz focal-plane imaging supplied an important means for function verification of these devices. For instance, Wang B et al. adopted a simulated annealing algorithm to design a dual-color terahertz metasurface hologram in 2016[189], as shown in Fig. 20(a). Hologram patterns of two letters "C" and "N" were separately loaded on terahertz wave fronts at 0.5 THz and 0.63 THz based on the device and its wavelength de-multiplexing function was characterized by the imaging technique. In 2018, Zhao H et al. developed an OAM multiplexing and de-multiplexing terahertz metasurface[190]. Utilizing the device, four focused phase vortex beams with different topological charges and propagation directions were generated under an incident terahertz Gaussian beam, as shown in Fig. 20(b). In addition, only one corresponding channel was recognized on the focal-plane when each of the individual vortex beams was incident on the device. The OAM multiplexing and de-multiplexing functions of the device was clearly demonstrated by the imaging technique. It was possible that the information transmission capability of terahertz communications was enhanced based on the device. In 2018, Guo JY et al. designed a terahertz meta-surface composed of cross-antennas to simultaneously modulate the amplitude, phase, and polarization of a terahertz field[191]. Based on the device, a terahertz Lorentz beam with a radial or angular polarization was formed with a right- or left-hand circularly polarized terahertz incident beam, as shown in Fig. 20(c). Using the imaging technique, different polarization components of terahertz Lorentz beams were accurately measured and distinctive responses of the device to different polarized incident lights were validated. In 2022, Li JT et al. developed a silicon-based terahertz meta-lens using dynamic phase to realize single-hand circular polarization conversion[49]. After passing through the device, a linearly polarized terahertz wave could be completely converted into a single-hand circular polarization. Furthermore, switching among LP, left-hand, and right-hand circular polarizations (LCP and RCP) could be readily manipulated by rotating the device with ±45° and ±90°, as shown in Fig. 20(d). Besides, a reversible polarization conversion was also achieved by the same device. When a terahertz wave with a single-hand circular polarization passed through the device, it could be completely converted into LP. It was possible that the metalens was used in advanced terahertz camera for polarization imaging. In 2023, Zhao H et al. designed a tri-layer terahertz meta-surface for multi-channel polarization generation and phase modulation[50]. Utilizing the modulation function of the device, a vectorial hologram with eight channels

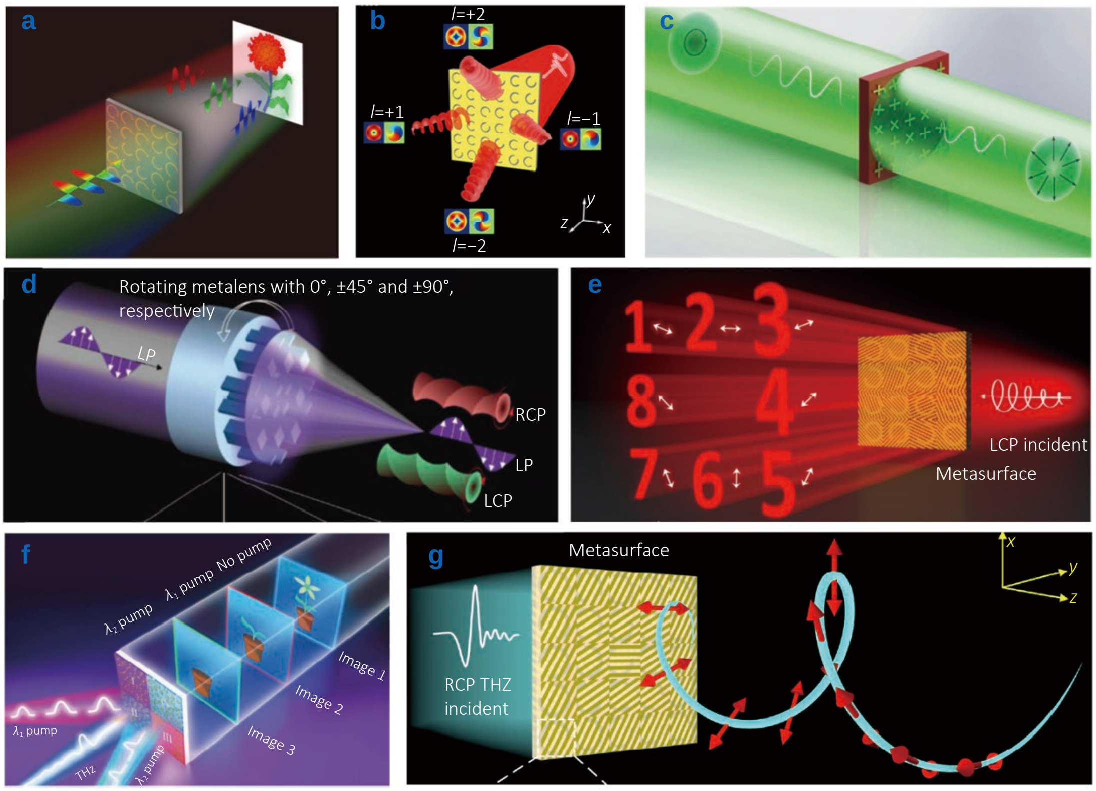

Fig. 20 | Function verification of terahertz meta-surfaces. (a) Multi-color metasurface hologram. (b) OAM multiplexing and de-multiplexing terahertz meta-surface. (c) Metasurface for generating a terahertz Lorentz beam with a radial or angular polarization. (d) Silicon-based terahertz metalens for single-hand circular polarization conversion. (e) Tri-layer terahertz metasurface for multi-channel polarization generation and phase modulation. (f) Pump-wavelength sensitive spatiotemporally tailored terahertz metadevice. (g) Meta-surface for generating a spatially structured light beam with continually changing polarization along an arbitrary transmission trajectory. Figure reproduced with permission from: (a) ref.[189], under a Creative Commons Attribution License; (b) ref.[190], American Chemical Society; (c) ref.[191], John Wiley and Sons; (d) ref.[49], (e) ref.[50], under a Creative Commons Attribution License; (f) ref.[51], John Wiley and Sons; (g) ref.[52], under a Creative Commons Attribution License.

(digits "1"–"8") for different LP states was realized, as shown in Fig. 20(e). The information in a specific channel could be hid via the selection of the polarization state to be detected. Moreover, the working efficiency of the device approximately approached 80%. The device opened up a new way for terahertz communications and information security. In 2024, Wang GC et al. proposed a pump-wavelength sensitive spatiotemporally tailored terahertz meta-device by integrating a meta-surface and 2D perovskites films with different bandgaps[51]. The wave front of the incident terahertz field could be spatially modulated by the metasurface and the transmission of the terahertz beam could be temporally controlled by optical excited 2D perovskites films. In this scheme, dynamic switching of a terahertz multi-focal lens and a dynamic display of holographic characters were experimentally realized by properly selecting a pumping wavelength, as shown in Fig. 20(f). This work provided a new pathway for designing more complex dynamic metadevices. In 2024, Nan T et al. developed a tri-layer metallic metasurface to generate a spatially structured terahertz beam with continually varying polarization along an arbitrary propagation trajectory[52]. With the metasurface, the phase and polarization of an incident terahertz field were properly modulated by ingeniously arranging the geometric characteristics of each layer structure. In this way, two terahertz structured beams with varying polarization states along a spatial helical transmission trajectory were formed, as shown in Fig. 20(g). A terahertz beam showed continuous variation from 15° LP to 75° LP, while other beam underwent transitions from 15° LP to RCP and then back to 75° LP. This work opened up new possibilities for creating customized spatial structured beams. Overall, marvelous functions of these meta-surfaces could be accurately and comprehensively characterized by the imaging technique. Besides, terahertz surface waves (TSWs) excited on sub-wavelength surface plasmonic devices (SPDs) could be also measured by the imaging technique. In 2016, Wang XK et al. generated TSWs by using rectangular and semi-circular slits and observed their temporal variations by using the imaging technique[86]. In 2019, Li HT et al. combined a Bessel-like terahertz beam and a metallic semi-circular slit to realize a terahertz surface plasmon light capsule. Utilizing the imaging technique, the spatial distribution and potential applications of the TSW was measured and analyzed[192]. The imaging technique supplied an effective characterization platform for developing integrated terahertz photonic circuits.

3.3.3 Spectral imaging of chemical substances and biological tissues

In terahertz focal-plane imaging, a terahertz signal could be extracted on each pixel and terahertz spectral images at different frequencies could be readily obtained by operating the Fourier transformation. It meant that the imaging technique possessed a spectral measurement function which was almost the same as that of THz-TDS. Taking advantage of the function, spatial patterns of chemical substances with different absorption features could be accurately identified. In 2005, Usami M et al. used a transmission-type terahertz focal-plane imaging system to measure three pellets made from polyethylene powder with salicylic acid (concentration of 70%), biotin (40%), and glucose (30%)[193]. Figure 21(a1) gives the schematic diagram of these pellets. Absorption images of the samples at 1.11 THz, 1.29 THz, and 1.44 THz were acquired, as shown in Figs. 21(a2–a4). It could be seen that the spatial patterns of three chemicals were clearly separated based on their characteristic absorptions. In 2006, Zhong H et al. applied a reflective terahertz focal imaging system to measure five chemicals, including 2,4-DNT, Theophylline, RDX, Glutamic Acid, and glass[194]. Figure 21(b1) and 21(b2) give the optical configuration of the imaging system and the pictures of five samples, respectively. Using the system, reflective spectroscopic imaging of five samples were fulfilled at a standoff measurement distance of 0.4 m. Figure 21(b3) exhibits the absorption images of the samples at 0.82 THz, 0.96 THz, 1.08 THz, and 1.21 THz. Based on their absorption discrepancies, the classification of the samples was achieved with an accuracy rate above 80% by using minimum distance classifier and neural network methods. In 2011, Yasuda T et al. proposed a fast frequency-resolved terahertz focal-plane imaging technique to reduce the time consumption to a certain degree[195]. Using the technique, two spectral images of a target at different frequencies were rapidly obtained in 1 min and three kinds of drugs (L-histidine, CBZ3, and maltose) were successfully distinguished. In 2024, Li C et al. developed an imaging-based pixelated meta-material sensor to achieve the detection of terahertz molecular fingerprint spectra of analytes by combining with a terahertz focal-plane imaging system[53], as shown in Fig. 21(c1). The sensor contained 4 × 4 pixelated array filters with transmission resonances tuned to discrete frequencies. Figure 21(c2) shows the transmission spectra of the meta-pixels without an analyte. The insets presented the transmission images of the device at four specific frequencies. A high transmission intensity marked the excitation of a corresponding meta-pixel in a specific spatial location. In this way, the interaction between an analyte and a localized terahertz field on the device was effectively strengthened. The absorption spectrum of a L-tyrosine sample was measured by using the technique, as shown in Fig. 21(c3). This work was beneficial to terahertz trace detection. In general, the spectral measurement function of the imaging technique was very valuable for security inspection, food and pharmaceutical quality controlling.

The spectral measurement function of terahertz focal-plane imaging could be also applied in biological sensing due to sensitive responses of the terahertz radiation to water content and different tissue structures. In 2017, Guo LH et al. measured natural dehydration processes of three types of animal tissues by adopting the imaging technique[196]. The left part of Fig. 22(a) shows the photos of the samples, including cattle, mutton, and pork. The right part of Fig. 22(a) presents the absorption images of the samples at 0.56 THz with dehydration time of 0 min, 40 min, 80 min, 120 min, 160 min, and 1 day. From experimental results, it could be

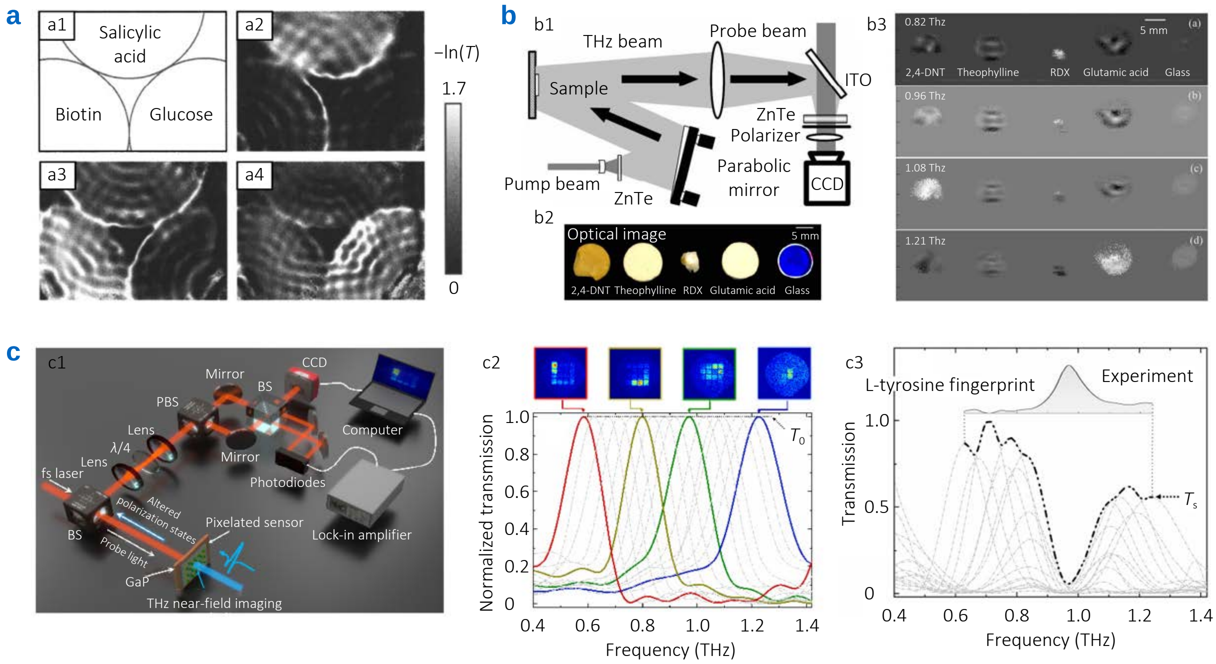

Fig. 21 | Identification of chemical substances. (a) Measurement of three pellets made from polyethylene powder with salicylic acid, biotin, and glucose. (a1) Schematic diagram of three samples. (a2–a4) Absorption images of the samples at 1.11 THz, 1.29 THz, and 1.44 THz. (b) Identification of 2,4-DNT, Theophylline, RDX, glutamic acid, and glass. (b1) Terahertz focal-plane imaging system in reflection geometry. (b2) Optical pictures of five samples. (b3) Absorption images of five samples at 0.82 THz, 0.96 THz, 1.08 THz, and 1.21 THz. (c) Imaging-based pixelated terahertz metamaterial sensor. (c1) Terahertz focal-plane imaging system combining with the sensor. (c2) Transmission spectra of the meta-pixels without an analyte, the insets showed the transmission images of the device at four specific frequencies. (c3) Absorption spectrum of a L-tyrosine sample measured by the technique. Figure reproduced with permission from: (a) ref.[193], AIP Publishing; (b) ref.[194], (c) ref.[53], under a Creative Commons Attribution License.

seen that all of adipose tissues showed weaker absorption to the terahertz radiation than muscle tissues. During dehydration, adipose tissues presented the remarkable loss of water content on a large area. Simultaneously, the cattle and mutton muscle tissues exhibited an overall dehydration phenomenon after 160 min; the porcine tissues showed a significant decline of terahertz absorption after 1 day. This work successfully characterized different water-holding capacities of adipose and muscle tissues in various animal bodies. In 2023, Yang SX et al. used a terahertz focal-plane near-field imaging technique to fulfill the measurement of oral tissues with a resolution of $\lambda/10$ at 1 THz[54]. The left column of Fig. 22(b) shows the histopathological images of test tissues, including ① normal epithelial tissue, ② connective tissue, ③ muscle fiber, ④ tongue squamous cell carcinomas, and ⑤ tongue muscle tissue. The middle and right columns of Fig. 22(b) exhibit the refractive-index and absorption-coefficient images of the samples at 1 THz. According to imaging results, the refractive index of loose connective tissue was lower than that of epithelial tissue and muscle fiber; the absorption coefficient of cancerous epithelial tissue was higher than that of normal epithelial tissue due to different water content; the muscle tissues sliced transversely and longitudinally showed different refractive indexes. This work demonstrated that the imaging technique could identify not only biological tissues with different components, but also normal and cancerous tissues as well as similar tissues with different slice directions. Based on these reports, it could be expected that the imaging technique was applied in the field of biomedicine, especially tumor diagnosis and surgery.

3.4 Other related technologies

Along with the development of terahertz focal-plane imaging, other similar imaging techniques were also proposed and applied in different fields. In 2003, Feurer T et al. adopted a pump-probe imaging technique to generate terahertz-frequency lattice vibrational waves in a 2 mm thick $LiTaO_3$ crystal and observe the spatial-temporal evolution of the terahertz phonon-polariton waves[197], as shown in Fig. 23(a). In this work, the $LiTaO_3$ crystal was excited by a shaped femto-second laser with an 800 nm wavelength and a series of terahertz phonon-polariton wavelets were generated with different spatial locations and time delays in the crystal. Constructive and destructive interferences between the terahertz wavelets were clearly recorded by using a synchronous probe laser with a 400 nm wavelength and a high-performance CCD. This work pointed toward a potential application for programmable controlling of phonon-polaritons into integrated terahertz waveguides. Following that, Wu Q and Werley CA et al. separately attempted different imaging methods to enhance the measurement sensitivity, including Talbot imaging, phase contrast imaging, Sagnac imaging,

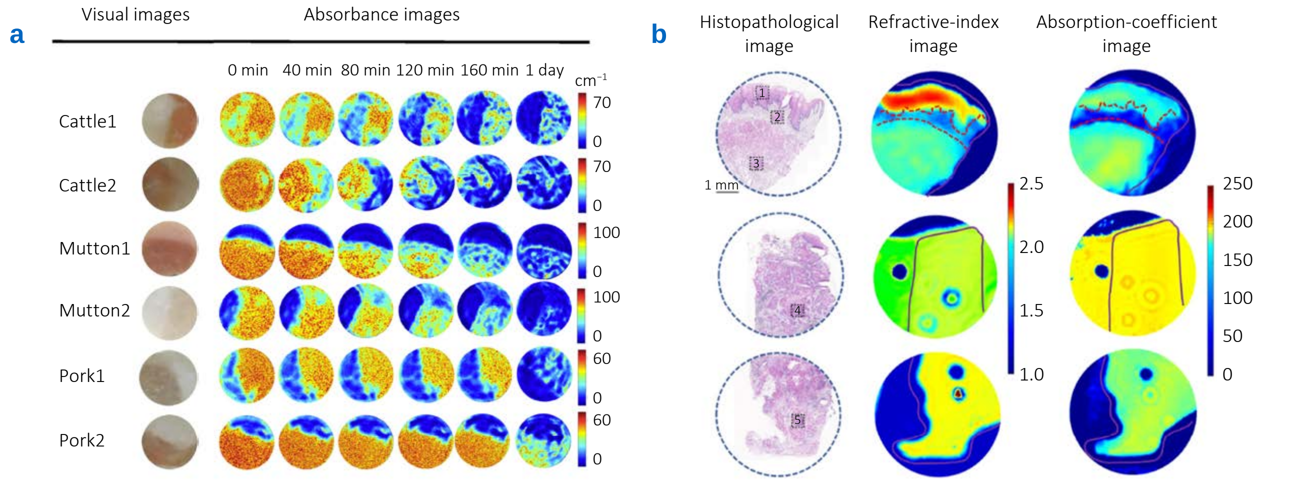

Fig. 22 | Measurement of biological tissues. (a) Measurement of natural dehydration processes for different animal tissues, including cattle, mutton, and pork. The left part were the photos of samples; the right parts showed the absorption images at 0.56 THz with dehydration time of 0 min, 40 min, 80 min, 120 min, 160 min, and 1 day. (b) Imaging of oral tissues. The left column were histopathological images; the middle and right columns were the refractive-index and absorption-coefficient images at 1 THz. Test tissues contained: ① normal epithelial tissue, ② connective tissue, ③ muscle fiber, ④ tongue squamous cell carcinomas, and ⑤ tongue muscle tissue. Figure reproduced with permission from: (a) ref.[196], Optica Publishing Group; (b) ref.[54], American Physical Society.

and polarization gating[198–199].

A photo-conductive antenna was a traditional device for terahertz detection, which has been widely applied in commercial terahertz systems. In 2008, Pradarutti B et al. fabricated a terahertz photo-conductive antenna array with 16-channels and fulfill the terahertz detection by combining with a micro-lens array[41]. Figure 23(b) gives the optical configuration of the terahertz system and the inset shows the photo of the antenna array. In this way, a terahertz focal line was measured and 16 THz temporal signals on the focal line were simultaneously extracted by a multi-channel Lock-in amplifier. This work opened up a new path for fast terahertz imaging. In 2024, Li XR et al. developed a 2D array detector consisted of 0.3 million plasmonic photo-conductive nano-antennas to realize a 1000-fold increase in terahertz imaging speed[200]. Utilizing the device, terahertz imaging with pixel super-resolution was fulfilled by combining with a convolutional neural network algorithm. Taking advantage of the technique, etched patterns in a silicon substrate and defects in battery electrodes were exactly measured and reconstructed. This technique provided possibility for the realization of terahertz imaging with a large number of pixels, large field of view, high SNR, high bandwidth, and fast data acquisition.

In 2022, Tamaki R et al. introduced an echelon mirror into a focal-plane imaging system to fulfill single-shot THz-TDS and measured the dynamics of electrons and ions emitted from a target material during laser ablation[201]. Figure 23(c) gives the schematic diagram of the system. In the path of the pump beam, electrons were emitted from the sample surface under the photoexcitation with an ultrashort laser so that the transient dipole moment was formed and the resultant macroscopic polarization radiated a terahertz wave, as shown in the inset of Fig. 23(c). Then, an echelon mirror was used to introduce a staircase-shaped wave front in the probe path and the single-shot acquisition of the terahertz waveform was realized by using differential detection and phase offset methods. Utilizing the technique, the abrupt variations in the amplitude and carrier-envelope phase of the terahertz waveform were accurately measured and analyzed at the ablation threshold. The technique supplied an important diagnostic tool for monitoring the ultrafast laser ablation process. In 2023, Dong JL et al. developed a single-shot ultrafast terahertz photography system to capture multiple frames of a complex ultrafast scene[55]. Figure 23(d) exhibits the schematic diagram of the system. The initial probe beam was split into four sub-pulses which were multiplexed in both the time and spatial-frequency domain by using four Ronchi gratings with different angles. Subsequently, these four sub-pulses were recombined to form the final probe beam. Then, the probe beam co-propagated with a terahertz beam that carried the temporal evolution of an ultrafast scene. Frames of the ultrafast scene were separately recorded on the four probe sub-pulses via EO sampling, which were captured by a CCD. Finally, these frames were separated in Fourier space and thus were extracted and reconstructed. The technique provided a powerful tool for the investigation of non-repeatable or destructive ultrafast events. In summary, it could be said that these related techniques endowed unique testing abilities from different perspectives for terahertz focal-plane imaging.

3.5 Future development of terahertz focal-plane imaging

To this date, the terahertz focal-plane imaging technique has become increasingly mature and its value has been sufficiently demonstrated. Nowadays, its development was the

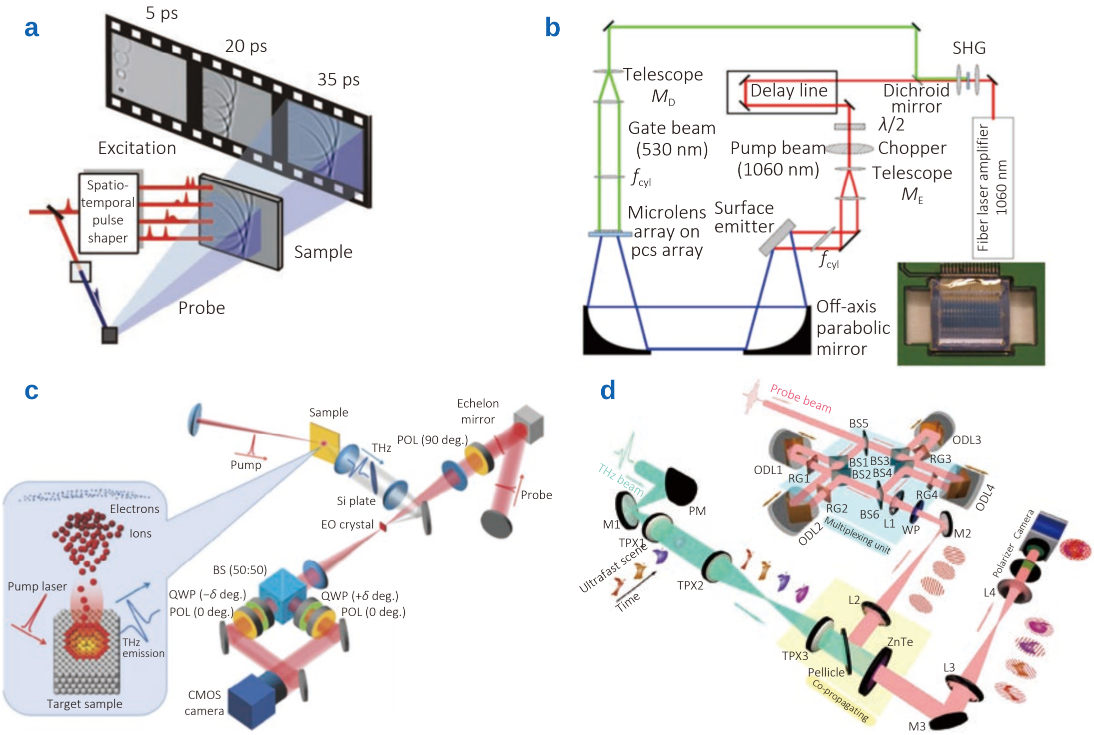

Fig. 23 | Development of related technology. (a) Generation and observation of terahertz phonon-polariton waves in a $LiTaO_3$ crystal. (b) Terahertz detection with a 16-channel photo-conductive antenna array. (c) Observation of the terahertz radiation from the surface of a target material during the initial laser ablation process. (d) Single-shot ultrafast terahertz photography for capturing the evolution of a complex ultrashort event. Figure reproduced with permission from: (a) ref.[197], Science; (b) ref.[41], (c) ref.[201], (d) ref.[55], under a Creative Commons Attribution License.

transition from a laboratory to practical applications. To achieve the transition, it still has to overcome some technical bottlenecks such as how to reduce the size and price of the system as well as how to further enhance the SNR and resolution of the system. Currently, almost all terahertz focal-plane imaging systems adopted a femto-second laser amplifier as an optical source, which seriously limited applications of the technique in real world scenarios. If a laser oscillator could be used to excite and detect the terahertz radiation, it was promising to improve the portability of the system. Of course, it required higher effective terahertz emitters and more sensitive terahertz array sensors. Recently, investigations of advanced photo-conductive antennas[200,202–203] and novel EO crystals[204–206] offered possibility for the aim. In addition, some deep learning algorithms has been successfully introduced into terahertz imaging with the advancement of artificial intelligence technology[207–208]. Utilizing these algorithms, more detail information could be effectively extracted in terahertz imaging and the imaging quality could be further upgraded. Besides, some terahertz metamaterial sensors have been also applied in terahertz imaging to strengthen the interaction between substances and localized terahertz fields for improving the imaging contrast[209–210]. To sum up, it can be expected that the terahertz focal-plane imaging technique will show powerful application values in industrial inspection soon based on its technical superiorities.

4 Terahertz pulse time-domain holography

Terahertz pulsed time-domain holography (PTDH)[211] is an imaging technique that combines the capabilities of broadband terahertz time-domain spectroscopy with the principles of digital holography. Unlike continuous-wave systems, and similarly to focal-plane imaging, PTDH utilizes short terahertz pulses that provide direct access to time-resolved measurements. As it will be shown below, in the aspect of the fast detection of time-resolved terahertz field, PTDH is similar and may even repeat the principles of terahertz focal-plane imaging technique, in the case when the terahertz radiation if focused on the electro-optic crystal. The cornerstone of terahertz PTDH is the mandatory use of wave propagation equations to study the dynamics of the terahertz pulses in spatio-temporal and spatio-frequency domains[59,64,212–216] as well as the formation of the hyperspectral object images from broadband coherently-detected complex-valued diffractive patterns[57,58,64,216].

4.1 Basic principles of terahertz PTDH

In PTDH, data acquisition is performed using coherent detection techniques of the terahertz field[169] with femtosecond laser pulses. The result of such measurements is not the envelope or power of the radiation, but the spatial distribution of the electric field itself. This allows extraction of information not only about the field amplitude, but also about the phase, and across all spectral components.

Figure 24 presents a conceptual diagram illustrating the capabilities of the terahertz PTDH. On one hand, this technique can be used for conducting experimental measurements of the optical properties and topology of various objects (see the orange "Object Characterization" blocks on the left in Fig. 24) and the direction from "Problem statement-2" to "Result-2". On the other hand, it is possible to numerically predict the diffraction properties of such objects (see the sequence of actions from the "Problem statement-1" block to "Result-1" on the same figure for the "Object Characterization" case), as well as to evaluate the effectiveness of sets of modulation components used for forming wideband electromagnetic fields possessing a specific spatio-temporal and/or spatial-spectral structure (the blue "Wavefront Metrology" blocks in the same figure). In the latter case, significant scientific interest lies in investigating the interaction of such fields with obstacles and analysing their stability against various types of interference. Such tasks can also be addressed through experimental measurements, which are indicated as "Problem statement-2" for obtaining "Result-2" in the figure.

The terahertz PTDH has several significant advantages compared to terahertz time-domain spectroscopy techniques, as it involves measurements in a collimated beam, which in practice means the possibility of stationary placement of the object in any area of space within the beam radius. This is often required when performing real-time measurements. For example, the achievable resolution, which is comparable to the wavelength, is significantly higher than that of the competing raster scanning focal-plane terahertz time-domain imaging technique, where the resolution is limited by the size of the beam waist radius[57]. In addition, the configuration of terahertz PTDH in the practical implementation of measurements allows minimizing the number of optical elements specially designed for use in the terahertz spectral range, since field registration is performed by a scanning aperture or a wide-aperture crystal coupled with a matrix receiver directly in the collimated beam that has passed through the object. In this configuration, the reconstruction quality does not depend on the optical elements used in the setup.

The terahertz PTDH combines the following aspects:

(i) Optical layouts for registering the wide terahertz wavefront in the form of spatio-temporal profiles. Here the diffracted terahertz field can be detected both by raster scanning and by means of a wide-aperture electro-optic crystal conjugated with a matrix photodetector, partial case of which is the focal-plane imaging technology.

(ii) Mathematical methods for calculating diffraction of monochromatic components of broadband radiation, used for both the formation of object images and the analysis of the propagation dynamics of complex-structured wave fields.

(iii) Numerical data processing techniques including digital signal processing (signal extraction based on the used observation model) and iterative algorithms, e.g. for expanding the field of view and increasing spatial resolution.

4.2 Terahertz PTDH layouts

Terahertz PTDH employs several detection configurations for wavefront acquisition: aperture-scanning techniques (include aperture[57], slit[218], and diaphragm-lens[68] scanning), antenna

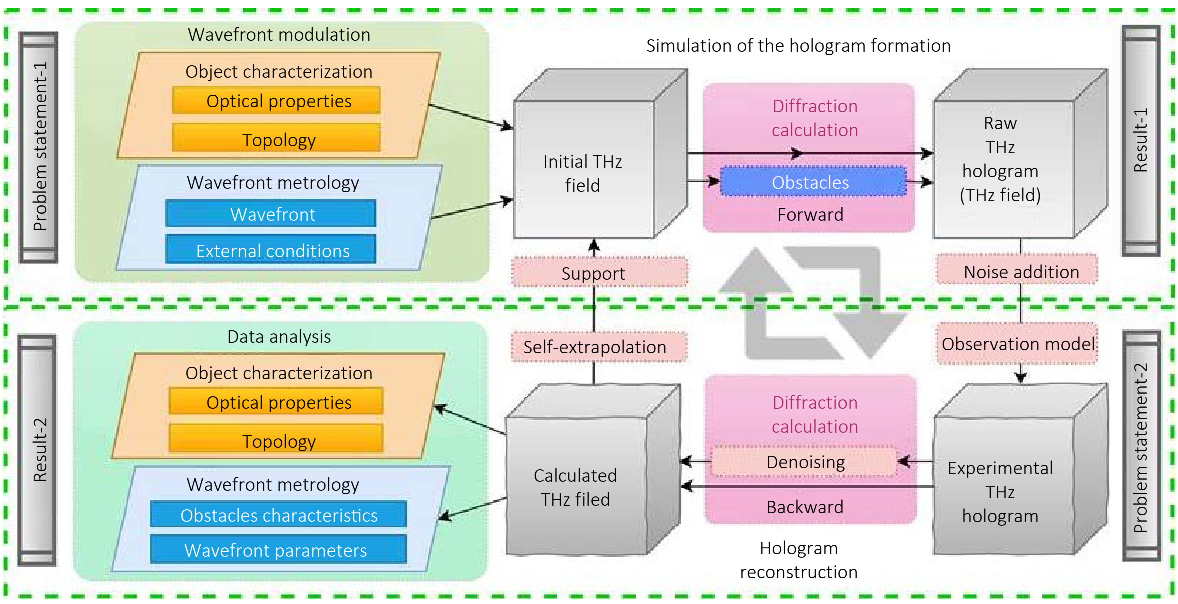

Fig. 24 | Conceptual illustration of terahertz pulsed time-domain holography.

scanning[219–221] and wide-field detection systems[56,65,222–223].

4.2.1 Aperture-scanning techniques

Figure 25 illustrates two detection configurations both relying on a scanning pinhole and a single-pixel detector employing either an electro-optic crystal (Fig. 25(a)) or a photoconductive antenna (Fig. 25(b))[216]. These approaches are based on the most widespread detection manners, implementing electro-optic and photo-conductive mechanisms, respectively. However, other detection mechanisms are also known[224], including air-biased, electro-optic, acoustic, liquid-based, and fluorescence-based methods. Theoretically, these mechanisms allow for spatially-resolved detection of terahertz time profiles. The impact of the raster scan parameters was studied in several works[57,225].

Raster scanning of an expanded terahertz field encounters a fundamental limitation, which manifests in the inherent trade-off between spatial resolution and signal-to-noise ratio when working with low-energy pulsed sources[226]. To overcome this constraint, a modified detection scheme can be employed, incorporating an additional lens that is optically conjugated with the scanning diaphragm and moves synchronously with it during the raster scanning process (Fig. 26).

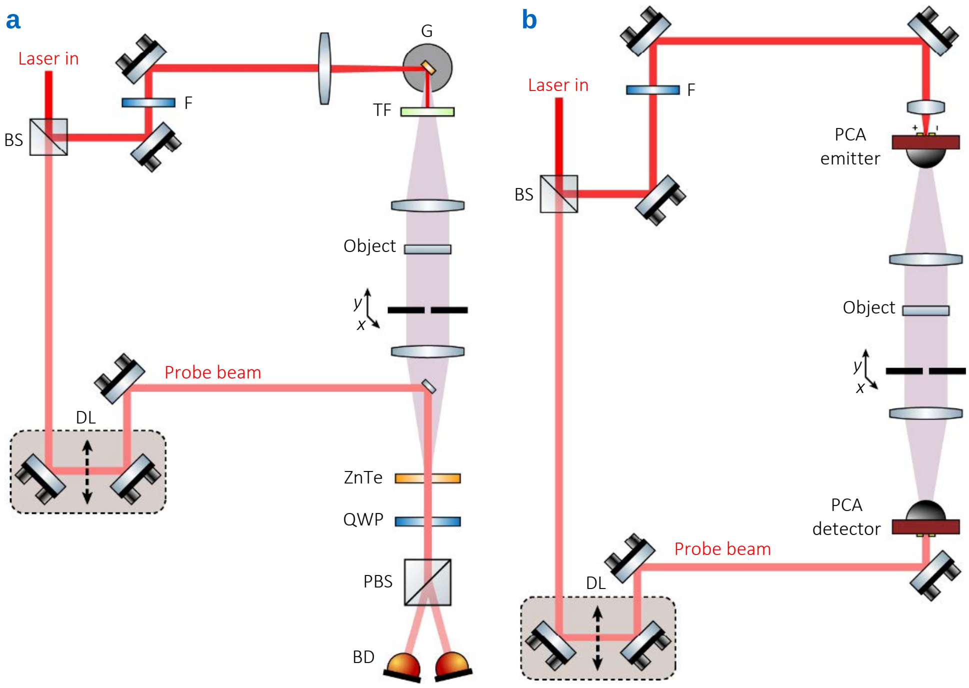

Fig. 25 | Schematic diagrams illustrating pinhole-scanning configurations for PTDH: (a) electro-optic crystal, (b) photoconductive antenna detection systems[216].

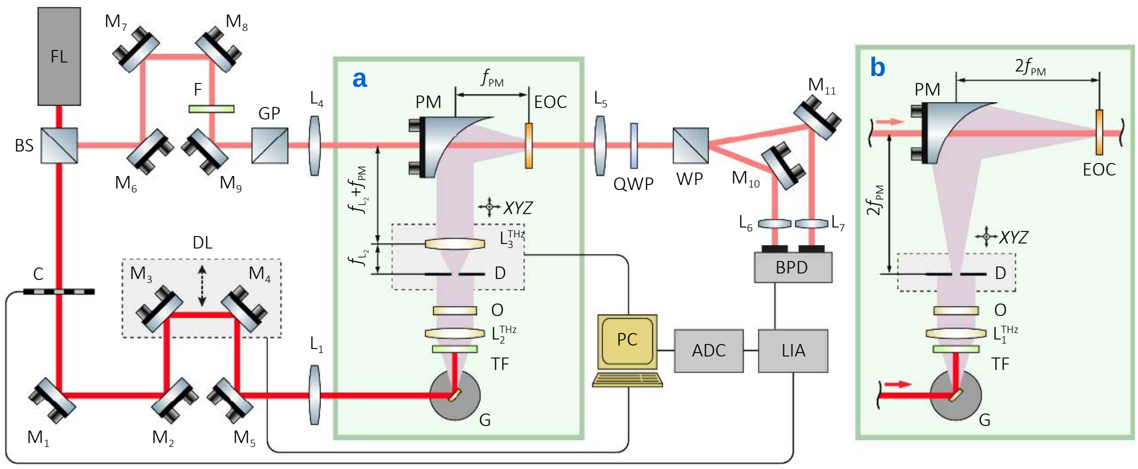

Fig. 26 | Schematic of terahertz PTDH experimental setup, comparing two raster scanning configurations: (a) diaphragm-lens and (b) a conventional diaphragm-only system (partially adapted from ref.[68]). The diaphragm-lens system enables collimation of the spherical wavefront produced by diffraction at the diaphragm aperture. Consequently, it achieves a substantial reduction in energy losses during radiation propagation and enhances the detected signal compared to conventional pinhole-only scanning.

The performance of the diaphragm-lens scanning configuration was evaluated through experimental registration of broadband pulsed Bessel-Gaussian beams[68] alongside numerical modelling (Fig. 27). The experimental validation was conducted under challenging low-power conditions, utilizing a terahertz source generating approximately 30 μW average power. Under the demanding conditions, successful detection was only achievable using the diaphragm-lens system (Fig. 27(a, b)), whereas conventional diaphragm scanning failed to produce any detectable signal.

Numerical simulations enabled direct comparison between the two scanning methodologies. In Fig. 27(c, d), the side-by-side arrangement of results displays spatio-temporal and spatio-frequency distributions, with the upper sections representing conventional diaphragm scanning and the lower sections showing the enhanced diaphragm-lens configuration under identical conditions. The results demonstrate that while using identical diaphragm sizes, the pinhole-lens system achieves substantial signal amplification of 2–2.5 times in the EO crystal plane. This enhancement enables improved spatial resolution in practical applications, as it permits the use of smaller diaphragm apertures while maintaining adequate signal-to-noise ratio, thereby overcoming a fundamental limitation in pulsed terahertz imaging systems. Numerical modeling further established the superiority of the diaphragm-lens system, showing it provides more reliable wavefront reconstruction by eliminating the influence of quadratic phase aberrations inherent to the single-diaphragm configuration[68].

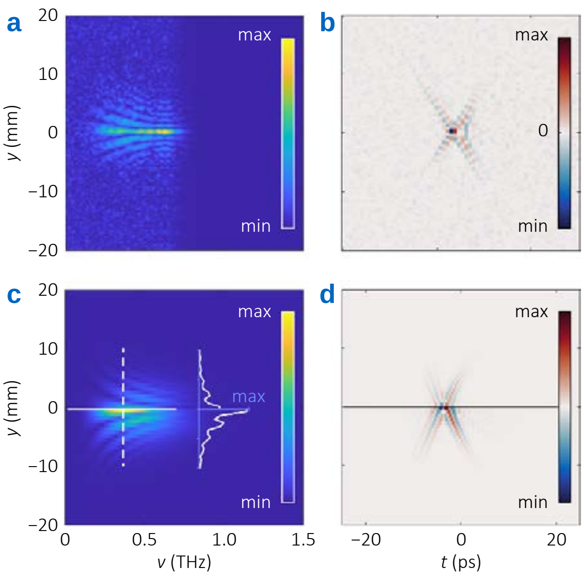

Fig. 27 | Application of the diaphragm-scan system in terahertz PTDH. Spatio-temporal and spatio-frequency imaging of a terahertz pulsed Bessel-Gaussian beam in the focal plane: (a, b) experimental results obtained with the diaphragm-lens system; (c, d) the corresponding numerical simulations comparing both detection schemes side-by-side (upper: single diaphragm; lower: diaphragm-lens system)[68].

4.2.2 Antenna-scanning techniques

Among other possible raster-scanning approaches for broadband pulsed terahertz field detection a measurement with a near-field photoconductive antenna equipped with a scanning tip should be mentioned. This approach was successfully implemented in refs.[219–221]. Although these works do not demonstrate numerical wavefront propagation inherent to holographic techniques, they measure the field distribution not in the focal plane, but rather within divergent diffraction volume, making them prospective candidates for conjugation with PTDH.

4.2.3 Wide-field detection

While raster-scanning detection is conceptually simple, its necessity for a 3D scan (across two spatial and one temporal coordinates) creates a fundamental trade-off between data acquisition time, spatial resolution, and the measurable field of view. This often forces a compromise, limiting the practical achievement of the high three-dimensional resolution (in *x*, *y*, and *t*) that pulsed terahertz holography theoretically offers. To overcome this limitation, a faster full-wavefront detection method was proposed (Fig. 28)[56,65,222–223].

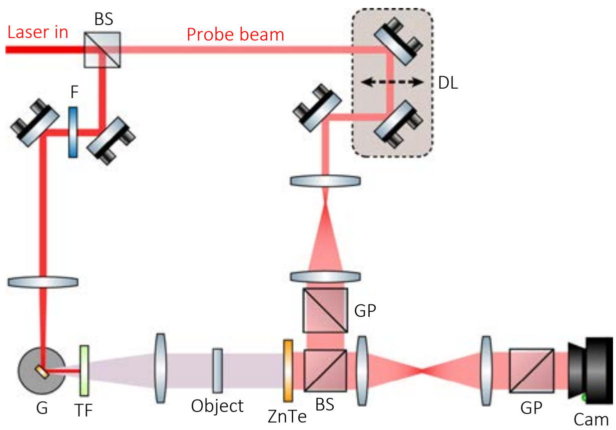

Fig. 28 | Schematic diagram illustrating the single-scan terahertz field spatio-temporal detection[216].

This technique uses a large-area electro-optic crystal (EOC) to encode the terahertz field onto the polarization of an expanded probe beam, requiring only a single temporal scan to capture the entire wavefront. This detection can be implemented in two primary configurations. The codirectional configuration minimizes the probe beam's intensity loss; however, it reduces the collection angle of the scattered terahertz field, limiting the resolution of the registered field. In contrast, the retroreflected configuration shortens the object-to-crystal distance, thereby increasing the spatial collection angle and improving resolution, albeit at the cost of significant probe beam attenuation due to double-passing the beamsplitter. Furthermore, inhomogeneities in the terahertz field distribution across the crystal can lead to non-uniform phase retardation in the probe beam[217]. Furthermore, the entire holographic detection system, particularly the retroreflective configuration, was specifically engineered for practicality, with all optical mounts designed for 3D printing and released as open-source hardware[65,222].

The measurement principle implemented in this approach using partially-crossed polarizers is illustrated in Fig. 29, and the a, b, and c respectively represent the zeros, negative and positive points.

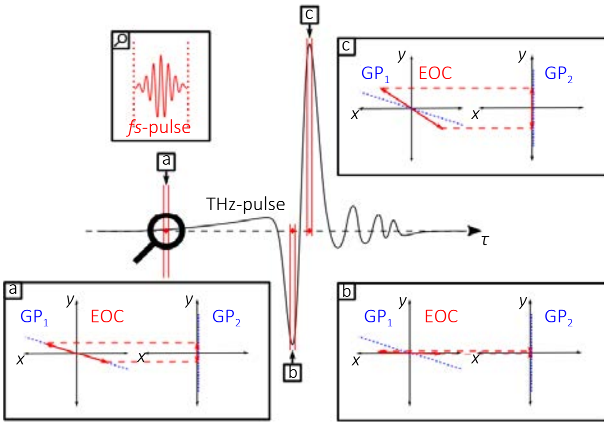

Fig. 29 | Illustration of the temporally-resolved detection of terahertz field strength. Figure reproduced with permission from ref.[65], Optica Publishing Group.

4.3 Theoretical aspects and algorithms of PTDH

The mathematical model of the method is based on the scalar theory of diffraction to describe the transformation of a broadband wavefront as it propagates through objects and free space[57,60,216,227]. In simple numerical simulation tasks (see "Problem statement-1" in Fig. 24), the simulated terahertz field is assumed to be ideally collimated. Consequently, its wavefront is assigned a spatial Gaussian amplitude distribution and a flat phase profile. In the time domain, the original signal is a single-cycle terahertz pulse with a duration of several picoseconds. But achievement of the best matching with the experimental profiles is possible when the terahertz radiation is carefully simulated just after the terahertz source with maximum details[68,214].

4.3.1 Computational framework and object parameterization

The object under study is computationally parameterized by its transmission function[57,63,60]. In the context of wavefront synthesis and analysis, these objects are referred to as modulation components. Examples of such components include spiral phase plates[65,212], phase axicons[59,68], and specialized composite elements like broadband vortex generators[66−67], as well as more complex devices utilizing metamaterials for this frequency range[218].

The interaction of the collimated terahertz beam with these modulating components is described in the spectral domain. The general principle involves modifying the original terahertz field's spatial-spectral distribution by multiplying it with the spatial transmission function of the modulator. This function can be frequency-independent or frequency-dependent, and can act as an amplitude or phase mask.

When applied to object characterization, the modulator represents the sample under study, which alters the amplitude and phase of the incident terahertz radiation. While the technique can be applied to both transmission and reflection modes, the description here focuses on transmission objects due to the current technological challenges associated with reflection-mode setups. Within this framework, several key computational tasks can be addressed.

1) Calculating an object's surface profile based on its known refractive index and the measured spatial distribution of the phase delay.

2) Determining the optical characteristics of a sample based on known surface relief data and the measured phase delay.

3) Identifying a material, its constituents, or impurities from its absorption spectrum, given information about its thickness and the measured phase distribution.

4) Blind identification of material, thickness, and optical characteristics based on phase information retrieved from several independent measurements.

The corresponding algorithmic approaches for solving these tasks rely on a spectral methodology, where wavefront propagation is calculated using scalar diffraction integrals across all frequency components of the pulsed field.

In PTDH, the processing of data acquired as spatio-temporal profiles utilizes numerous techniques originally developed for terahertz spectroscopy. A notable feature is that when working with spatial-spectral phase distributions, information about the absolute phase can be retrieved using phase-unwrapping algorithms that operate not only in the spatial domain but also across the frequency domain.

Among the data processing techniques, a specialized iterative broadband algorithm for extrapolating the complex wavefield amplitude beyond the sensor's recorded area was particularly developed[217]. This algorithm is highly relevant for fast coherent detection systems in which wide field sensors are typically limited in size. If a non-zero terahertz diffracted field existed outside the crystal's active aperture, this iterative post-processing algorithm can be applied to the recorded data to recover the original field distribution. The core idea of this technique is based on the assumption that a portion of the diffraction pattern was truncated at the sensor's boundaries and can be numerically reconstructed. The algorithm iteratively alternates between the spatial and frequency domains, applying constraints in each, and its convergence is significantly improved by using an apodizing mask.

The application of this algorithm leads to extension of the field of view and enhancement of the effective spatial resolution beyond the classical diffraction limit achieved for the lower-frequency spectral components.

4.3.2 Data denoising algorithms

The detection of terahertz fields is fundamentally limited by source power, with typical values for common emitters like photoconductive antennas being on the order of microWatts. This low signal level necessitates sophisticated denoising strategies, especially in wide-field holographic setups where the signal is spatially distributed. A foundational study systematically addressed the critical trade-off between spatial resolution and SNR inherent in the method[57]. The research focused on the use of a scanning pinhole, where a smaller aperture improves resolution but drastically reduces the signal energy reaching the detector. This makes the signal resistant to detector noise, which remains constant regardless of pinhole size. Through numerical simulations that incorporated measured noise models, the study demonstrated the method's surprising tolerance, showing that object features could be reconstructed even when noise amplitudes were comparable to the signal at the hologram plane. The analysis concluded that an optimal pinhole diameter (e.g., 1.5 mm in their setup) could be identified to balance resolution and SNR effectively, establishing a crucial pre-processing step before applying advanced numerical denoising.

Building upon this understanding of noise origins and the critical hardware trade-offs, the further research was focused on adapting modern block-matching algorithms to the multi-dimensional data of PTDH[61]. Two key algorithms were investigated: the video block-matching and 3D (VBM3D) filtering algorithm for denoising spatio-temporal data, and the complex-domain BM3D (CDBM3D) algorithm for direct processing of complex-valued spatio-spectral data. It was shown that while VBM3D is effective for visualizing wavefield dynamics in time, the CDBM3D algorithm, which exploits the correlation between amplitude and phase, provides superior accuracy for phase image reconstruction. A hybrid approach, using VBM3D for "soft" prefiltering of temporal data before applying CDBM3D to the spectral domain, yielded the most precise results for object profile reconstruction.

Subsequent work addressed the specific case of holography with a balanced detection system, where the noise follows a Skellam distribution rather than a Gaussian model[62]. The noise variance in such a system is signal-independent. For this optimized noise model, the study introduced and validated a more advanced algorithm, the cube complex-domain filter (CCF). Unlike CDBM3D, which processes each frequency layer independently, CCF performs block-matching simultaneously across the entire 3D hyperspectral data cube (two spatial and one spectral dimension). The combination of temporal filtering (VBM3D) and this enhanced spectral filtering (CCF) was demonstrated to expand the usable dynamic range of terahertz frequencies and provide a significant qualitative enhancement in image contrast and spatial resolution, particularly for the lower-frequency spectral components.

A detailed comparison of terahertz focal-plane and PTDH techniques reveals their conceptual kinship, which manifests in partial overlaps on both methodological and applicability levels. This is illustrated by specific cases: the focal-plane technique sometimes employs numerical wavefront propagation—a key feature of PTDH (e.g., refs.[47,180])—while a distinct application of PTDH itself is the analysis of terahertz field evolution at the focus (as discussed in refs.[60,67]). These similarities and distinctions between the techniques stem from their independent, parallel development by different research teams.

4.4 Applications of PTDH

The ultrabroadband pulsed terahertz radiation offers distinct advantages for material characterization, particularly as it reveals characteristic molecular absorption resonances across various organic compounds, thereby facilitating simultaneous imaging and spectroscopic analysis. PTDH enables quantitative extraction of material optical constants, e.g., refractive index distribution, and achieves superior spatial resolution compared to time-domain focal plane imaging.

4.4.1 Retrieval of object properties

The principal advantage of coherent detection in PTDH lies in its capacity to extract quantitative object properties from the recorded complex-valued field. The amplitude of the wave provides insights into the material's absorption coefficient, while the phase delay encodes information about the refractive index and physical thickness. This allows for solving inverse problems such as calculating surface relief from known optical constants or determining material characteristics from a known profile. A demonstration of this opportunity was presented in[57], where the authors were the first to apply PTDH for quantitative phase imaging of an object that only modulates phase. The experiment involved a custom-fabricated Teflon target with a gradient-step relief, specifically designed to test the method's ability to resolve both gradual and abrupt topological changes. Through a pinhole-assisted raster scan of the collimated terahertz beam and subsequent numerical back-propagation of the wavefront, the object's relief was accurately reconstructed. The research conclusively showed that phase imaging was indispensable for resolving the object's topology and that multi-spectral synthesis (Fig. 30) was crucial for achieving high-fidelity reconstruction, establishing a new benchmark for metrological applications of PTDH.

In work[58], the authors investigated the optical properties of sodium polyacrylate in the terahertz range. It was demonstrated that accounting for material dispersion is essential for the accurate reconstruction of an object's phase and relief in terahertz PTDH imaging. The work highlighted that neglecting dispersion introduces significant phase uncertainty, which becomes particularly problematic when visualizing objects with a complex spatial distribution of the refractive index. This research expanded the applicability of terahertz PTDH to include dispersive materials, a consideration that is also highly relevant for the challenging task of locating objects embedded within complex, dispersive media.

In a related study[217], researchers demonstrated the application of terahertz PTDH for reconstructing spectrally selective objects. They used a specialized test object—an opaque mask with letters that were transparent only within specific terahertz frequency bands. This setup allowed the authors to simulate and reconstruct a spatially inhomogeneous object whose transmission depended on the illumination frequency. The reconstruction was performed using an iterative algorithm, which successfully resolved both the spatial and spectral features of the object. The method led to a substantial improvement in reconstruction quality, approximately halving the mean root square error, and proved effective for objects with complex spectral-spatial properties. This work underscores the technique's potential for spatio-temporal metrology of broadband wavefronts and imaging of spectrally complex structures.

Terahertz PTDH has been adapted for biomedical diagnostics[228], specifically for the analysis of lyophilized blood plasma to identify markers associated with diabetes[63]. This approach addresses key challenges in studying biological samples: liquid blood plasma is unstable over time, and whole blood contains cells that dominate the THz response, obscuring the signal from glycated proteins. Lyophilized plasma pellets provide a stable, transportable alternative with low THz absorption, making them ideal for transmission-mode analysis.

The core of the method is its sensitivity to spatial inhomogeneities in the pellet's refractive index, which arise from variations in the concentration of glycated proteins like albumin—a key indicator of diabetes. While traditional TDS with raster scanning is too slow for practical clinical use, PTDH enables rapid, single-scan acquisition of the entire wavefront, making it suitable for express diagnosis.

The research methodology, outlined in Fig. 31, combines physical and numerical experiments. The physical stage involves preparing pellets from diabetic and healthy plasma and characterizing them with TDS. The numerical stage synthesizes a realistic terahertz hologram, incorporating noise and detection artifacts, to develop and validate the reconstruction algorithms. This workflow establishes a protocol where a measured pellet's hologram can be processed to extract its optical properties, which are then statistically analyzed against a database for diagnosis. This positions PTDH as a promising tool for fast, reliable biomedical inspection.

4.4.2 Wavefront metrology and design of modulating components

Terahertz PTDH establishes itself as an efficient tool for the multi-dimensional analysis of complex-structured, broadband wavefields across spatial, angular, temporal, and frequency coordinates, while also serving as a direct terahertz-domain analogue of modern spatio-temporal metrology techniques developed for the visible range, namely the TERMITES[229] and INSIGHT[230]. The unique capability of PTDH in this context stems from its fundamental detection principle: EO sampling. Unlike these optical techniques that

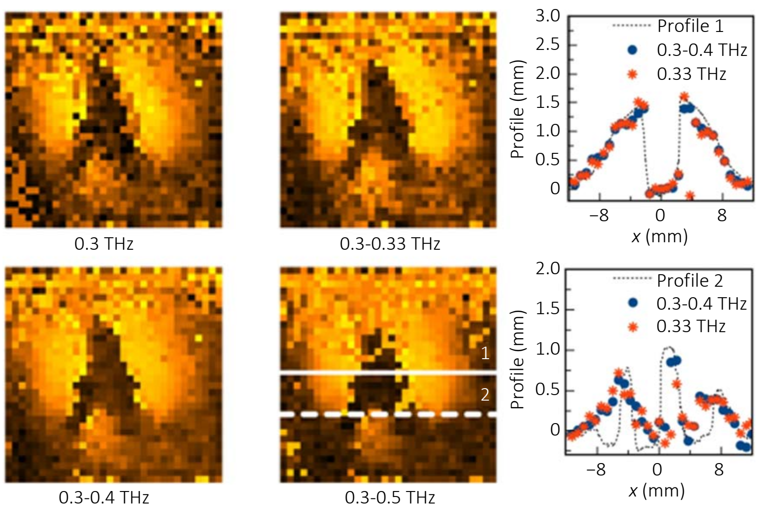

Fig. 30 | Comparative reconstruction of an object's surface profile using different terahertz spectral bands. Cross-sections along the white lines in images corresponds to 0.3–0.5 THz are quantitatively compared in the right column. Figure reproduced with permission from ref.[57], IEEE.

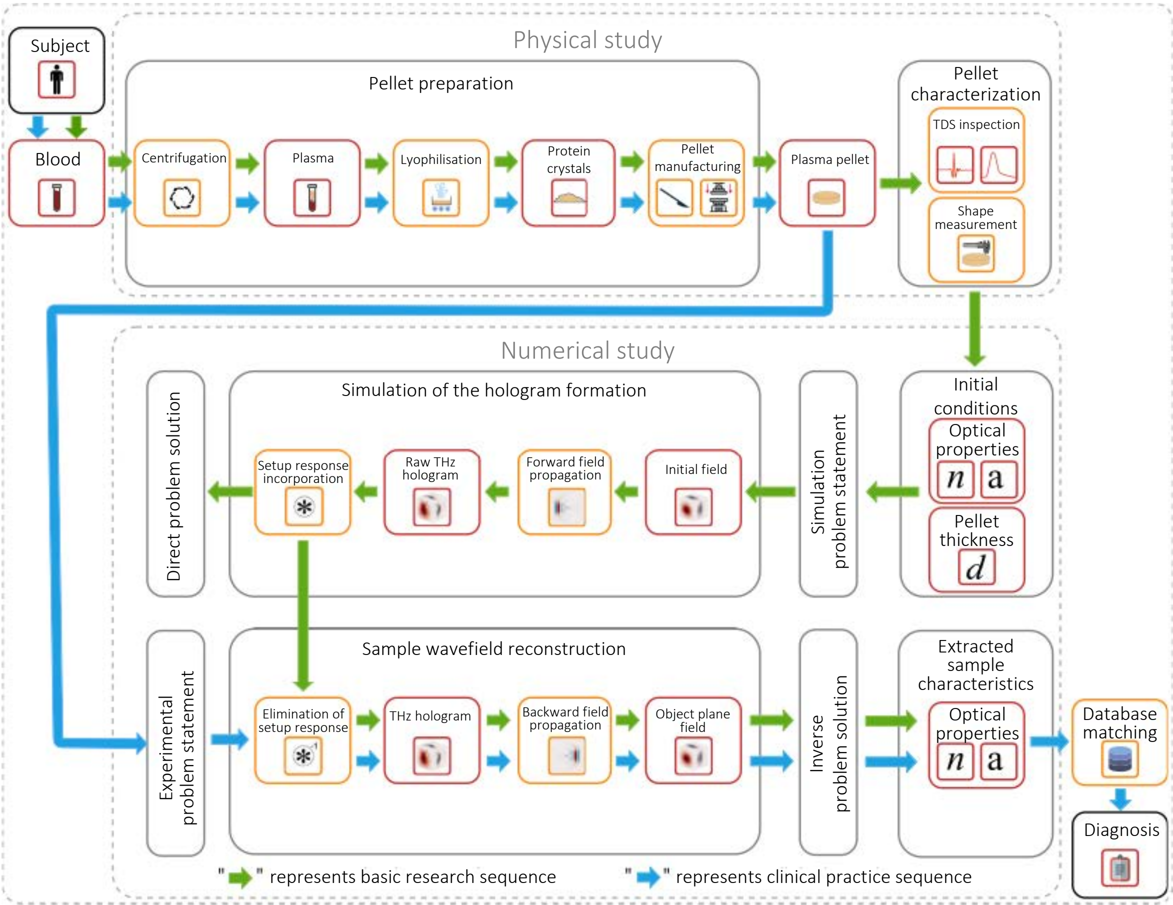

Fig. 31 | Conceptual workflow for diabetes diagnostics using terahertz PTDH. The diagram outlines the methodology from sample preparation (lyophilized blood plasma pellets) to diagnosis, integrating both physical experiments and numerical modeling to enable fast, single-scan holographic assessment[63].

rely on measuring correlation functions, PTDH provides a direct measurement of the electric field's temporal evolution. This grants immediate access to the full phase information in the Fourier spectrum and uniquely enables the complete characterization of single-cycle field oscillations, a feat that remains challenging in the visible domain. Nevertheless, this technique presents several practical limitations. The spatial and temporal resolution in the THz range is inherently constrained by the longer wavelengths and limited source power. Furthermore, the method is inherently data-intensive. A single measurement of a hyperspectral wavefront can require gigabytes of storage for the spatio-temporal data cube. While this data volume is significant, it is politely comparable to the demands of other advanced metrology methods; for instance, a raw dataset from a TERMITES measurement in the visible range can be an order of magnitude larger. This highlights a common challenge in the field of ultrafast spatio-temporal metrology, where capturing complex phenomena, such as the dynamics of highly scattered fields, pushes the limits of both computational resources and physical measurement constraints[231].

The previously outlined capability of PTDH for multi-dimensional analysis has been directly applied to study the propagation dynamics of spatio-temporal and spatio-spectral terahertz fields. In the work[59], the propagational dynamics of pulsed broadband terahertz Gauss-Bessel beams are examined numerically, while ref.[68] contains experimental data. Figures 32 and 33 illustrate the beam evolution in the spatio-temporal and spatio-spectral domains, respectively, showing pulse reshaping during propagation. The characteristic X-shaped envelope is uniquely visible in the spatio-temporal distribution (Fig. 32). The analysis[59] in further revealed a pronounced spatio-temporal coupling, manifested by a significant reshaping of the beam's leading edge during propagation.

The study provides a detailed analysis of Gauss-Bessel beam properties. The results demonstrate that interference from different axicon sectors produces specific amplitude extrema for individual frequency components (Fig. 34), resulting in a spatially narrow beam profile advantageous for high-resolution imaging. Furthermore, phase velocity analysis reveals a discrepancy with interpretation of the existing experimental data. The calculations indicate sensitivity to sampling step, which leads to apparent superluminal or subluminal behavior depending on the regime.

Using PTDH there is also an opportunity to calculate and study the longitudinal field component using the two transverse ones. Importantly, the technique provides the opportunity to study the evolution of the longitudinal terahertz field component within the volume of its diffraction propagation[214]. Figure 35 presents the normalized spatio-spectral and spatio-temporal profiles of the transverse (top row) and longitudinal (bottom row) terahertz field components following diffraction from a spectral Fresnel filter aperture at two different distances.

The application of terahertz PTDH for the comprehensive characterization of broadband terahertz vortex beams throughout their formation and propagation is demonstrated in work[67]. Terahertz beam modulators based on polarizing components and the geometric-phase effect are reviewed in ref.[66]. Different configurations of such modulators are schematically presented in Fig. 36, which details the transformation of the beam polarization structure after each component and demonstrates the possibility of generation of vortex and cylindrical vector beams with circular or linear polarization.

Work[67] details the development of achromatic multilayer quarter- and half-waveplates, designed to operate across a broad terahertz frequency spectrum. Essential for broadband beam manipulation, these waveplates are realized by stacking birefringent plates and optimizing their thicknesses and crystal orientations (Fig. 37(a)). A Jones matrix formalism provides an analytical model to describe the transformation of the input beam's polarization state as it propagates through the multilayer structure. The optimization performed in work is based on the equalizes the phase retardation between the ordinary and extraordinary waves for all spectral components of interest, achieving a target value (e.g., π for a half-waveplate).

Furthermore, the work proposes a method for constructing an achromatic q-plate. This is achieved by assembling the pre-optimized achromatic waveplates into segmented patterns (Figs. 37 (b, c)), where each segment is specifically oriented. The resulting waveplates and q-plates, arranged in the correct sequence, serve as achromatic devices capable of generating broadband uniformly-topologically charged (BUTCH) beams, in accordance with the scenarios in Fig. 36. The propagation dynamic of such beams was investigated in free space under edge diffraction, where half of the beam was obstructed (Fig. 38)[60].

Analysis of the spatio-temporal and spatio-spectral distributions following beam blocking reveals that, although a strong asymmetry emerges in the spatial amplitude profile, the singular phase recovers and transverse energy circulation is preserved. This conclusion is supported by the analysis of spectral trajectory of the singular point and the phase structure of individual spectral components (Fig. 39).

The self-reconstruction of the BUTCH beam vortex properties, analogous to the behaviour of monochromatic optical vortices, verifies the conservation of topological charge

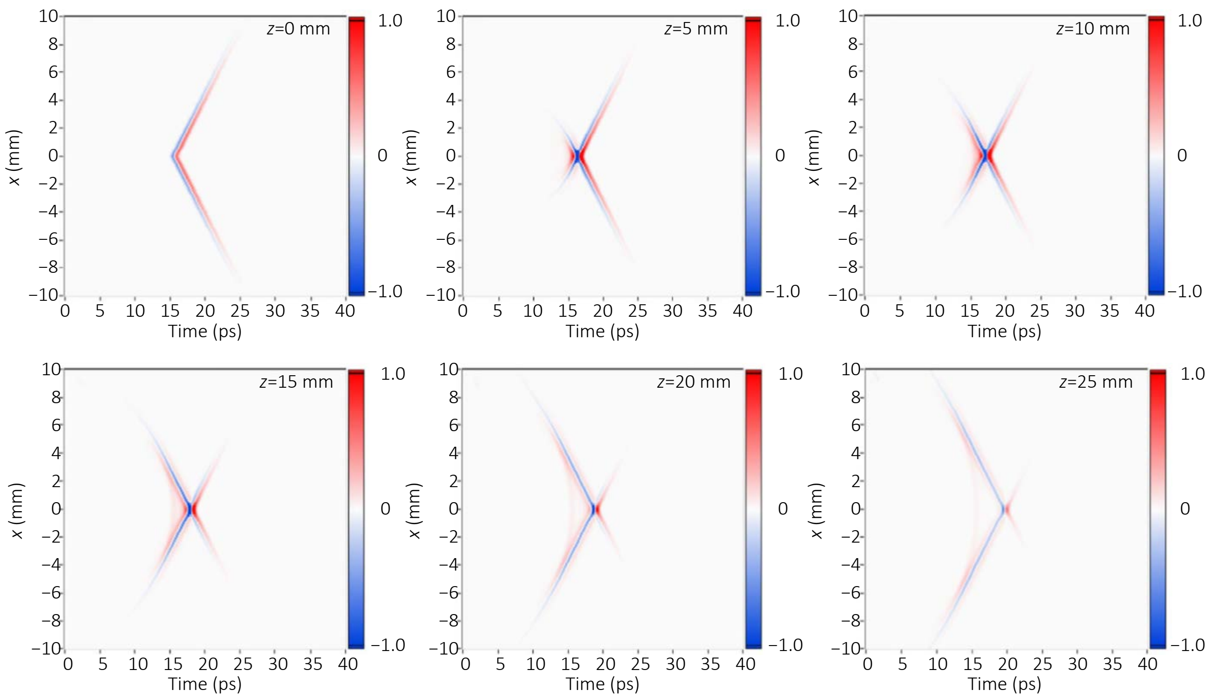

Fig. 32 | Spatio-temporal evolution of a broadband Bessel-Gaussian beam after an axicon. Panels show the THz field in the central plane at successive propagation distances: 0 mm, 5 mm, 10 mm, 15 mm, 20 mm, and 25 mm. Figure reproduced with permission from ref.[59], under a Creative Commons Attribution License.

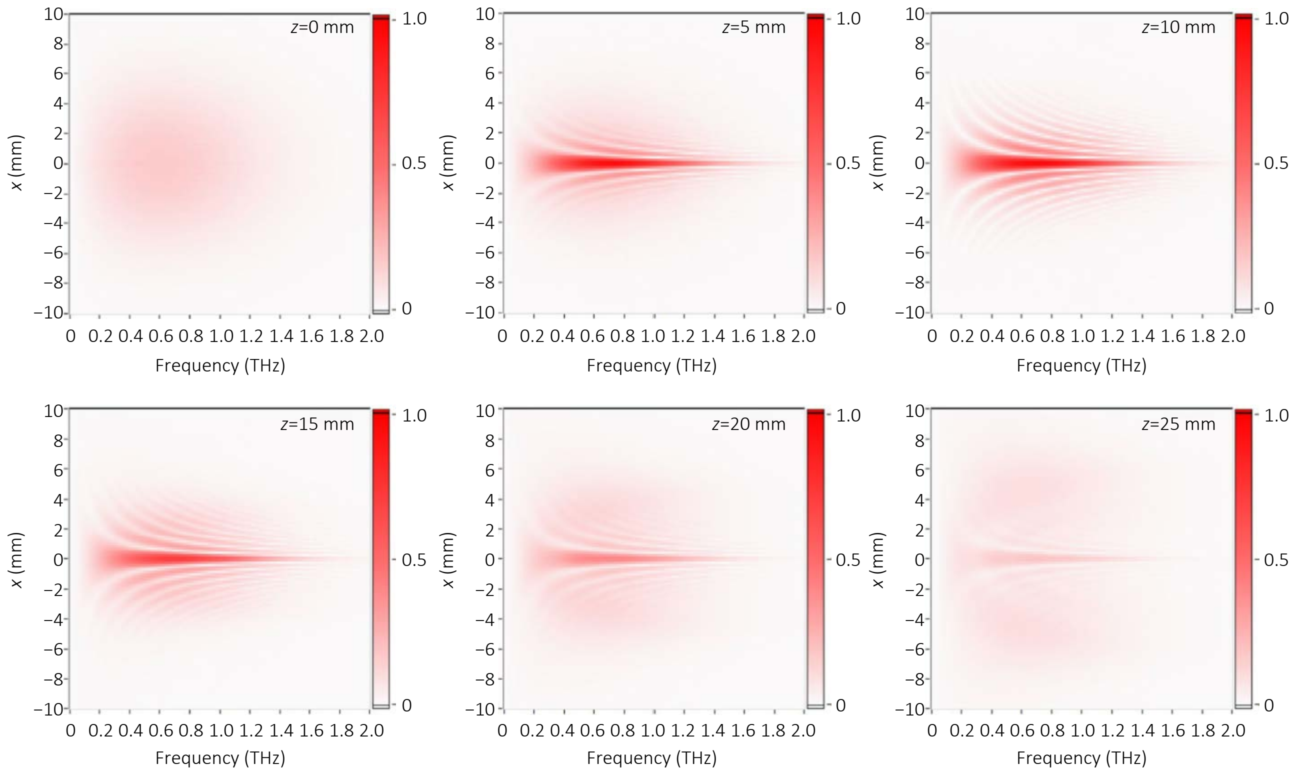

Fig. 33 | Spatio-spectral evolution of a broadband Bessel-Gaussian beam after an axicon. Figure reproduced with permission from ref.[59], under a Creative Commons Attribution License.

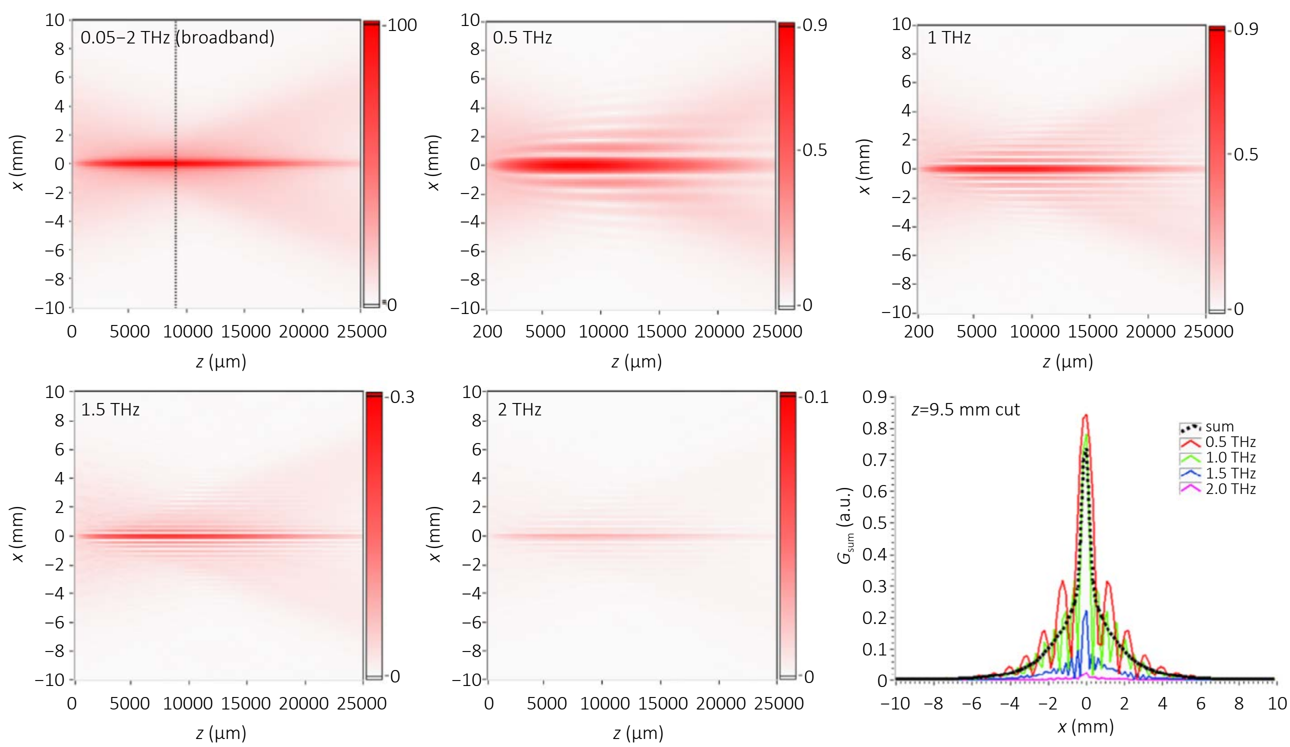

Fig. 34 | Longitudinal patterns of a Bessel-Gaussian beam along propagation distance *z*. Panels show the broadband pulse and its constituent spectral components. The transverse cross-section at the marked position is displayed on the right. Figure reproduced with permission from ref.[59], under a Creative Commons Attribution License.

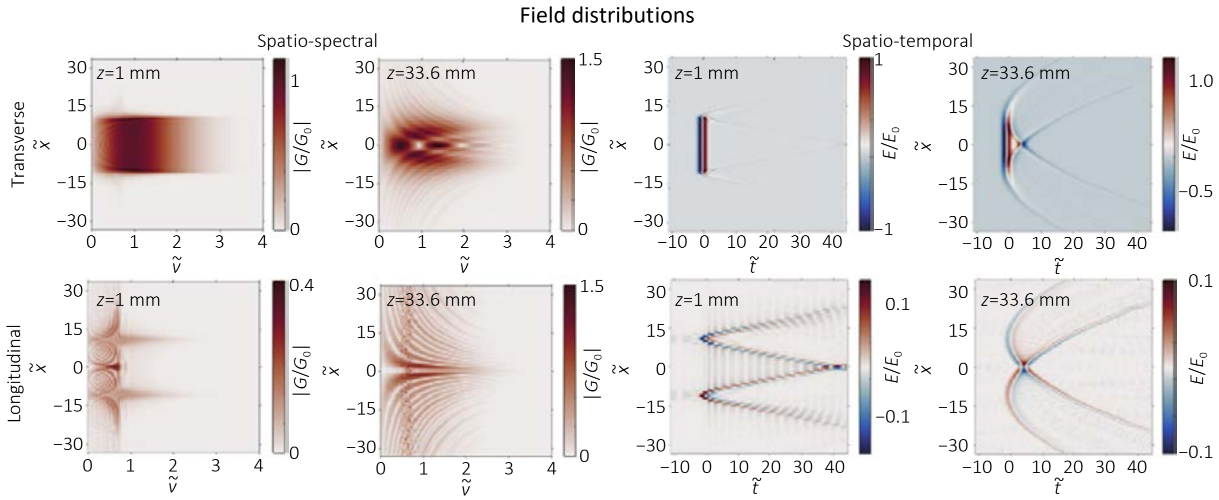

Fig. 35 | Evolution of the terahertz field behind a spectral Fresnel filter. Figure reproduced with permission from ref.[214], under a Creative Commons Attribution License.

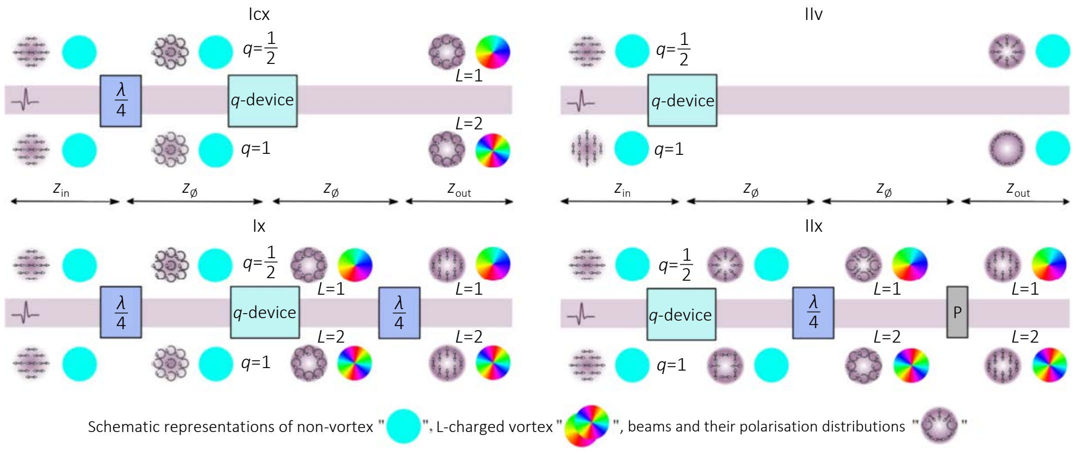

Fig. 36 | Scheme types for terahertz vector and vortex beam shaping. Scheme types for terahertz vector and vortex beam shaping. Two main configurations (I and II) generate vortex beams with circular (Icx) and linear (Ix, IIx) polarizations, and vector beams with cylindrical polarizations (IIv). Each scheme produces beams with topological charges L = 1 and L = 2.

under obstruction and confirms the potential of BUTCH beams for broadband terahertz telecommunications.

The propagation dynamics and interference of BUTCH beams have been a subject of detailed study. Initial research focused on configurations involving the interference of two BUTCH beams with single and binary topological charges[215]. Subsequent investigations, however, revealed that more straightforward and practically significant phenomena are observed when a BUTCH beam with a unit topological charge interferes with a fundamental Gaussian beam[64].

The experimental configuration for studying spatio-temporal and spatio-frequency evolution of terahertz BUTCH beams with integer topological charge employs a dual-interferometer system (Fig. 40). A Ti:sapphire femtosecond laser system with chirped pulse amplification serves as the optical source, split into pump and probe beams. The pump beam passes through a Michelson interferometer with controlled delay, generating two sequential terahertz pulses carrying Laguerre-Gaussian profiles from the terahertz generator G. These pulses are then divided in a terahertz Mach-Zehnder interferometer, where one arm incorporates a beam modulator creating BUTCH beams (Fig. 40(a)) while the other arm maintains Gaussian profiles with intensity compensation. At the detecting ZnTe crystal both arms are combined together. The resulting four-pulse sequence consists of two vortex BUTCH pulses and two matched Gaussian reference pulses (Fig. 40(b)).

When the BUTCH beam undergoes controlled displacement through delay variation in a Mach-Zehnder interferometer, the interference structure shows characteristic rotations of extrema along the frequency axis. This displacement was utilized to implement a spectral encoding scheme. The principle involves summing the spectral density within a specifically optimized receiving aperture for distinct spectral channels. Varying the interferometer delay deforms the

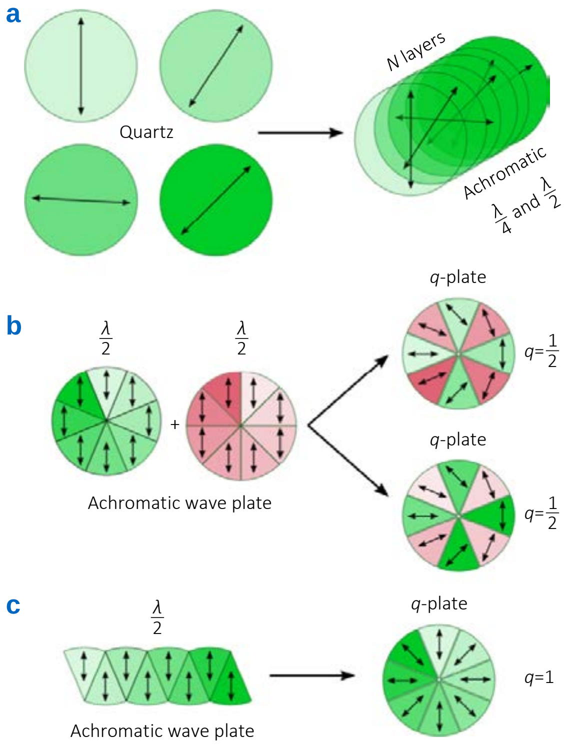

Fig. 37 | Schematic designs of terahertz wavefront-modifying elements. Shown are (a) an achromatic wave plate, (b) a q-plate with a topological charge of q = 1/2, and (c) a q-plate with q = 1. Figure reproduced with permission from ref.[67], under a Creative Commons Attribution License.

helical wavefront, shifting the intensity maxima across the aperture and creating a unique binary signature for each delay position. An optimal aperture shape and orientation were identified to exploit the wavefield's chiral symmetry, effectively halving the number of required measurements. Figure 41 demonstrates the successful operation of this principle for a three-channel system, plotting the normalized signal in each channel against the delay line position. A defined threshold (red line) cleanly converts the analogy signals into a robust binary code, shown above the graph[232]. Thus, PTDH establishes itself as a versatile methodology for applied studies of beam propagation dynamics, providing unparalleled capability for multi-dimensional analysis in the spatial, temporal, and spectral domains. It is noteworthy that a direct analogue of this technique, known as transient acoustic holography, exists in the field of acoustics[233]. Both methods share the fundamental principle of reconstructing a complete wave field from measurements in a single plane to analyse propagation dynamics and extract spatio-spectral characteristics, differing primarily in the nature of the waves they probe—electromagnetic waves in the terahertz regime versus acoustic pressure waves.

5 Terahertz single-pixel imaging

Single-pixel imaging (SPI), also known as computational ghost imaging (CGI), is a novel imaging scheme based on spatial modulation of the light field and computational reconstruction. Its core feature lies in breaking the reliance of traditional imaging on pixel array detectors; instead, it realizes the recovery of the target's spatial information

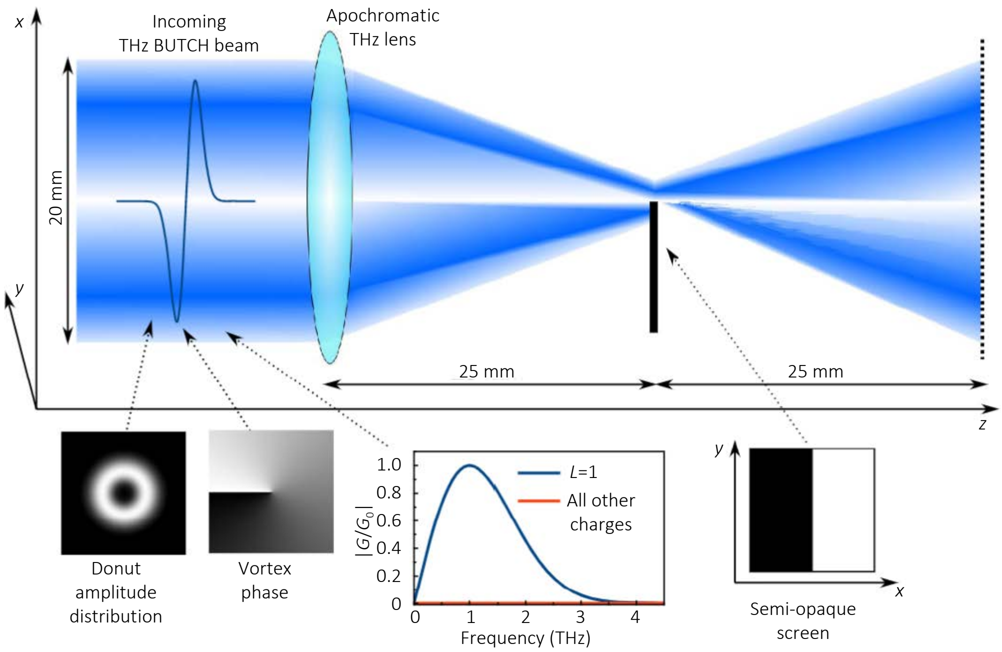

Fig. 38 | Layout of the numerical experiment for a pulsed broadband terahertz vortex beam propagating past a half-blocking screen. Figure reproduced with permission from ref.[60], Optica Publishing Group.

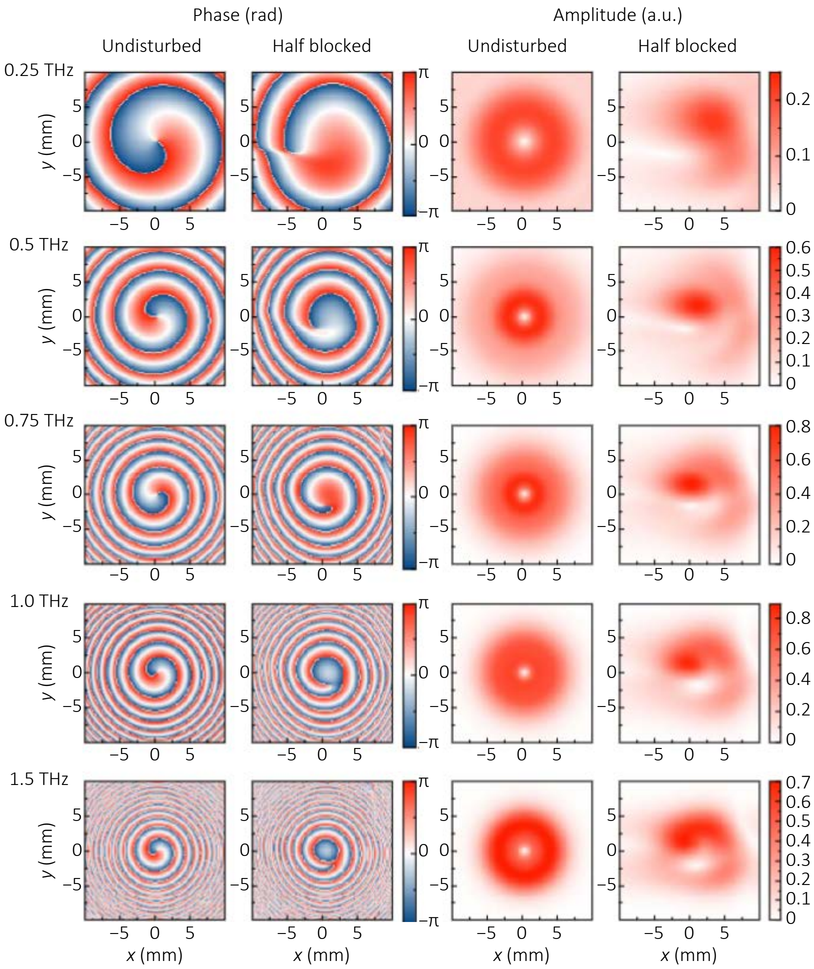

Fig. 39 | Spatial distributions of phase (left two columns) and amplitude (right two columns) for different frequency components of the terahertz BUTCH beam at the focal point. Figure reproduced with permission from ref.[60], Optica Publishing Group.

through intensity measurement by a single-pixel detector and computational algorithms[234], boasting the significant advantage of full-wavelength adaptability[235–241]. The emergence of terahertz single-pixel imaging (THz-SPI) benefits precisely from the breakthroughs in the underlying principles of SPI and the maturity of experimental techniques, thereby providing an innovative solution to the imaging challenges in the terahertz band.

5.1 Development of terahertz single-pixel imaging

In 2008, in a study conducted by Shapiro JH et al. from the Massachusetts Institute of Technology[242], the computational ghost imaging scheme based on spatially modulated measurement and single-pixel detection was systematically proposed for the first time from a theoretical perspective, as shown in Fig. 42(a). This marked the initial establishment of the theoretical framework for single-pixel imaging technology. Addressing the limitations of traditional ghost imaging, which relies on entangled light sources[243] or beam-splitting optical paths[244], the study innovatively introduced a SLM as the core modulation component. It replaced the function of traditional reference optical paths by performing deterministic spatial encoding on beams. In the same year, Duarte MF et al. experimentally verified a SPI system based on compressed sensing (CS) theory for the first time[245], and officially established the technical term "single-pixel imaging". This experimental system is detailed in Fig. 42(b), employed a digital micromirror device (DMD)[246] as the core of spatial modulation, utilizing its flipping characteristic to generate binary pseudo-random modulation patterns. After being modulated by the DMD, the laser beam irradiated the target object, and the transmitted or reflected light was collected by a photodiode (single-pixel detector) and converted into electrical signals. Based on CS theory[247–249], the undersampled data (with a sampling ratio of only 10%–30% of the Nyquist frequency) was processed using the L1-norm minimization algorithm[69], successfully reconstructing an image with 128 pixel× 128 pixel.

Due to the lack of high-performance focal plane array detectors in the terahertz band, traditional imaging technologies face bottlenecks such as low resolution and complex systems. However, the "single pixel detector + computational reconstruction" characteristic of SPI perfectly

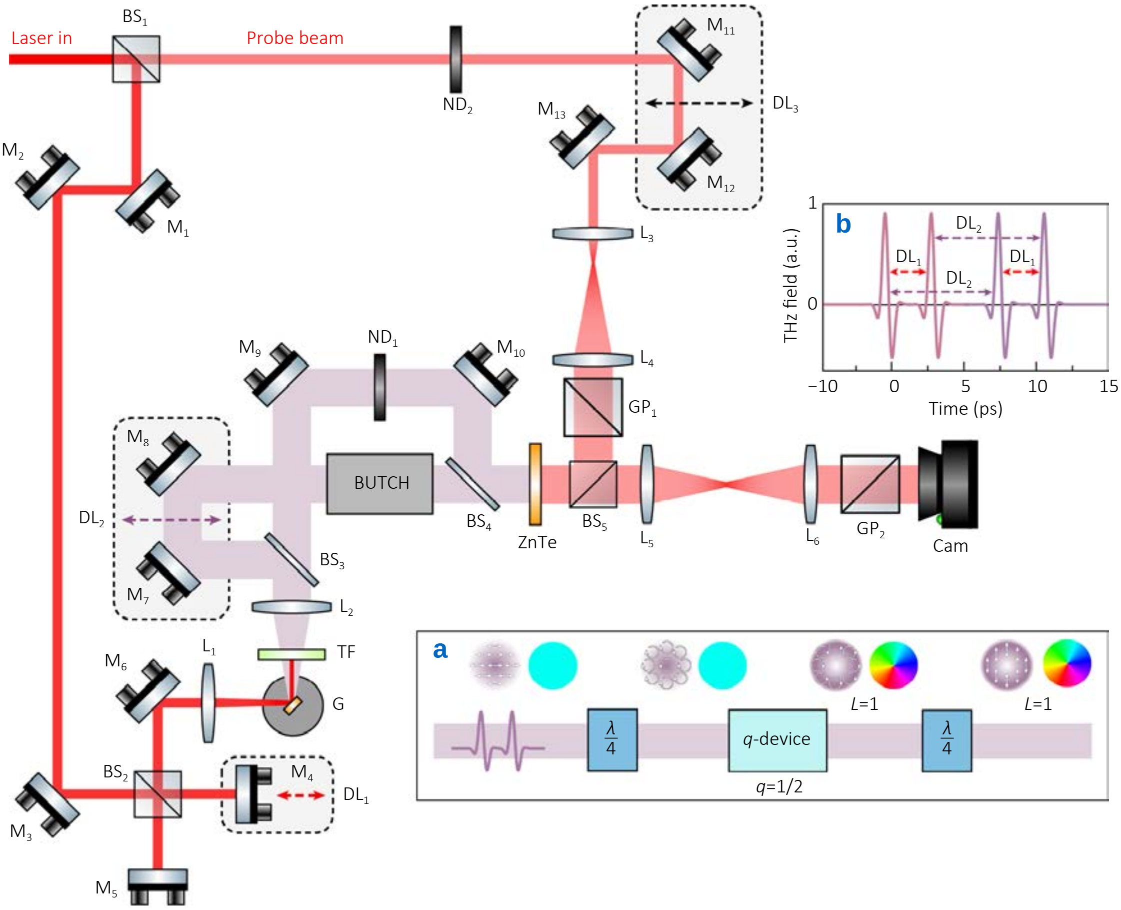

Fig. 40 | Schematic of the experimental setup for investigating the dynamics of interfering terahertz BUTCH beams[64]. Inset (a): elements of BUTCH beam generator[66,67]. Inset (b): temporal profiles of resulting terahertz pulses at the detecting ZnTe crystal.

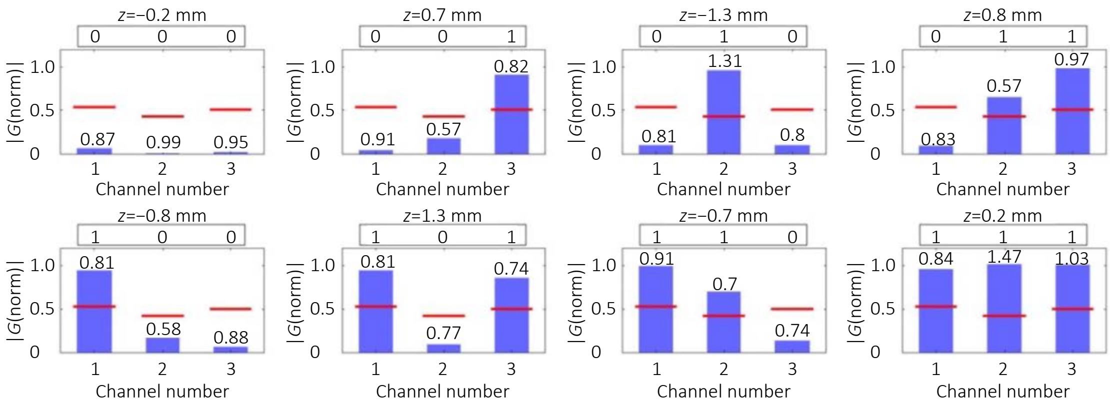

Fig. 41 | Implementation of binary encoding with interfering terahertz BUTCH beams across three spectral channels. Figure reproduced with permission from ref.[232], Optica Publishing Group.

forms a technical complementarity to this situation. In 2008, the team led by Chan WL achieved the first experimental verification of THz-SPI[250]. The experiment used random metal patterns fabricated on printed circuit boards (PCBs) as terahertz spatial modulators. Leveraging the strong reflective property of metal materials towards terahertz waves[251], it created a transmittance difference between the metal and non-metal regions in the patterns, thereby realizing spatial encoding of terahertz waves. The experimental system was composed of a terahertz transmitter, a modulation screen, an object mask, and a terahertz single-pixel receiver in Fig. 42(c). By replacing different modulation patterns and recording the detector's signals, the terahertz image of the target object as shown in Fig. 42(d) was finally reconstructed based on a correlation algorithm, exhibited in Fig. 42(e) and 42(f). This experiment verified, for the first time, the applicability of SPI in the terahertz band, marking the successful extension of SPI to the terahertz band.

5.2 Components of terahertz single-pixel imaging

From a structural perspective, the core optical path architecture of THz-SPI exhibits distinct modular characteristics. Its basic system consists of three key components: the terahertz illumination/detection unit, the target object, and the modulation unit, as seen in Fig. 43. As the core of the system for signal generation and acquisition, the illumination/detection unit undertakes the functions of generating terahertz radiation and converting terahertz signals carrying target information into measurable signals. Its performance directly determines the SNR, spectral range, and temporal resolution. This part outlines two technical approaches: the first is the continuous-wave terahertz (CW-THz) system[252,253], which employs a CW-THz source to produce stable monochromatic terahertz radiation, and works in conjunction with high-sensitivity pyroelectric detectors to enable direct measurement of terahertz wave intensity. Featuring a simple structure and low cost, this system is well-suited for static imaging scenarios where temporal resolution requirements are modest, such as non-destructive testing of cultural relics. However, its inability to resolve temporal details means it cannot capture the terahertz time-domain spectral information of a target, which limits its capability for material identification. The second approach is the THz-TDS imaging system[254], which generates pulsed terahertz waves based on photoconductive antennas or the

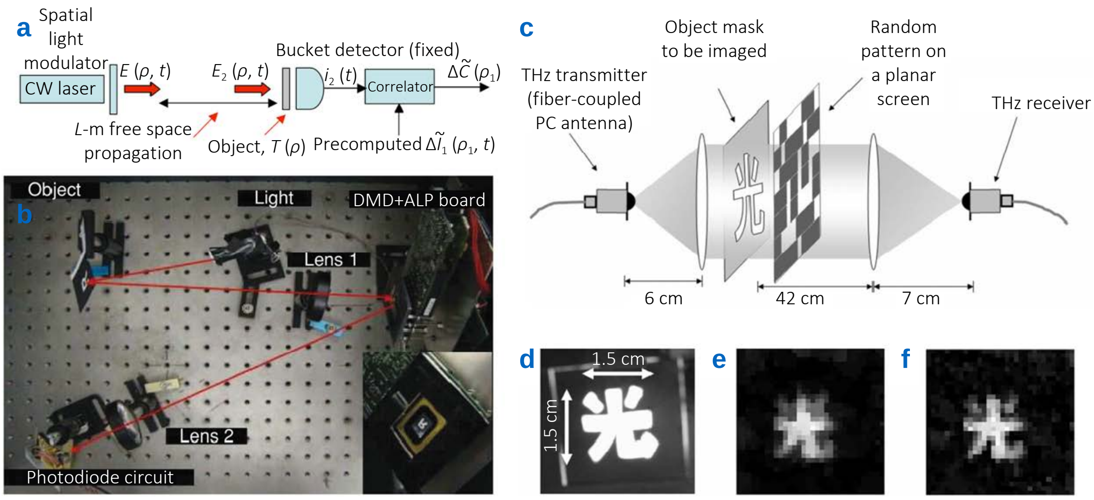

Fig. 42 | Development of terahertz single-pixel imaging. (a) Theoretical model of single-pixel imaging. (b) Schematic of the first implemented SPI experiment. (c) Demonstration of the first THz-SPI experiment. (d) Original image of the object. (e,f) Reconstructed images of the object after 300 and 600 acquisition times, respectively. Figure reproduced with permission from: (a) ref.[242], American Physical Society; (b) ref.[245], IEEE; (c–f) ref.[250], AIP Publishing.

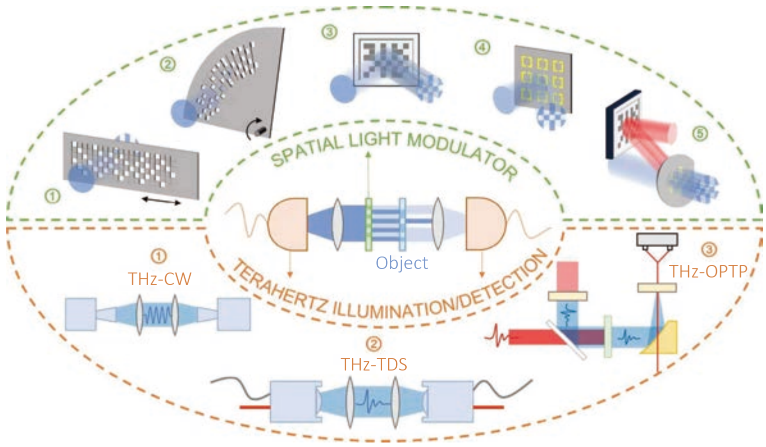

Fig. 43 | Basic architecture of THz-SPI, primarily categorized by two aspects: SLMs (upper section) and terahertz illumination/detection modes (lower section); the common types of SLMs (upper section, left to right) are: ① mechanical metal mask (strip type); ② mechanical metal mask (rotating disk type); ③ terahertz direct SLM; ④ metasurface modulator; ⑤ terahertz indirect optical modulator (e.g., optically pumped semiconductor materials). The terahertz illumination/detection modes (lower section, left to right) are: ① CW-THz source and detector; ② THz-TDS system; ③ optical pump-terahertz probe system.

optical rectification effect. It records the time-domain waveform of terahertz pulses through EO sampling or photoconductive detection, enabling simultaneous acquisition of the amplitude and phase information of the target, and obtains the spectral distribution through Fourier transform. Equipped with both temporal and spectral resolution capabilities, this system can identify materials (e.g., distinguishing between different chemical substances) by analyzing the terahertz spectral characteristics of the target. It delivers high imaging contrast, making it ideal for fields that demand spectral information—including biomedical imaging (e.g., early tumor diagnosis[255,256]) and hazardous material detection (e.g., spectral identification of explosives[257−259]).

As the imaging object, the target to be imaged encodes its own spatial distribution information (geometric structure and material properties[260,261]) into terahertz waves through the absorption, reflection, transmission, or scattering of terahertz waves. Since terahertz waves have unique sensitivity to polar molecules[262], semiconductor materials[263], etc., this technology can detect target details that are difficult to identify by traditional optical imaging, such as non-metallic items concealed within packages and lesion-affected regions in biological tissues.

The modulation unit is the encoding core of SPI technology. By implementing spatial modulation (including amplitude, phase, or polarization modulation) on terahertz waves, it converts the two-dimensional spatial information into time-series signals that can be recorded by a single-pixel detector. The design of modulation patterns and their switching speed directly affect imaging resolution and efficiency, and are key bottlenecks restricting the improvement of system performance. As a core innovative component of THz-SPI systems, beam modulators have shown an evolutionary trend from "static" to "reconfigurable" and from "mechanical" to "optical /electrical ", and are primarily categorized into two types: one is fixed mask modulators, which use prefabricated physical masks (e.g., 3D-printed diffusors[264,265], circuit boards printed with random metal patterns[250], microstructural arrays prepared by lithography) to perform spatial modulation on terahertz waves. They utilize the strong reflective property of metal regions and the transmissive property of non-metallic regions towards terahertz waves to form fixed two-dimensional modulation patterns. The other is reconfigurable modulators. To overcome the speed limitation of fixed masks, reconfigurable modulation materials has become a research focus, among which optically controlled mask modulation is the current mainstream solution. It takes advantage of the characteristic that the terahertz transmittance of photoactive materials (e.g., doped semiconductors, vanadium dioxide films[70,266]) changes with the intensity of pump light. A SLM projects a patterned pump laser to form a reconfigurable terahertz modulation mask on the material surface. The spatial distribution of the pump laser determines the terahertz wave mode, realizing high-speed "light-controlled light" modulation.

5.3 Development of mechanical modulation imaging

5.3.1 Metal masks

Early THz-SPI relied on mechanical masks to achieve beam modulation. The principle is to perform spatially blocking of terahertz through physical structures, thereby indirectly accomplishing encoding. Initial strip-shaped mechanical masks, limited by mechanical switching properties, suffered from inherently slow switching speed and failed to meet fast imaging needs. To overcome this limitation, Shen H et al. proposed a rotating disk modulation scheme[267]. As shown in Fig. 44, this scheme innovatively utilized the continuity of circular motion: after terahertz waves were collimated by a parabolic mirror, they passed through the sample and the patterns on the rotating disk, and finally, the detector received the intensity signals to reconstruct the image. Compared with the stepwise switching mode of traditional strip masks, the rotating disk eliminates the need for frequent starts and stops, increasing modulation efficiency by approximately 20 times. Nevertheless, limited by mechanical rotational inertia, its frame rate remains at a relatively low level (usually a few frames per second), and the pattern flexibility is poor. It is only suitable for applications in static or low-speed scenarios.

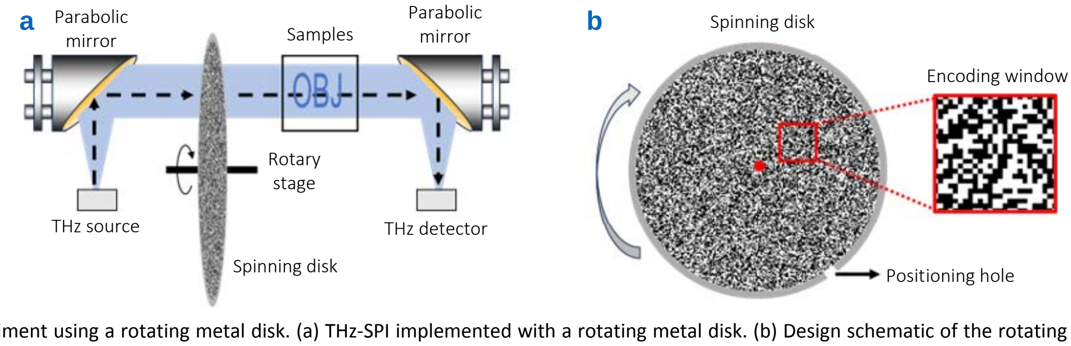

Fig. 44 | Experiment using a rotating metal disk. (a) THz-SPI implemented with a rotating metal disk. (b) Design schematic of the rotating disk: the red dot in the center is the rotation axis, and the positioning hole at the corner is used to calibrate the state of the rotating disk. Figure reproduced with permission from ref.[267], Optical Society of America.

Valles A et al. further optimized the rotating disk design[74]. They improved spatial encoding accuracy by designing high-precision periodic patterns (Fig. 45), and at the same time, adopted a broadband terahertz source to expand the spectral coverage range of imaging. This allowed the system to maintain stable imaging quality in the 3–13 THz frequency band, solving the limitation that early mechanical masks were only used for narrowband imaging.

In addition to the modulation of terahertz waves using such metal masks, there is another approach that employs specially fabricated terahertz modulators for patterned modulation. Unlike the method that uses mature visible-light SLM devices to modulate laser pump and then indirectly modulates terahertz waves via semiconductor materials, this approach modulates terahertz waves directly. Therefore, it is also classified into "mechanical" masks here. Most of the currently proposed terahertz direct modulators are electronically addressed devices; thus, compared with the aforementioned metal masks, they offer significantly enhanced flexibility.

5.3.2 Terahertz spatial light modulators

Watts CM et al. developed an all-solid-state THz-SPI system based on electronically controlled metamaterial SLM[71]; they constructed an 8 × 8 reconfigurable metamaterial array, where the electromagnetic absorption properties of each pixel are dynamically adjusted via a bias voltage, and integrated it with a single-pixel terahertz detector for imaging

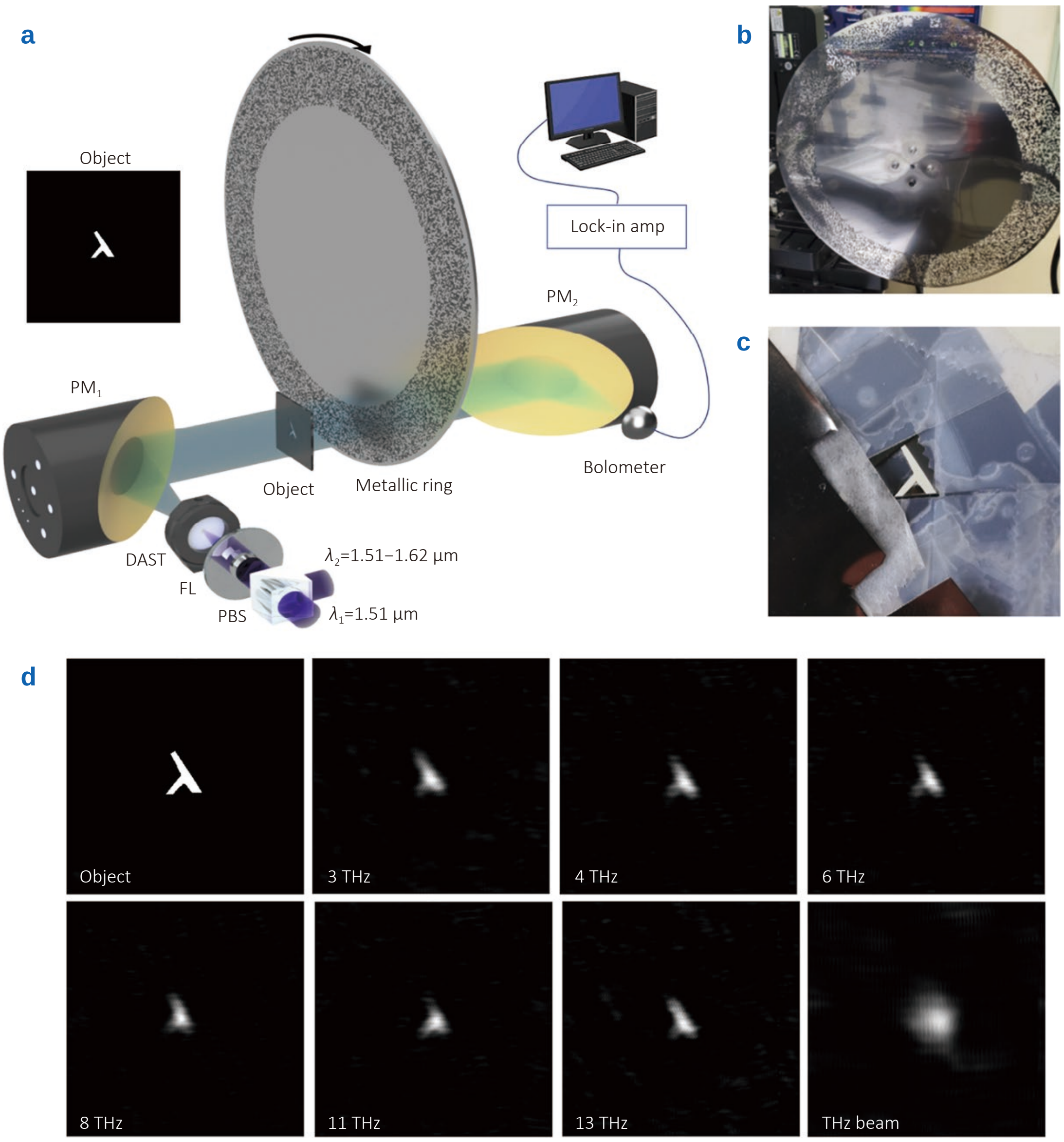

Fig. 45 | Further development of rotating disk. (a) Schematic of the imaging setup. (b) Photograph of the designed metal rotating disk. (c) Photograph of the object used for imaging. (d) Experimental results showing the broadband high-resolution imaging within the high-frequency terahertz region. Figure reproduced with permission from ref.[74], under a Creative Commons Attribution License.

(Fig. 46). The modulator's all-electronic control eliminates artifacts from mechanical rotation in traditional masks, while a lock-in detection scheme enables direct use of [1, −1] or [1, 0, −1]mask values, avoiding the doubled acquisition time and increased noise of indirect negative-value approximation methods. Additionally, combining compressed sensing with partial Hadamard matrices[268] reduces the number of measurements by over 70% (from 64 to 19) while maintaining image quality, increasing the frame rate to approximately 1 Hz and enabling real-time imaging of moving objects (1.8 mm/s lateral movement).

Compared with single-frequency terahertz SLMs, Li WL et al. developed an 8 × 8 dual-color terahertz SLM based on tunable liquid crystal (LC) metamaterial absorbers[76], as shown in Fig. 47. They utilized the large terahertz birefringence of LC, where a 0–10 V bias drives a ~20 GHz frequency shift of the absorber (from f_1=470.2 GHz to f_2=450.7 GHz) with a modulation depth exceeding 70% at both frequencies, enabling dual-frequency spatial encoding. They also proposed an auto-calibrated CS algorithm to mitigate the effects of non-uniform terahertz beams and pixel modulation, increasing the peak signal-to-noise ratio of images of dispersive objects by 52%.

Beyond the aforementioned metamaterial and LC modulators, Malevich Y et al. developed a 16 × 16 terahertz SLM based on electrolyte-gated graphene[73]; they utilized the electric double layer at the graphene-electrolyte interface to achieve high charge density via electrostatic gating (Fig. 48), and broke the trade-off between gating efficiency and switching speed by optimizing ion packing dynamics, enabling a maximum switching frequency of 1 kHz. The modulator realizes over 70% broadband terahertz modulation (covering 0.1–4 THz) and is integrated with a single-pixel detector to form an imaging system, reconstructing clear images of large-area objects.

Metal masks offer advantages such as a simple optical path structure, low cost, and no need for complex optical or electronic control systems. However, their flexibility in encoding images is limited. In contrast, devices like direct terahertz SLMs have a simple structure and can form relatively fine patterns through electronic control methods. Nevertheless, they suffer from limited resolution: fabricating high-resolution devices is not only difficult but also costly. These drawbacks have prompted researchers to shift toward developing optically controlled modulators. The core of optically controlled modulators lies in utilizing the photoinduced electron properties of specific materials to achieve dynamic regulation of terahertz waves, a process that deeply relies on the photoelectric effect within the materials.

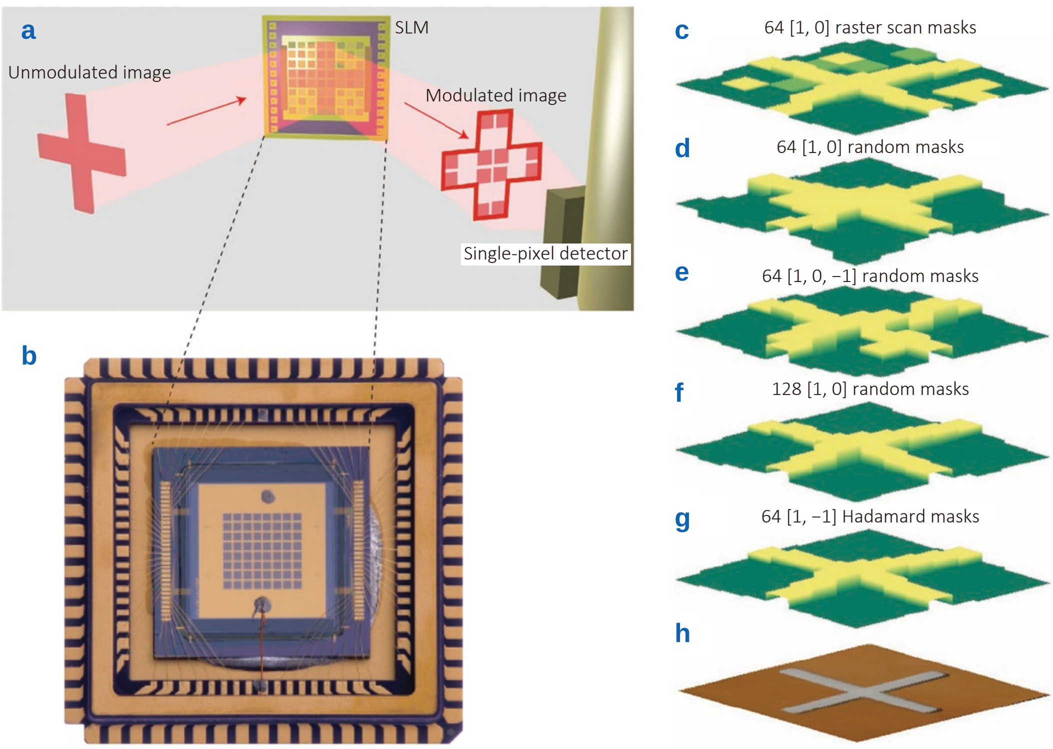

Fig. 46 | Single-pixel imaging with a THz-SLM. (a) Schematic of the SPI process using an SLM. (b) Photograph of the SLM. (c–g) Comparison of reconstruction techniques for an inverse cross aperture: (c) 64 [1, 0] raster-scan masks; (d) 64 [1, 0] random masks; (e) 64 [1, 0, −1] random masks derived from subtracting two sets of data; (f) 128 [1, 0] random masks and (g) 64 [1, −1] Hadamard masks. (h) Photograph of the object (inverse cross). Figure reproduced with permission from ref.[71], Springer Nature.

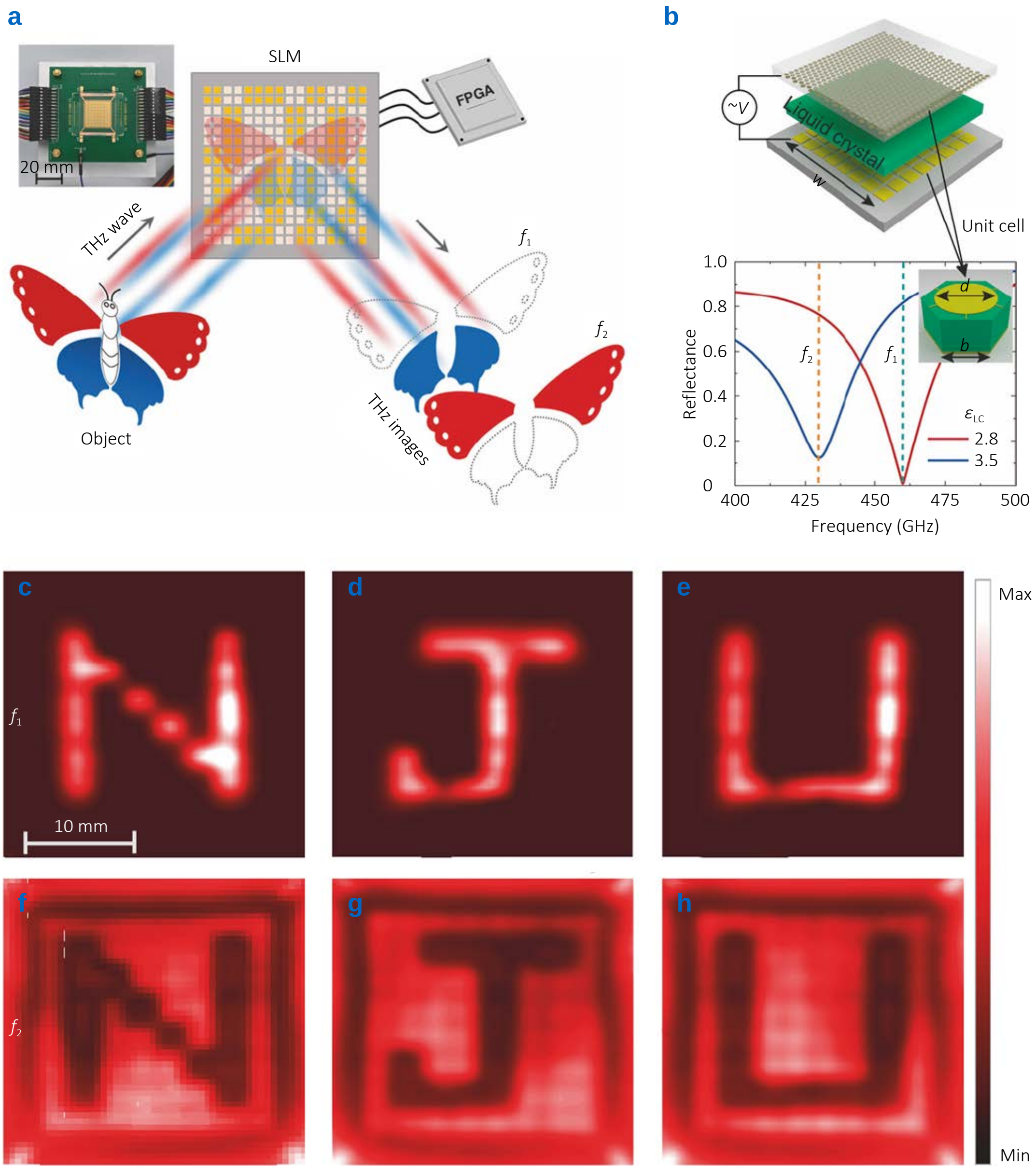

Fig. 47 | Dual-color terahertz SLM. (a) Schematic diagram of the dual-color terahertz SLM; the inset shows a photo of the fabricated terahertz SLM. (b) Exploded view of the terahertz SLM and simulated reflectance spectra for different permittivities of LC. (c–e) Projection display results at f_1. (f–h) Projection display results at f_2. Figure reproduced with permission from ref.[76], under a Creative Commons Attribution License.

5.4 Development of optical modulation imaging

5.4.1 Improvement of imaging speed

Taking typical materials such as high-resistivity silicon[269], germanium[270,271], and vanadium dioxide (VO_2)[272] as examples: in the dark state, these materials show high resistivity (valence band electrons bound to atomic orbitals), allowing terahertz waves to penetrate easily (transmittance usually over 50%); when irradiated by near-infrared or visible light pump, the materials absorb photon energy and trigger the photoelectric effect: valence band electrons jump to the conduction band to form massive free carriers, where for semiconductors like high-resistivity silicon and germanium, photoexcited carrier concentration can rapidly rise to 10^{16}–10^{17} cm^{-3} within several picoseconds, sharply increasing conductivity (from 10^{-4} S/m in the dark to 10^{-1}–10 S/m) and producing a metal-like electromagnetic response (free electrons induce a strong surface plasmon effect, leading to terahertz absorption or reflection with a modulation depth over 70%), while for phase-change materials like VO_2, photoexcitation not only boosts carrier concentration but also drives a phase transition from monoclinic (insulating state) to rutile (metallic state), and this structural change further enhances terahertz reflectivity (modulation depth over 60%) with a picosecond-level phase transition response.

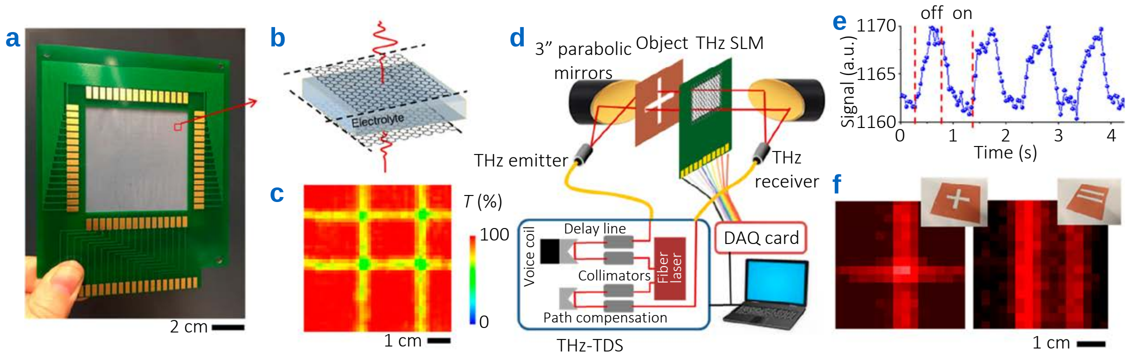

Fig. 48 | Terahertz SLM based on electrolyte-gated graphene. (a) Photograph of graphene-based terahertz SLM arrays on a PCB. (b) Schematic of one single pixel of the device. (c) Terahertz transmission image (0.1 THz) through the device. (d) Schematic of the experimental setup. (e) Integrated intensity variation when one SLM pixel is periodically switched. (f) Reconstructed images of cross and double-line masks; insets show metallic mask photographs. Figure reproduced with permission from ref.[73], American Chemical Society.

This photoelectric-effect-based modulation mechanism improves the response speed of optical control masks by 6–9 orders of magnitude compared to millisecond-level mechanical masks, and when combined with the sub-picosecond synchronous control of pump light and terahertz pulses via THz-TDS, it enables high-speed terahertz spatial encoding (providing key hardware support for fast imaging), with the upper limit of pattern switching frequency determined by the material's carrier lifetime (e.g., ~nanoseconds for silicon) or phase transition recovery time (e.g., ~microseconds for VO_2).

Enhancing imaging speed and achieving real-time imaging capability is a key to the practical application of THz-SPI, with the core lying in optimizing the efficiency between the modulation and reconstruction algorithm. Stantchev RI et al.[75] compared the total internal reflection (TIR), transmission, and reflection modes of high-resistivity silicon and found that the TIR mode could reach a modulation depth of 0.91 when the pump power increased. This performance outperforms the 0.77 of transmission mode and 0.57 of reflection mode, while the TIR mode also has insertion loss comparable to that of transmission mode. These advantages make it the preferred solution for high-speed imaging, as depicted in Fig. 49. Also, the team adopted a Hadamard matrix with partial sampling and a regularized imaging reconstruction matrix to reduce computation time, increasing the imaging frame rate for 32 pixel×32 pixel to 6 f/s and achieving terahertz video imaging for the first time; this enabled the observation of dynamic processes, a breakthrough compared to traditional static imaging.

To demonstrate the real-time dynamic imaging performance of this terahertz system, Stantchev RI's team[75] tracked hydration changes in *Achyranthes aspera*: the leaves were illuminated with an intense white-light source, whose excessive intensity induced high oxidative stress and chlorophyll loss (clearly observable post-experiment)[273]. Using terahertz transmission and phase delay images, the team recorded the leaf's photodamage process (Fig. 50): in the initial images, main leaf veins were clearly visible (white in transmission images, green in phase delay images), which corresponded to low transmittance and large phase delay. This is because veins are thicker than other leaf parts and responsible for water transport, so they increase terahertz absorption and phase delay in this region. As photodamage worsened, damaged areas showed gradually decreasing phase delay and increasing transmittance. This result comes from photooxidative stress-induced thinning of these regions, and thinner leaves further reduce terahertz phase delay while boosting transmittance. The team also found phase delay images offered clearer vein contrast, which indicates higher water content near veins with overall leaf thickness unchanged. Finally, imaging showed vein internal phase delay decreased over time, as the leaf became water-deficient and shrank. This research confirms THz-SPI enables real-time dynamic imaging of biological tissues.

Beyond the aforementioned technical routes, there are other improvement directions aimed at enhancing the imaging speed of THz-SPI. One category involves optimizing sampling efficiency through innovative signal measurement methods, while the other focuses on breaking the speed bottleneck by improving the performance of terahertz modulation materials.

In terms of innovative signal measurement methods, Zanotto L et al.[274] addressed the long acquisition time bottleneck of traditional THz-TDS SPI, which is caused by delay stage scanning sampling. They proposed a scanless terahertz waveform detection scheme: by cleverly utilizing the wavefront tilt effect, they implemented spatiotemporal encoding for terahertz detection, enabling instantaneous capture of terahertz waveforms, as seen in Fig. 51. This design eliminates the step of scanning sampling that relies on a delay stage in traditional time-domain measurement, further compressing the sampling process and forming a synergy with the spatial encoding strategy of SPI. The combination of SPI and single-shot detection[275] not only reduces system complexity but also breaks through the speed limitations of traditional raster imaging in both spatial and temporal dimensions, especially suitable for scenarios requiring rapid acquisition of material spectral-spatial information.

Regarding the improvement of terahertz modulation materials, Liang JX et al.[276] focused on the trade-off between

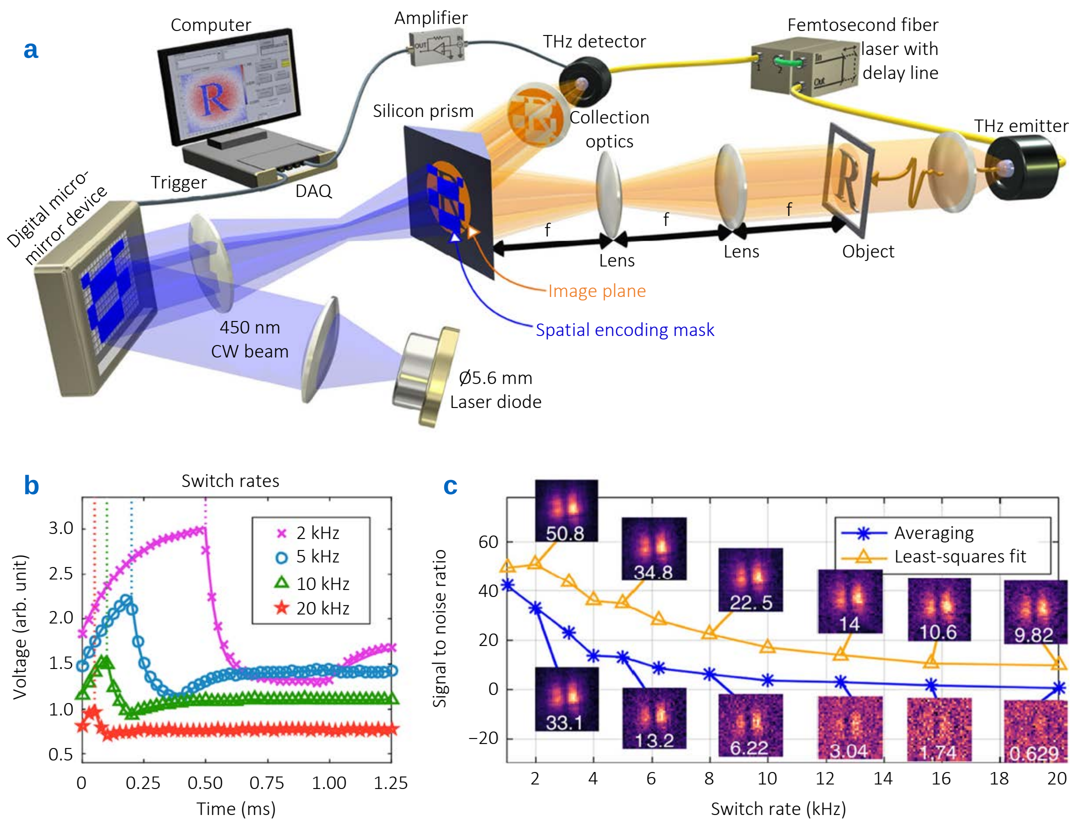

Fig. 49 | Real-time THz-SPI. (a) Schematic of the terahertz real-time SPI setup. (b) Voltage-time curves measured at different mask switch rates. (c) Curves showing the relationship between image SNR and mask switch rate. Figure reproduced with permission from ref.[75], under a Creative Commons Attribution License.

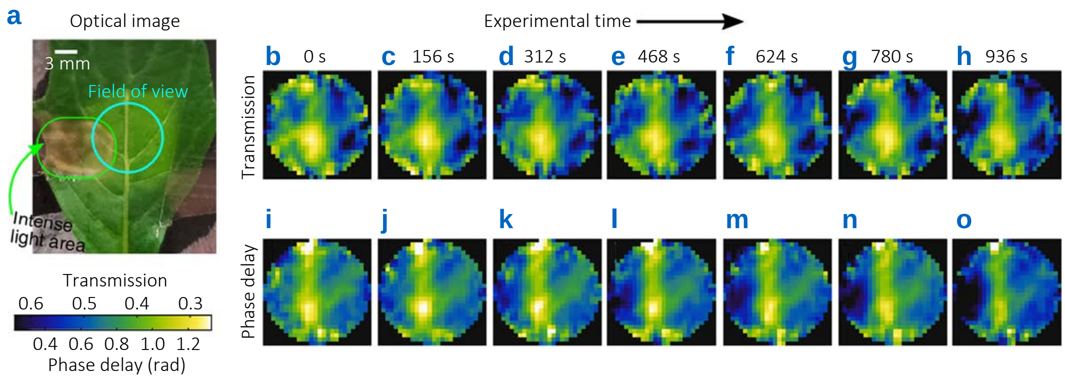

Fig. 50 | Real-time dynamic imaging using THz-SPI. (a) Optical image of the Achyranthes aspera leaf used in the experiment. (b–h) Terahertz transmission and (i–o) phase delay images of the leaf shown in (a) at different time points (the experimental time is labeled on top). Figure reproduced with permission from ref.[75], under a Creative Commons Attribution License.

modulation depth and rate in terahertz SLMs. They proposed using a polymer-silicon heterojunction as the core of the modulator, combined with CW optical illumination, to achieve high-performance THz-SPI, as shown in Fig. 52. Its core innovation lies in optimizing carrier dynamics through organic-semiconductor interface design: the polymer layer, serving as a light-absorbing unit, efficiently captures pump light energy, and the generated photogenerated carriers accumulate rapidly at the heterojunction interface; meanwhile, the thickness of the silicon substrate achieves performance balance by regulating the effective carrier lifetime. Based on this modulator, the study realized video-rate super-resolution SPI under a CW terahertz source.

5.4.2 Improvement of resolution

Limited by the diffraction resolution limit of the terahertz band, the far-field resolution of THz-SPI is on the order of the wavelength. To improve the resolution and meet the demand for smaller resolution, scanning with near-field probes[277–279] is an effective experimental method; however, raster scanning with near-field probes is often restricted by requirements for sample flatness and suffers from low SNR. The SPI scheme, which uses optical probes instead of physical ones, is a promising approach to achieve near-field detection.

In early near-field THz-SPI research, Stantchev RI et al. innovatively placed the sample in close to a high-resistivity silicon modulator[72], enabling terahertz waves to interact with the sample at sub-wavelength distances. By utilizing the information carried by evanescent fields, they achieved a

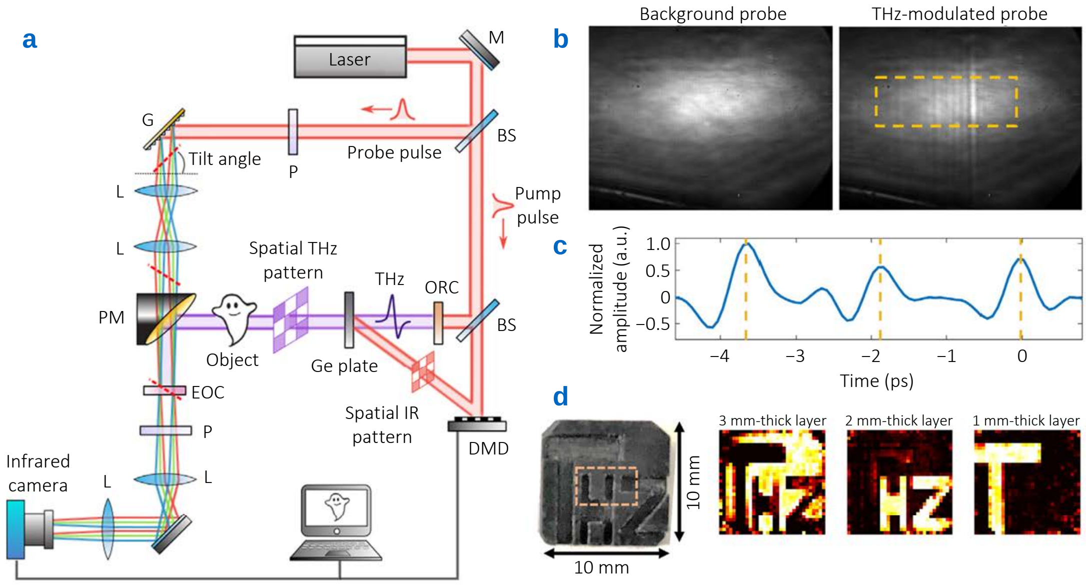

Fig. 51 | THz-SPI based on single-shot detection. (a) Simplified schematic of the THz-SPI optical path based on single-shot detection. (b) Example images recorded by an infrared (IR) camera. (c) Waveform showing an example of the measured terahertz trace. (d) A high-density polyethylene (HDPE) sample engraved with the letters "T-H-Z", along with the reconstructed images obtained based on the electric field amplitudes at three different peak-corresponding time positions selected from the terahertz waveform in (c). Figure reproduced with permission from ref.[274], under a Creative Commons Attribution-NonCommercial License.

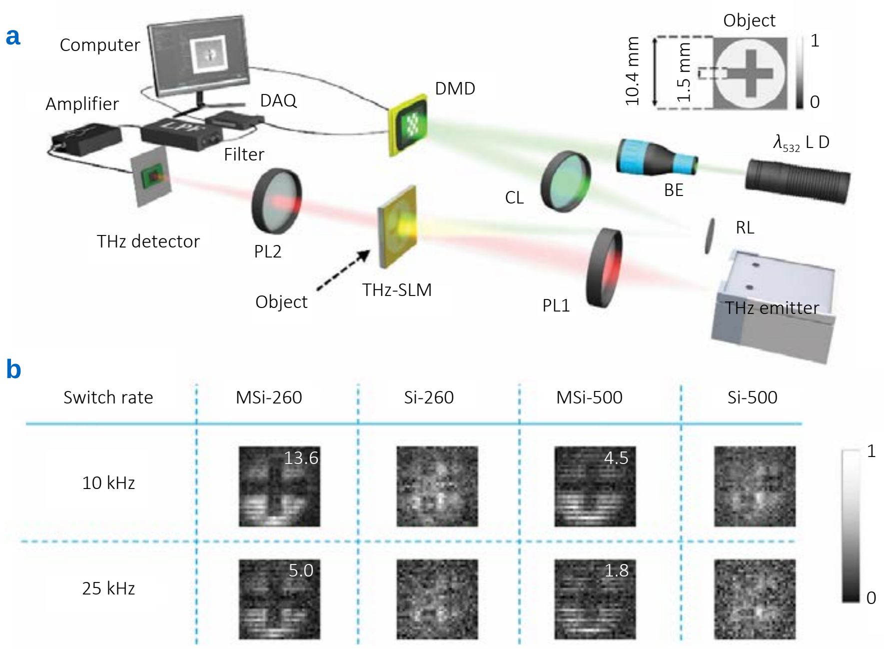

Fig. 52 | THz-SPI using a polymer-silicon heterojunction. (a) Schematic of the THz-SPI system. (b) Comparison of imaging quality among MSi-500, MSi-260, Si-500, and Si-260 at switching rates of 10 kHz and 25 kHz, respectively. Here, "M" denotes that a film of ploy [2-methoxy-5-(2'-ethylhexyloxy)-1,4-phenylenevinylene] (MEH-PPV), and the numbers following "Si" represent the thickness of the silicon wafers (micrometers). Figure reproduced with permission from ref.[276], John wiley and Sons.

resolution of 103 (±7) μm (Fig. 53) for the first time (smaller than the peak wavelength of 375 μm). The breakthrough of this work lies in proving that THz-SPI combined with the near-field effect can break the diffraction limit, providing ideas for subsequent high-resolution research. Later, the team further optimized the system: they used 6 μm ultrathin silicon wafers[280] instead of thick silicon wafers to further extract evanescent wave information, improving the resolution to approximately 9 μm (λ/45 at 0.75 THz), as shown in Fig. 53(c). Compared with their previous work, the ultra-thin silicon wafers reduced the propagation loss of terahertz waves in the material and extended the retention time of evanescent fields; however, the reduced thickness of the silicon wafers led to a roughly 20% decrease in terahertz modulation depth, revealing the trade-off relationship between resolution and signal intensity. Chen SC et al. used an 180 nm-thick VO_2 film as the modulator[281]; its ultrathin film property (only 3% of the thickness of silicon wafers) effectively retained evanescent wave information, and driven by femtosecond lasers, a resolution of 4.5 μm (exceeding λ/100) was achieved (Fig. 54): doubled compared to the 9 μm resolution. The innovation of this work lies in the selection of VO_2 material: its photo-induced maximum terahertz modulation depth can reach 60%, and the penetration depth of 800 nm laser is only 100 nm[282], avoiding interference from photoexcitation on the imaged object. Meanwhile, through the CS algorithm, high correlation was maintained during the acquisition process, providing stable data support for high-resolution imaging.

However, to achieve a large modulation depth, high laser energy is required to pump the terahertz modulation material, which imposes requirements on equipment performance. To reduce the demand for laser power, She RB et al. integrated single-layer graphene on a high-resistivity silicon (GOS) substrate[283], and its setup is detailed in Fig. 55(a). Utilizing the high carrier mobility of graphene, a higher modulation depth (improved by approximately 30%) was achieved under laser excitation compared to pure high-resistivity silicon substrates[284]. At the same time, they introduced the Fourier SPI method[285,286] through the video mode of a DMD, achieving a resolution of 270 μm at a central wavelength of 1.363 mm. Even when the sampling ratio was as low as 1.6%, the SNR still reached 5.11, which was better than the 3.89 of Hadamard SPI. In addition, Yang XY et al. integrated subwavelength metallic gratings on a silicon-on-sapphire (SOS) substrate (Fig. 55(e))[287]. They utilized the surface plasmon effect of metallic gratings to enhance the

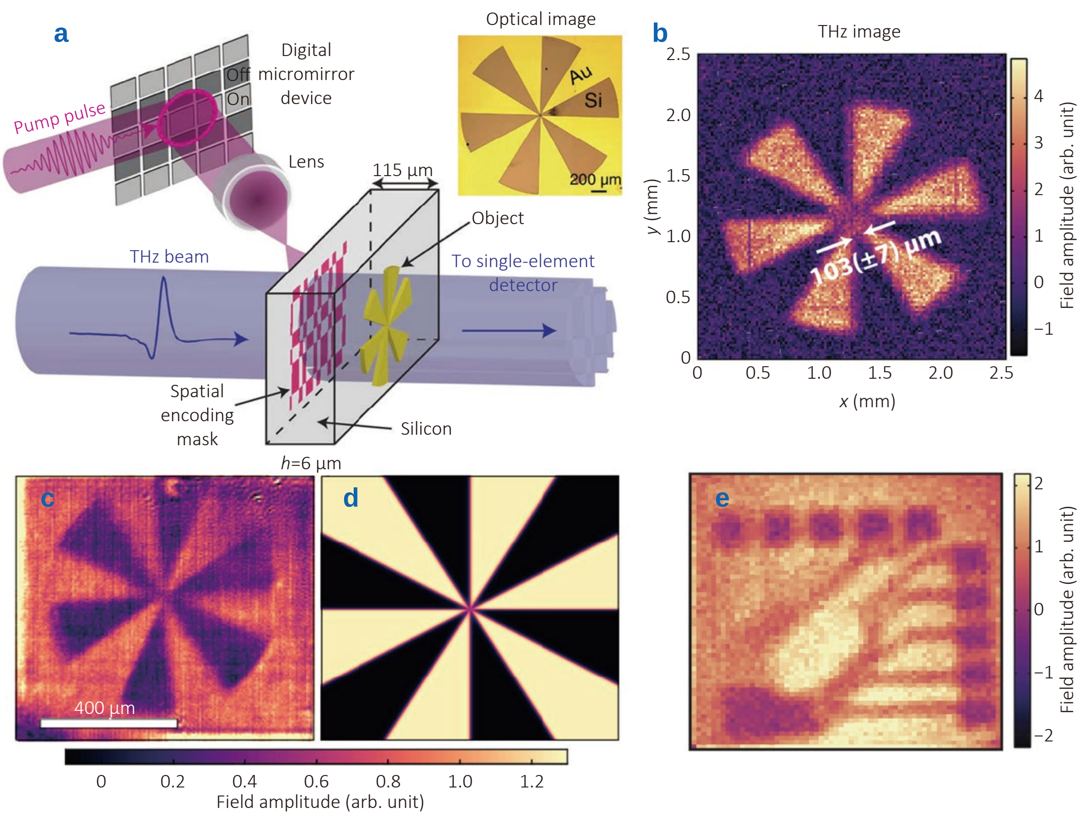

Fig. 53 | Near-field THz-SPI based on silicon. (a) Schematic illustration of near-field THz-SPI. (b) 128 pixel×128 pixel terahertz image of the resolution test target shown in (a). (c) Terahertz images of the cartwheel captured through a 6-μm-thick silicon wafer. (d) Calculated diffracted fields of the cartwheel. (e) Single-pixel terahertz image of the circuit board. Figure reproduced with permission from: (a, b) ref.[72], (c–e) ref.[280], under a Creative Commons Attribution License.

interaction between terahertz waves and materials[288,289]. Under a low pump energy density (80 μJ/cm^2), they achieved a modulation depth of over 60%, which is five times higher than that of pure SOS substrates (approximately 10%). This efficient modulation characteristic provides sufficient signal dynamic range for high-resolution imaging, helping to capture target details more accurately.

5.4.3 Limitation of modulation materials and other imaging methods

Based on the aforementioned experimental scheme, in the modulation of THz-SPI, materials such as Si and VO_2 are selected due to their broad operating bandwidth (0.1–3 THz). Semiconductor materials like silicon demonstrate an ultra-high modulation depth (>90%), rapid switching speed (~nanoseconds, GHz), and low required pump power (μJ/cm^2). However, they are limited by the penetration depth (~12 μm); with a reduced thickness resulting in a lower carrier concentration. This thus necessitates the incorporation of materials such as graphene to provide additional carriers for enhancing the modulation depth. In comparison to silicon, VO_2 features an extremely small penetration depth (~100 nm) and a relatively high modulation depth (>60%), which empowers it to achieve ultra-high resolution in near-field THz-SPI. Nevertheless, its slow switching speed (~milliseconds, kHz) and the need for relatively high pump power (mJ/cm^2) circumscribe its application scenarios.

To overcome the limitation imposed by material modulation depth, researchers consider abandoning the use of modulation materials and instead implementing encoding

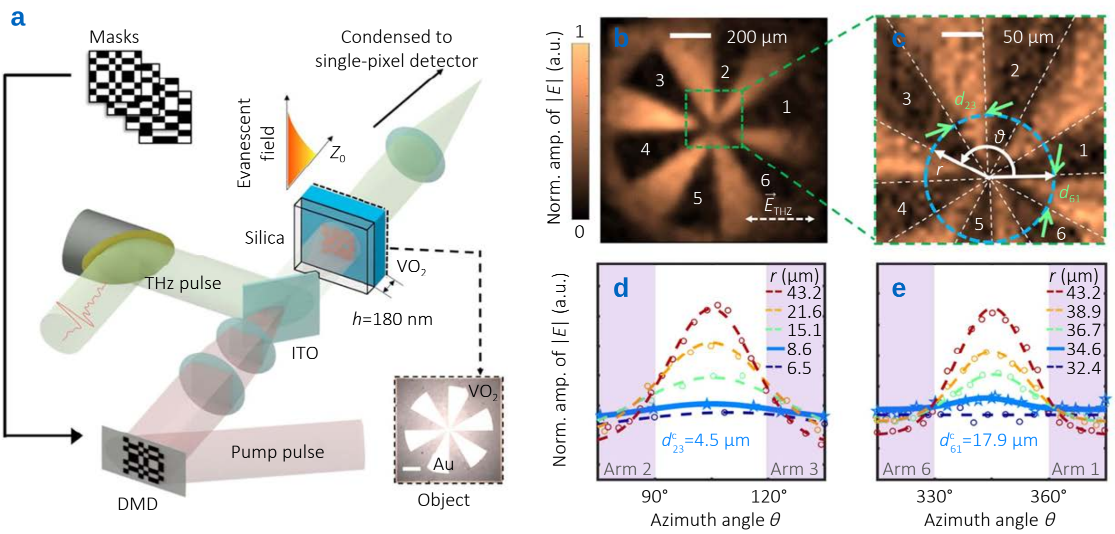

Fig. 54 | Near-field THz-SPI based on VO_2. (a) Near-field THz-SPI system based on a VO_2 terahertz modulator. (b) Experimental terahertz image of the cartwheel. (c) Higher-resolution terahertz image of the dashed green boxed area in (b). (d, e) Normalized terahertz amplitude as a function of arcs from arm 2 to arm 3 and from arm 6 to arm 1, respectively. Figure reproduced with permission from ref.[281], Optica Publishing Group.

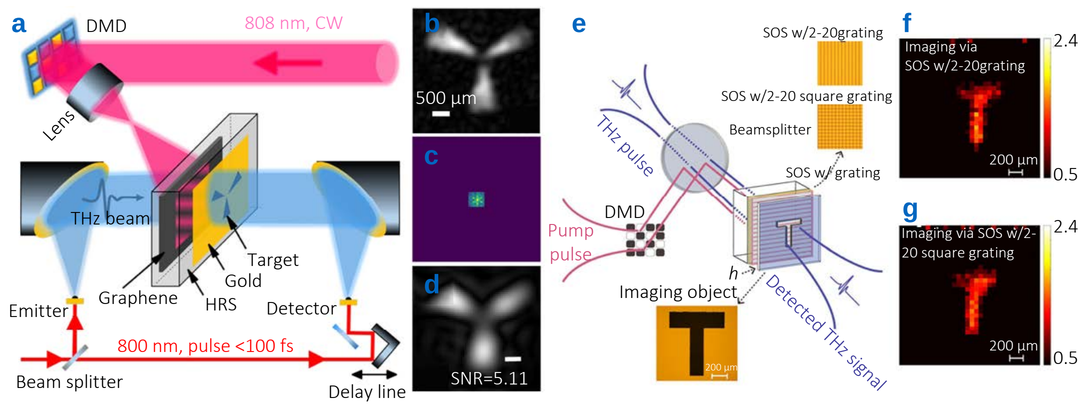

Fig. 55 | Low laser power pump THz-SPI systems. (a) Terahertz near-field SPI system based on GOS substrate. (b) Fourier SPI image at a sampling ratio of 11.8%. (c) Fourier spectrum and (d) corresponding image at a sampling ratio of 1.6%. (e) Terahertz near-field SPI system based on a metal grating structure on SOS, along with its corresponding reconstructed images: (f) image of the grating and (g) image of the square grating. Figure reproduced with permission from: (a–d) ref.[283], (e–g) ref.[287], AIP Publishing.

directly on the transmitter/detector to achieve THz-SPI. Olivieri L et al. directly encoded femtosecond pump light using a SLM[290–292], generating terahertz pulses with the same spatial pattern on a ZnTe crystal, is shown in Fig. 56. They advanced the generation of patterned beams to the terahertz generation stage, removing the modulator from the terahertz path and reducing loss. Combined with the principle of nonlinear SPI, this approach not only achieved hyperspectral imaging but also created favorable conditions for improving imaging resolution, further expanding the application dimensions of high-resolution imaging.

Chen SC et al. used spintronic terahertz emitters (STEs) instead of traditional EO crystals to further reduce the thickness of the transmitter, as shown in Fig. 57[293]; they generated terahertz pulses using the inverse spin Hall effect[294,295] and placed the object in close contact behind the modulator. The modulator's thickness of only a few nanometers avoided the blurring of encoded images caused by thick EO crystals, achieving a minimum resolution of 6.5 μm and covering a broad frequency band of 0.1–30 THz[296] (expanding the spectral range compared to electro-optic crystals (which usually cover 0.1–5 THz)). Meanwhile, its generation efficiency is comparable to that of electro-optic crystals, providing a new scheme for broadband high-resolution imaging.

As depicted in Fig. 58, Zhao JP et al. proposed the probe-beam encoding technology[297], they performed encoding in the detection stage, utilizing the spatiotemporal overlap characteristic between the terahertz field and probe light in EO sampling. By encoding the probe beam to selectively

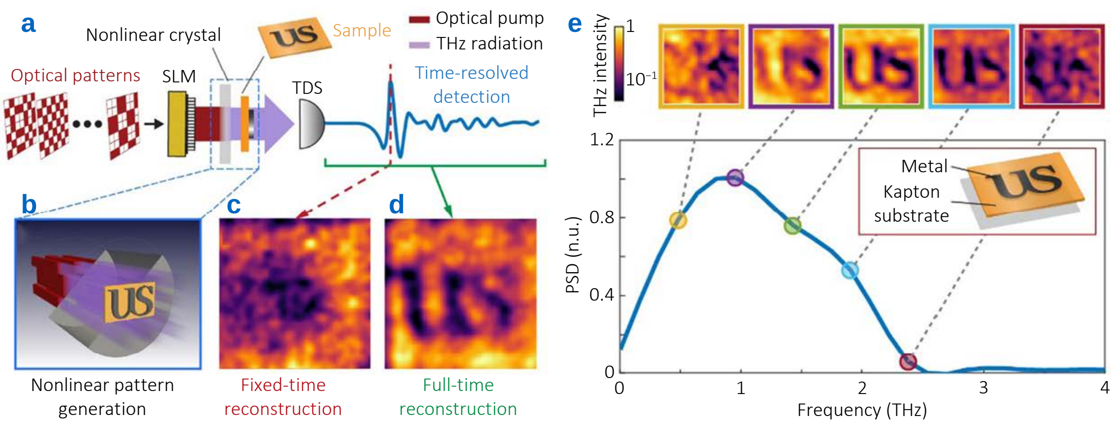

Fig. 56 | Time-resolved nonlinear ghost imaging. (a) Description of key experimental components for time-resolved nonlinear SPI. (b) Three-dimensional representation of terahertz mode nonlinear generation. (c) Fixed-time reconstruction. (d) Backpropagated hyperspectral image. (e) Reconstructed images at different frequencies of the hyperspectral image. Figure reproduced with permission from ref.[290], under a Creative Commons Attribution License.

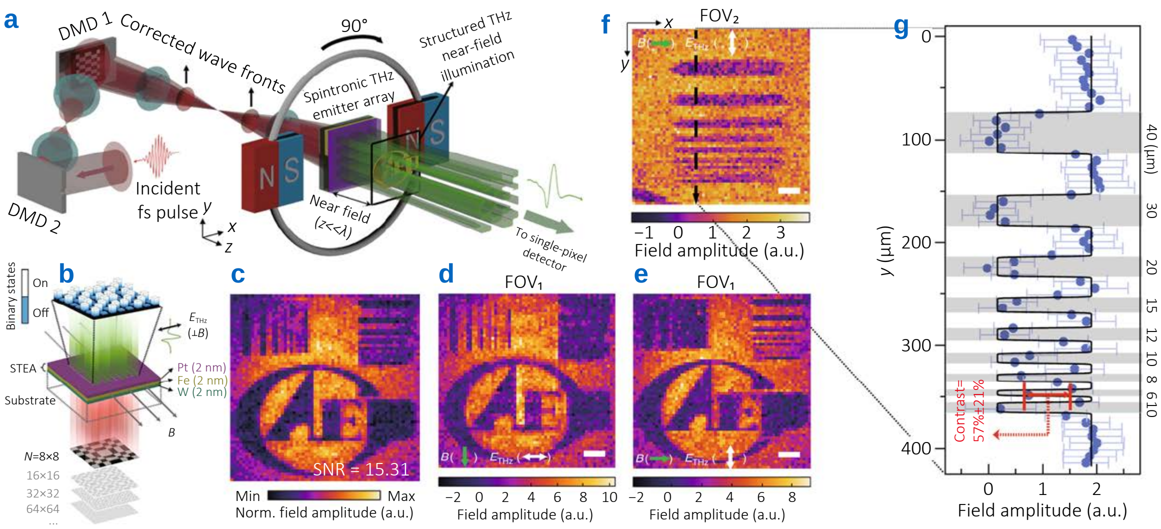

Fig. 57 | Ghost spintronic terahertz emitter array microscope. (a) Schematic of the ghost spintronic terahertz emitter-array microscope system. (b) Schematic of the STE array. (c) Fused polarization-free terahertz image. (d, e) Terahertz ghost images with a magnetic field applied along the vertical direction and horizontal direction, respectively. (f) Terahertz ghost image in a smaller field. (g) Averaged amplitude of the terahertz field along the black dashed arrow in (f). Figure reproduced with permission from ref.[293], under a Creative Commons Attribution License.

measure the target field, no dedicated terahertz modulators are needed. This method is not only simpler than directly modulating the terahertz field but also effectively retains the spatial information of the terahertz field. A resolution of 62 μm (λ/15) was achieved at 0.32 THz, providing a new technical path for high-resolution imaging.

5.5 Spectral identification imaging and time-of-flight imaging

Beyond the aforementioned functionalities, due to the distinct absorption characteristics of different substances for broadband terahertz waves, THz-SPI based on a THz-TDS system enables spectral identification imaging of materials. Shen YC et al.[298] analyzed a composite material made of polyethylene (PE) and lactose (Fig. 59(a–e)). Since the regions containing lactose exhibit two main absorption lines at 0.54 THz and 1.38 THz, the component regions of PE and lactose can be identified and distinguished by decomposing the time-domain spectral information of different coordinate regions. Olivieri L et al.[290] also adopted a similar approach, combining encoded terahertz generation and time-resolved measurement methods to achieve the classification and identification of gold, Kapton, and Teflon (Fig. 59(f–i)).

In addition, when terahertz pulses pass through a material, the difference in refractive index between the material and air causes varying degrees of peak shift in the terahertz time-domain pulses. The traditional raster scanning method requires time-resolved measurements of different regions of the material to calculate the material's thickness. In contrast, by encoding different regions of the object via THz-SPI, the superposition of time-domain waveforms of the material in the terahertz-transmitted regions can be obtained. Zanotto L et al.[274] used samples made of high-density PE with different thicknesses and successfully reconstructed 16×16 3D images at different time delays; Chen SC et al.[293] also utilized their self-developed SPI system to achieve 3D imaging of SiO_2 with different thicknesses and specific patterns, as shown in Fig. 60. At the same time, combined with CS technology, high-resolution phase detection capability can also be achieved using a small number of measurements.

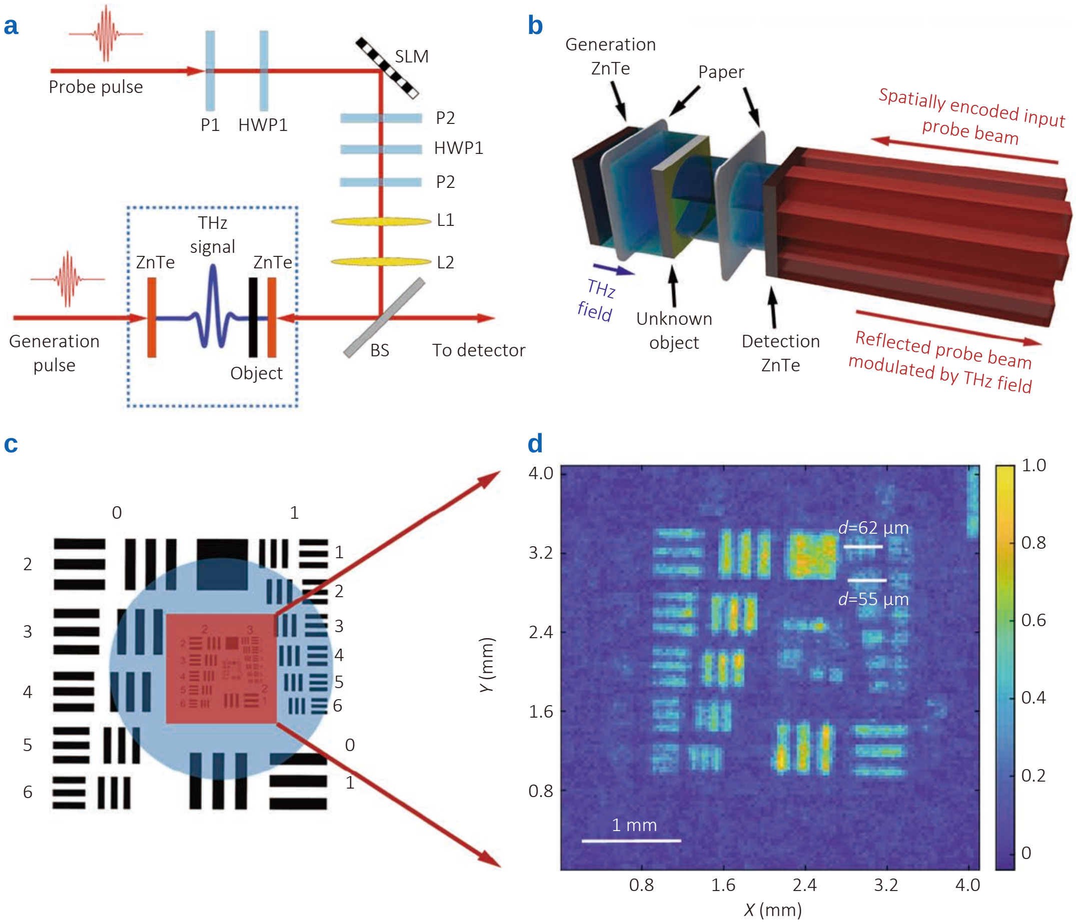

Fig. 58 | THz-SPI via probe-beam encoding. (a) Schematic of the system configuration. (b) Detailed description of the sampling approach. (c) Original American National Standards Institute resolution target (AF target). (d) Experimental result with a 128 pixel×128 pixel resolution, showing the resolution limit. Figure reproduced with permission from ref.[297], under a Creative Commons Attribution License.

5.6 Future development of terahertz single-pixel imaging

Currently, THz-SPI technology mostly adopts easily modifiable optical modulators, enabling flexible imaging methods that are continuously improved. It has formed typical applications in fields such as real-time dynamic imaging, near-field imaging, spectral imaging, and time-of-flight imaging, and is one of the most promising technologies for achieving fast and even real-time imaging in the terahertz frequency

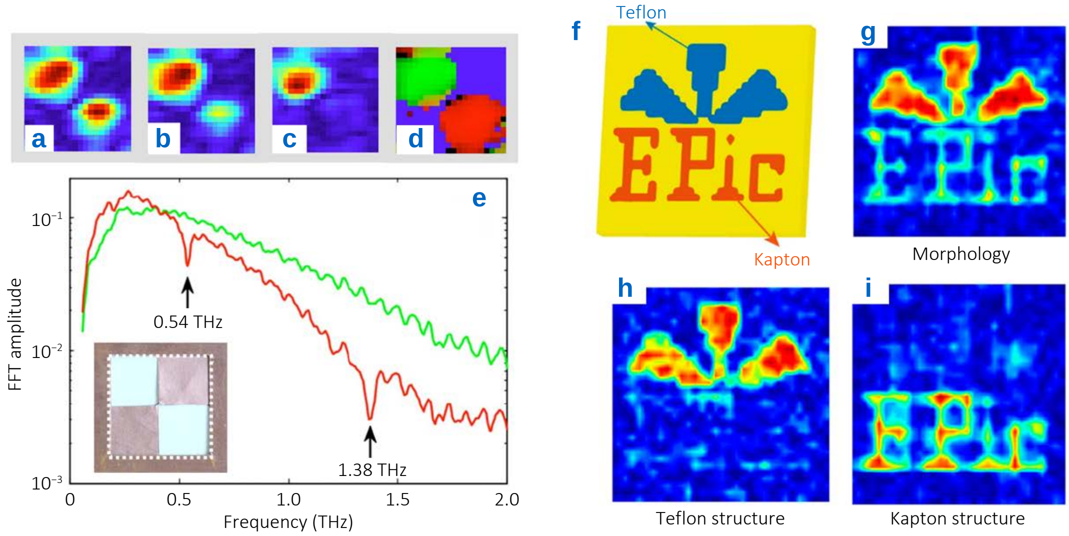

Fig. 59 | Spectral identification imaging. (a–c) Reconstructed terahertz images of the sample at 0.50 THz, 0.54 THz, and 1.38 THz, respectively. (d) RGB chemical map of the sample. (e) Terahertz spectra of polyethylene and lactose. The hyperspectral imaging based on time-resolved measurements: (f) the object; (g–i) reconstructed images, used to demonstrate the chemical selectivity of the hyperspectral method. Figure reproduced with permission from: (a–e) ref.[298], AIP Publishing; (f–i) ref.[290], under a Creative Commons Attribution License.

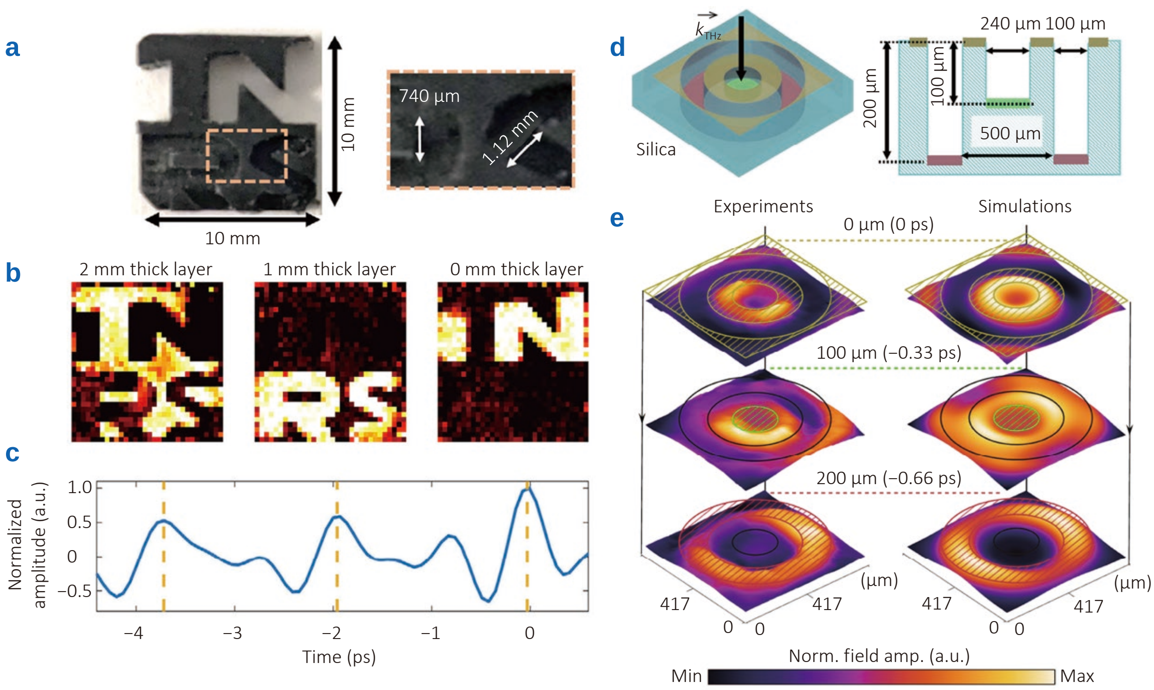

Fig. 60 | Time-of-Flight imaging. (a) Sample: a high-density PE sheet engraved with the letters "I-N-R-S". (b) Images reconstructed using the electric field amplitudes at three different peak points of the terahertz waveform shown in (c). (c) Terahertz waveform. (d) Structure of the object: the object has air grooves engraved on a SiO_2 substrate, with three interfaces. (e) Experimental sub-diffraction-limit images of the interfaces at heights of 0 μm, 100 μm, and 200 μm, respectively, along with the simulated electric field distributions corresponding to these three interfaces. Figure reproduced with permission from: (a-c) ref.[274], under a Creative Commons Attribution-NonCommercial License; (d, e) ref.[293], under a Creative Commons Attribution License.

band, with significant advantages in cost, speed, and efficiency. However, the technology still faces several key limitations at present.

A lack of direct, efficient terahertz modulators persists: existing static devices (e.g., mechanical masks) suffer from slow switching speeds and fixed encoding sequences, while dynamic devices (e.g., photomodulated materials) require high-power lasers for modulation. Both types are constrained by material inherent properties and light source limitations. Thus, low-cost devices with large modulation depth and high switching rates are urgently needed to simplify system function implementation.

Insufficient fast full-waveform acquisition technology remains: most current systems only measure the peak intensity of terahertz waves, which is a trade-off to boost acquisition speed at the cost of full information, while full-waveform measurement is significantly time-consuming. Though improvements can be achieved via mechanical methods[299,300] (replacing stepping delay lines with oscillating/rotating delay lines) or optical methods[301,302] (wavefront transformation), further optimization is still required.

The advancement of new imaging algorithms is needed: the selection of sampling matrices[303−305] and compressed sensing reconstruction[306] are core components of the technology. Although deep learning-based image enhancement algorithms[307−311] have been initially applied, it is still necessary to develop advanced algorithms based on imaging principles to achieve lower sampling ratios, which will help the technology move toward real-time imaging.

Looking ahead, the advancement of THz-SPI technology will focus on addressing its current key limitations through targeted innovations. As these challenges are tackled, THz-SPI is expected to expand into more high-value applications, ranging from chemical spectroscopy to on-site non-destructive testing, which will solidify its role in unlocking the practical potential of the terahertz band.

6 Terahertz near field imaging

Terahertz technology has emerged as a powerful tool across diverse fields, yet conventional far-field terahertz imaging remains fundamentally constrained by the Rayleigh diffraction limit. Its lateral resolution is limited to roughly half the wavelength-on the order of hundreds of micrometres, making it unsuitable for applications that demand micron- to nanometre-scale detail. In biomedical research, for example, single-cell imaging requires nanometre resolution, and probing terahertz responses of proteins, DNA, and viruses demands still finer discrimination. In the same way, the fast progress of micro- and nanomaterials in materials science needs detailed study of how electromagnetic forces interact with matter to understand the causes of many large-scale effects.

Driven by the demand for sub-wavelength spatial resolution, terahertz super-resolution imaging has attracted extensive attentions[312−315]. Confocal and compressive-sensing approaches, despite still using far-field detection[316−317], achieve only modest gains, which are typically limited to approximately ~$\lambda/10$. By contrast, evanescent-wave-based near-field techniques deliver markedly higher resolving power. These methods draw inspiration from mature infrared and visible-light near-field systems, which now routinely spatially map plasmonic, phonon-polariton, and excitonic resonances[318−325], probe strong coupling phenomena[326,327] and enable micro- to nano-scale material characterization[328−333] (Fig. 61). The unique ability of the terahertz band to penetrate materials and select specific wavelengths makes near-field terahertz imaging a promising tool for studying biological tissues and understanding how electromagnetic waves interact with matter at the nanoscale in advanced materials.

6.1 Principal near-field imaging schemes

To resolve the terahertz near-field distribution on a sample's surface and surpass the Rayleigh limit by orders of magnitude, three principal near-field imaging schemes have been developed over the past decades: aperture-based, photoconductive-probe, and scattering-type techniques. The first two modalities require the detector to be positioned within the evanescent field region immediately above the surface, whereas the scattering-type approach uses a sharp probe to scatter the local field, converting evanescent waves into propagating waves that can be detected at a distance. Each method has its pros and cons: aperture and photoconductive probes usually only provide resolution at the micrometre level, while scattering-type systems can achieve resolution in the tens of nanometres but can disturb the original surface field, requiring complex algorithms to fix the data. Thus, the optimal choice of near-field detection strategy depends critically on the specific application requirements.

6.1.1 Aperture-based terahertz near-field imaging

An aperture-type terahertz near-field imaging system typically employs a sub-wavelength aperture—fabricated as a tens-of-micrometres-wide hole in a metal film—with a detector placed directly against the aperture. When a terahertz wave is incident upon and transmits through the sample, only the evanescent fields in the immediate vicinity of the aperture reach the detector. Because the separation between the aperture (and detector) and the sample surface is much smaller than the wavelength, the measured signal predominantly encodes the sample's near-field distribution. Synge EH first proposed this seminal approach in 1928[334].

The main part of using an aperture-type terahertz near-field system is to carefully control the space between the metal plate, which has a tiny hole, and the surface of the sample. In theory, the smaller this spacing, the stronger the near-field signal; in practice, one must keep the gap on the order of tens of micrometres to avoid contact or collision and to ensure experimental stability. The method's chief

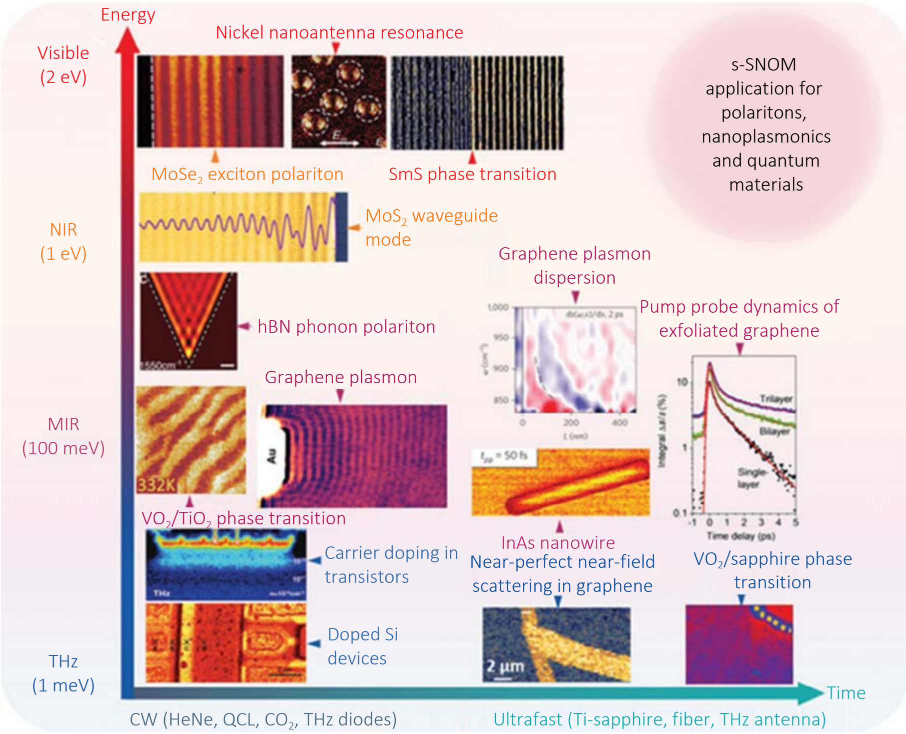

Fig. 61 | Summary of selected application scenarios for scattering-type near-field imaging systems in nanophotonics, spanning the visible, infrared, and terahertz spectral bands. Figure reproduced with permission from ref.[333], John Wiley and Sons.

advantage is its simplicity: by raster-scanning the sample beneath a fixed aperture, one can directly record terahertz near-field contrasts with a spatial resolution set by the aperture diameter (tens of micrometres). However, it also has notable drawbacks. The tiny aperture transmits only a weak fraction of the incident terahertz power, yielding low signal-to-noise ratios that demand low-noise, high-gain amplification. Diffraction from the aperture edges and surrounding regions further degrades resolution and can introduce background artifacts. Moreover, any variations in the sample's surface topography can alter the plate-sample separation during scanning, causing fluctuations in the detected near-field intensity and thus compromising image quality. In recent years, research on aperture-type terahertz near-field systems has been limited—largely focused on mapping surface-resonant fields in individual metallic resonator elements[335–340].

6.1.2 Photoconductive-probe terahertz near-field imaging

Photoconductive-probe terahertz near-field systems likewise position the detector within the evanescent region to directly sample the surface field, but unlike aperture-type setups, the photoconductive switch itself can be fabricated at subwavelength dimensions, obviating the need for a separate aperture. Figure 62 shows two representative probe geometries. geometries, because the active switch is sensitive only along its biased axis, the left-hand configuration selectively detects the transverse field component, whereas the right-hand probe is oriented to measure the longitudinal field.

Fig. 62 | Schematic illustrations of two representative photoconductive probes.

In practical implementations, the photoconductive-probe tip must be positioned just a few to a few tens of micrometres above the sample surface. Owing to the micron-scale dimensions of the photoconductive switch and the elimination of aperture-diffraction effects, these systems can achieve lateral resolutions on the order of a few micrometres. Nevertheless, they face notable challenges. First, the absence of an intrinsic tip–sample spacing feedback mechanism—and the extreme fragility of the photoconductive tip—means even slight collisions can render the probe inoperative. Consequently, real-time monitoring of the tip height via optical microscopy, often augmented with image-recognition algorithms for active position adjustment, is essential. Second, optical alignment is particularly demanding: a femtosecond laser (typically 780 nm or 1560 nm) must be precisely focused onto the tiny switch, with alignment accuracy directly governing system performance. Despite these hurdles, photoconductive-probe terahertz near-field microscopy has advanced rapidly recently, thanks to its ability to selectively detect specific field-polarization components and to record time-domain near-field signals, finding growing application in biomedical diagnostics and in the electromagnetic control of metasurfaces[210, 341–345].

6.1.3 Scattering-type terahertz scanning near-field imaging

Scattering-type terahertz scanning near-field optical microscopy (s-SNOM) departs fundamentally from aperture- and photoconductive-probe schemes by employing an indirect scattering mechanism: evanescent waves at the sample surface are converted into propagating waves via a sharp probe and detected in the far field, as shown in Fig. 63. In practice, terahertz s-SNOM integrates a conventional far-field terahertz optical path with a scanning probe microscope (SPM)—typically an atomic force microscope (AFM) or a tuning-fork-based probe—to raster the near-field sensor across the sample and achieve nanoscale mapping of surface field distributions.

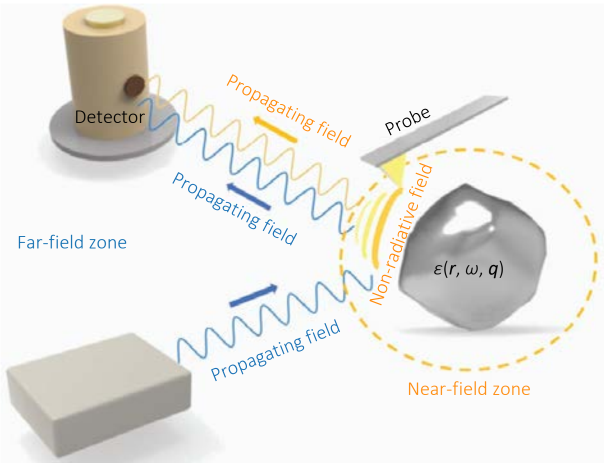

Fig. 63 | Schematic illustration of the operational principle of a terahertz scattering-type scanning near-field optical microscope (THz s-SNOM). Figure reproduced with permission from ref.[333], John Wiley and Sons.

When the terahertz beam is tightly focused onto the probe apex, the probe becomes polarized, and-by the "lightning-rod" effect-a highly confined local field is established at the tip. As the tip approaches the sample surface, image charges are induced within the sample to mirror the probe's excitation charges, forming an effective dipole between tip and sample that radiates electromagnetic waves into the far field. This mechanism converts the localized near-field into a propagating wave, with an efficiency set by the effective polarizability of the tip-sample dipole. Achieving true nanometre-scale resolution therefore requires a tip curvature radius on the same order; however, owing to the long wavelength of terahertz radiation, the dipole's polarizability remains relatively low. To overcome this, the probe is operated in tapping mode so that the scattered signal is modulated at the probe's oscillation frequency. By demodulating the detected signal at higher harmonics, one can selectively recover the terahertz near-field information from the sample surface. Later sections provide detailed discussions of the signal-modulation and demodulation schemes, as well as the optical-path design.

This system offers several key advantages. First, its spatial resolution is governed by the tip's curvature radius rather than the incident wavelength, enabling true nanometre-scale imaging. Second, by leveraging mature AFM feedback control, the tip–sample distance can be precisely maintained, improving stability and image quality. Third, the integration of either single-frequency continuous-wave sources or broadband pulsed sources allows both high-resolution near-field imaging and terahertz near-field time-domain spectroscopy.

Nevertheless, the use of a scattering probe inevitably perturbs the native evanescent field, necessitating sophisticated near-field models to reconstruct the unperturbed distribution. Additionally, compared to aperture and photoconductive probe systems, terahertz s-SNOM is more complicated and costly, and the probe's lower scattering efficiency can affect its performance on samples that reflect light poorly. The remainder of this review focuses on this technique, exploring its diverse application scenarios.

Recently, numerous research groups worldwide have independently developed terahertz s-SNOM systems and extended their applications across materials science[82, 346–350], biological imaging[351], and nanotomography[77, 352–353]. Notably, leading advances have come from Rainer's team at CIC nanoGUNE (Spain), Haewook's group in Korea, Basov's laboratory in the USA, Mengkui Liu's team, and Huber's group. Leveraging terahertz s-SNOM, these teams have conducted in-depth studies of metamaterials, two-dimensional electronic systems, photonic crystals, and biological tissues, thereby laying a solid foundation for the future development of terahertz near-field imaging.

By contrast, development of terahertz scattering-type near-field techniques in China began somewhat later. The earliest home-grown system was demonstrated in 2018 by Cui HL's group at Jilin University, who achieved continuous-wave terahertz near-field imaging at 110 GHz[79, 354]. Subsequently, Shanghai University of Electricity and Technology, the Shanghai Institute of Microsystems and Information Technology, and the USTC have each constructed their own terahertz s-SNOM platforms. To broaden the technique's applicability, these domestic efforts have integrated various terahertz sources—electronics-based emitters operating in the hundreds-of-GHz band, quantum-cascade lasers above 2 THz, and pulsed sources covering 0.2–3 THz.

6.2 Applications of terahertz scattering-type near field imaging

After more than a decade of rapid advancement, terahertz scattering-type SNOM has been applied across a broad spectrum of fields, opening up diverse application scenarios. These include nanoscale materials characterization[347–356], mapping of surface-field distributions in resonant architectures[78, 357–359], probing of surface-plasmon standing waves[360–363], biomedical imaging[351, 364–367], and near-field tomographic reconstruction[77, 352–353].

To exploit the direct correlation between the near-field signal and the local dielectric properties beneath the probe, Moon K et al. employed a custom-built THz-TDS–based near-field imaging system to perform both imaging and spectroscopy of α-lactose[80] in 2019. The experimental optical layout is shown in Fig. 64. In Fig. 64, the sample's topography and first-harmonic near-field image are presented: trace α-lactose crystals embedded within a HDPE matrix produce markedly stronger near-field contrast, reflecting lactose's higher dielectric constant in the terahertz band. Finally, the authors recorded near-field spectra of lactose (A) and HDPE (B) (Fig. 64(c)) and applied a probe-sample line-dipole model to extract the dielectric constant of lactose.

In 2020, Chen C et al. employed a gas-laser–based terahertz scattering-type near-field imaging system to compare the near-field intensity and phase of two phase-change materials—amorphous $Ge_1Sb_2Te_4$ (a-GST) and crystalline $Ge_1Sb_2Te_4$ (c-GST)—at multiple frequencies, as shown in Fig. 65[81]. Owing to a phonon resonance in c-GST near 4 THz, its dielectric constant undergoes a pronounced variation around that frequency, whereas a-GST's dielectric response changes more gradually. This difference manifests as a contrast reversal at ~4.25 THz in both the near-field intensity and phase images.

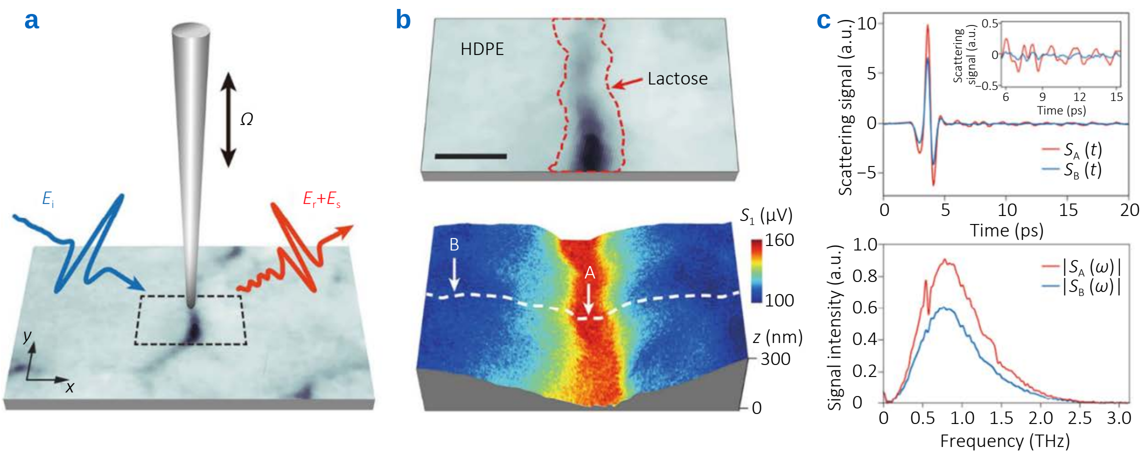

Fig. 64 | THz-TDS s-SNOM near-field imaging and spectroscopy of α-lactose. (a) Schematic of the THz s-SNOM experimental setup, (b) optical and near-field topography images of lactose embedded in HDPE, and (c) time-domain scattering signals and corresponding THz resonance spectra. Figure reproduced with permission from ref.[80], under a Creative Commons Attribution License.

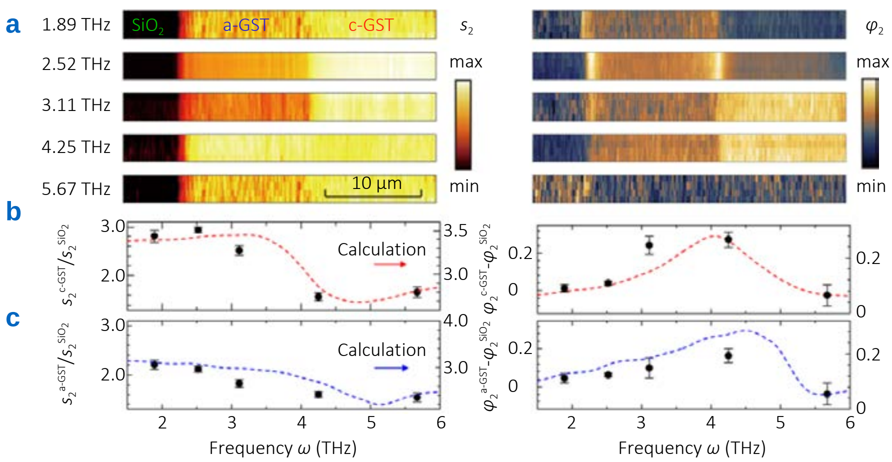

Fig. 65 | Comparison of near-field amplitude and phase for two phase-change materials at different terahertz frequencies. (a) Near-field amplitude (s_2) and phase (ϕ_2) images of substrate/a-GST/c-GST areas across multiple frequencies. (b, c) Measured and calculated near-field spectra extracted from the images in (a).Figure reproduced with permission from ref.[81], under a Creative Commons Attribution-NonCommercial License.

The following year, Basov and colleagues in the USA employed a THz-TDS s-SNOM system to study thin-layer Weyl semimetal WTe_2[354]. As shown in Fig. 66, the setup Fig. 66(a) consists of the THz-TDS optical path combined with an AFM probe; panel Fig. 66(b) shows optical micrographs of monolayer, bilayer and trilayer WTe_2 on an hBN substrate; and panel Fig. 66(c) presents the corresponding first-harmonic, time-domain peak near-field images. They observed a clear layer-dependent insulator-to-metal transition: the monolayer's near-field signal is nearly identical to that of the hBN substrate, whereas in the trilayer a pronounced signal increase denotes emergent metallic behaviour. Importantly, this transition was shown to persist even at low temperatures.

In 2018, Rainer's team in Spain employed an electronic frequency-multiplier source to realize a 500–750 GHz terahertz s-SNOM system[368]. By combining this source with an AFM-based probe, they imaged a single static-memory cell, acquiring both topography and first-harmonic near-field amplitude and phase maps, as shown in Fig. 67. Two measurement points straddled the device's PN junction: point C in the n-doped region (carrier density 2×10^{17} cm^{-3}) and point D in the p-doped region (2×10^{16} cm^{-3}). These two sites exhibited markedly different near-field contrasts, directly reflecting their carrier concentrations. Furthermore, theoretical calculations of the dependence of near-field amplitude and phase on carrier density reproduced the experimental transition between points C and D with high fidelity, validating the system's quantitative sensitivity to semiconductor doping levels[368].

Scattering-type terahertz s-SNOM offers unique advantages for probing the surface resonance fields of sub-wavelength metallic structures. In 2017, Riccardo et al. implemented a QCL-driven s-SNOM system to map both the amplitude and phase of surface resonances in a metallic photonic crystal[78], as shown in Fig. 68. Dean's group used a similar QCL-based s-SNOM setup to image a sub-wavelength metallic ring resonator in 2021, extracting the real-part near-field signal to reveal opposite positive and negative electric field polarities on the ring's left and right sides[357], as shown in Fig. 69.

In 2024, the team at the UESTC introduced a time-domain-filtered terahertz scattering-type scanning near-field optical microscope (THz-TDF s-SNOM), in which an extended probe cantilever permits temporal separation and removal of probe-surface-wave interference, thereby isolating the sample's intrinsic terahertz nanospectral and imaging signals. They demonstrated its superiority in revealing deep sub-wavelength vibrational and resonant modes in historical pigments and metallic antennas[83, 356], as show in Fig. 70. In the same year, they further employed a conventional terahertz s-SNOM to achieve reversible nanoscale switching between Lorentzian and Fano resonance line shapes by rotating the resonant structure, thus elucidating a probe-induced phase-interference mechanism[369]. Additionally, by tuning the incident polarization angle, they realized tunable weak-strong coupling hybrid states at 0.75 THz and 0.91 THz in a metal microstrip–substrate-waveguide "photonic molecule", providing a new strategy for geometrical-angle control of light–matter interactions[370].

Surface plasmon-polaritons are a fundamental phenomenon in condensed-matter physics that, prior to the advent of near-field techniques, could only be inferred indirectly via far-field reflection or transmission. In 2017, Rainer et al. employed a graphene-hBN-Au multilayer heterostructure combined with a near-field photocurrent detection scheme to achieve real-space imaging of acoustic graphene plasmons[360], as shown in Fig. 71. Given that terahertz wavelengths are typically on the order of hundreds of micrometres, directly resolving the resulting standing-wave pattern demands both an extended imaging range and plasmons with very high confinement to overcome their intrinsic propagation losses. By using the dielectric environment of the multilayer stack to compress the plasmon wavelength by more than two orders of magnitude, the authors were able to observe multiple standing-wave fringes within a few micrometres of the surface.

In 2022, Chen S et al. at the University of Shanghai for Science and Technology used a terahertz-gas-laser-driven scattering-type s-SNOM to achieve real-space imaging of

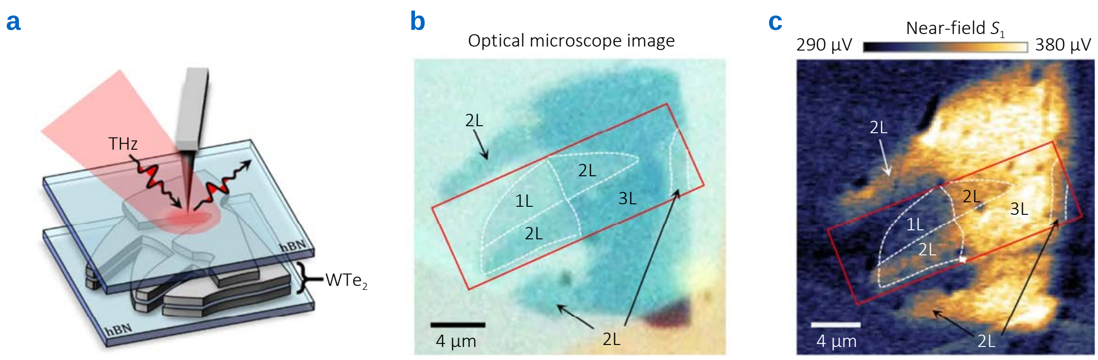

Fig. 66 | Near-field imaging of the Weyl semimetal WTe_2 using a THz-TDS s-SNOM system. (a) Schematic of the THz s-SNOM experiment on an hBN-encapsulated WTe_2 microcrystal, (b) corresponding optical microscope image, and (c) room-temperature THz near-field image revealing distinct layer-dependent signals across 1L, 2L, and 3L regions. Figure reproduced with permission from ref.[354], under a Creative Commons Attribution License.

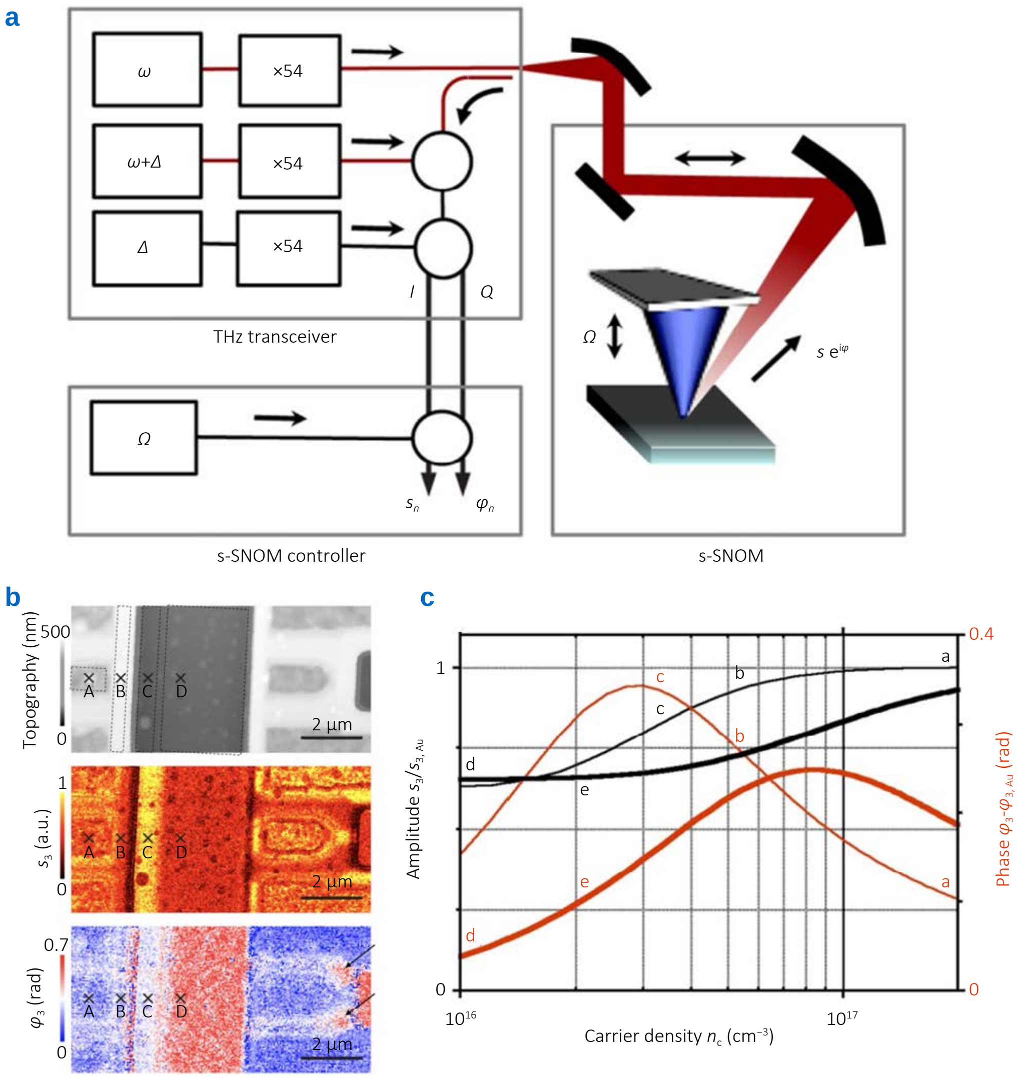

Fig. 67 | Terahertz near-field imaging of regions with different carrier concentrations. (a) Schematic of the tunable THz s-SNOM setup, (b) topography alongside 0.6 THz near-field amplitude and phase images of doped Si, and (c) predicted near-field signals as a function of carrier density. Figure reproduced with permission from ref.[368], under a Creative Commons Attribution License.

surface plasmon-polaritons on the topological insulator Bi_2Se_3[361], as shown in Fig. 72. Although only half a fringe was captured, tuning the incident terahertz frequency produced the expected shift in fringe spacing, in excellent agreement with theoretical predictions. The following year, the same platform was applied to map standing waves of acoustic plasmons in silver telluride (Ag_2Te)[362], as shown in Fig. 73. Thanks to an exceptionally high field-confinement factor, plasmons excited at 4.25 THz exhibited a measured wavelength of approximately 2.5 μm.

Near -field terahertz imaging has also made significant inroads into biomedical applications. In 2020, Wang HB et al. at the Chongqing Institute of Green and Intelligent Technology (CAS) employed a THz-TDS s-SNOM system to achieve nanoscale near-field mapping of individual immunoglobulin molecules, ingeniously using graphene substrates to combine high imaging contrast with an exceptionally flat background signal[351], as shown in Fig. 74. In 2024, Hu M's group at UESTC, in collaboration with Hu T's team at West China School of Stomatology, extended THz-TDS s-SNOM to visualize oral Streptococcus bacteria, establishing a clear correlation between cellular morphology and near-field response[364], as shown in Fig. 75. Later that year, the same teams applied nanoscale near-field imaging to bovine enamel before and after demineralization; by integrating AFM, SEM and elemental mapping, they uncovered the morphological and dielectric-constant changes driven by lattice dissolution and mineral-ion migration during early caries formation, offering fresh insights for early caries diagnosis and enamel electromagnetic characterization[366].

In 2025, a team from the UESTC and the Third Military Medical University implemented a single-bacterium terahertz dielectric nanoscopic imaging (STDN) strategy on a custom terahertz scattering-type SNOM platform[367], as shown in Fig. 76. By synchronously capturing AFM three-

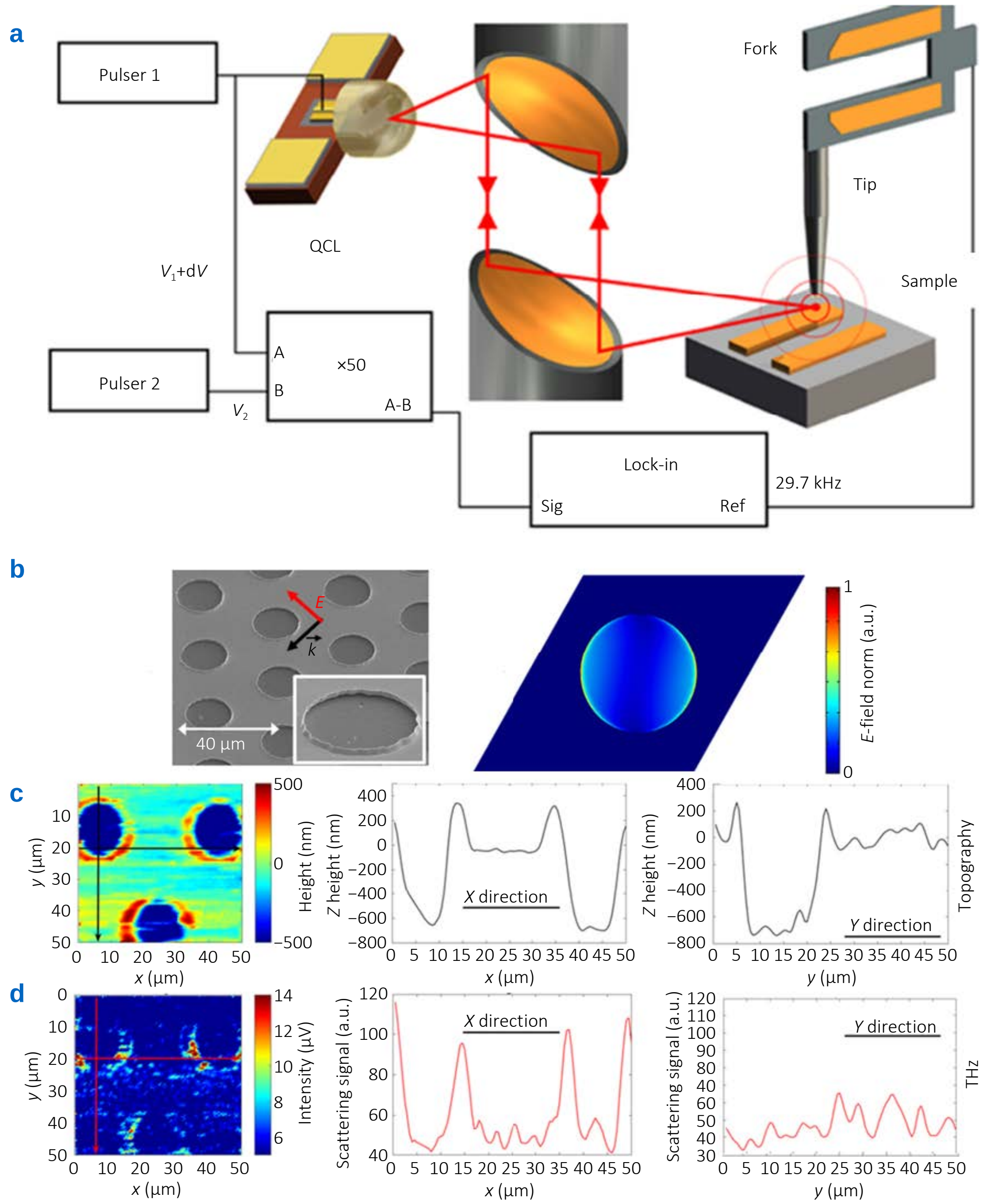

Fig. 68 | Observation of localized terahertz plasmonic modes on a metallic photonic crystal. (a) Schematic of the experimental setup, (b) SEM micrograph and simulated electric field of the patterned quantum cascade laser (QCL) surface, alongside (c) topography and (d) corresponding THz near-field scattered signal with extracted profiles. Figure reproduced with permission from ref.[78], American Chemical Society.

dimensional topography and terahertz near-field dielectric responses, and combining principal-component analysis with a support-vector-machine classifier, they demonstrated 99.3% accuracy in species identification and 91.6% accuracy in antibiotic-susceptibility testing within just two hours—paving the way for label-free, culture-free rapid single-cell microbial diagnostics.

By exploiting the intrinsic depth-sectioning capability of near-field microscopy, nanometre-scale tomographic reconstruction has become possible. In 2014, Rainer and co-workers demonstrated three-dimensional imaging of a protruding feature buried beneath a dielectric overlayer using an infrared s-SNOM platform[328]. That same year, Moon et al. extended this concept to the terahertz band, achieving nanometre-resolution imaging of a metal grating under a dielectric coating with their THz-s-SNOM system—attaining ~80 nm resolution at the third-harmonic frequency[77], as shown in Fig. 77. More recently, in 2023, Wang HB's team at the Chongqing Institute of Green and Intelligent Technology applied THz-TDS s-SNOM for tomographic mapping of protein films on solid substrates. By incorporating a finite-dipole probe-sample model, they developed a novel

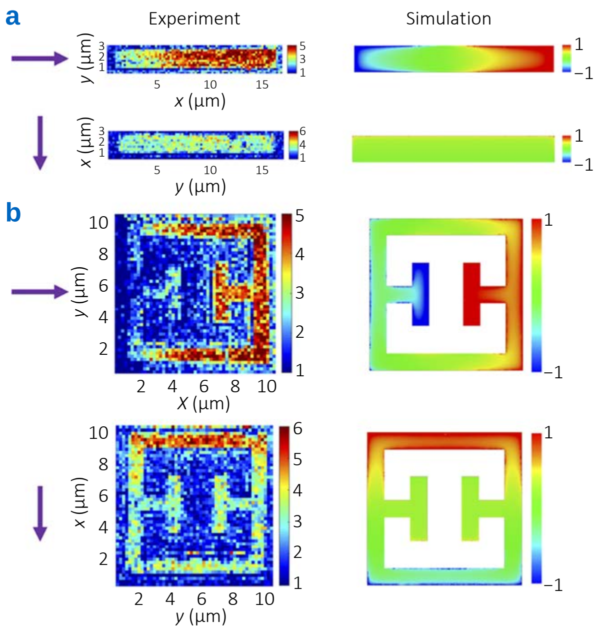

Fig. 69 | Terahertz near-field imaging of a rectangular antenna and ring resonator. Measured THz s-SNOM images and corresponding out-of-plane field simulations of (a) a dipole antenna and (b) a split-ring resonator (SRR) at ~ 3.45 THz, under both on- and off-resonance excitation. Figure reproduced with permission from ref.[357], under a Creative Commons Attribution License.

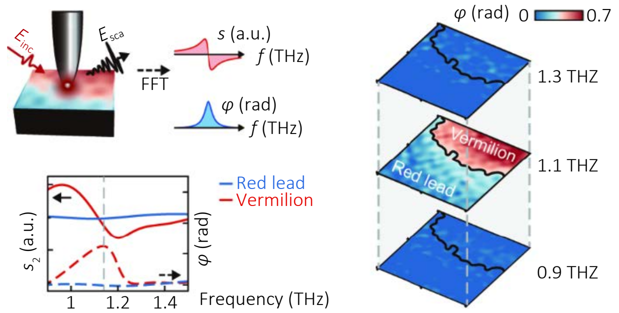

Fig. 70 | Time-domain-filtered THz scattering-type s-SNOM revealing intrinsic nanoscale light-matter interactions. Figure reproduced with permission from ref.[83], American Chemical Society.

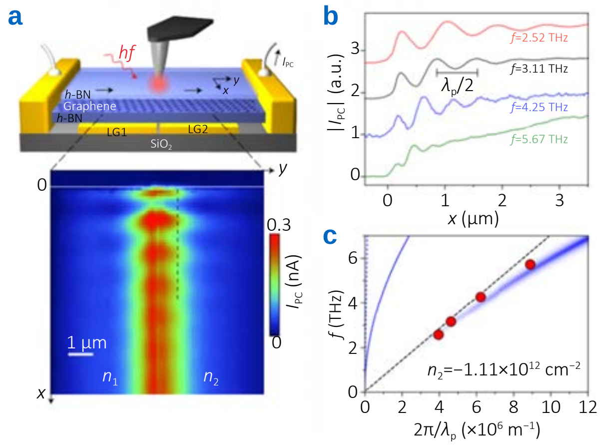

Fig. 71 | Real-space imaging of graphene acoustic surface plasmon-polaritons. (a) Schematic of the THz photocurrent nanoscopy setup alongside the near-field photocurrent image of a split-gate graphene photodetector. (b) Near-field photocurrent profiles at various frequencies and (c) the corresponding experimental and theoretical plasmon dispersion relations. Figure reproduced with permission from ref.[360], Springer Nature.

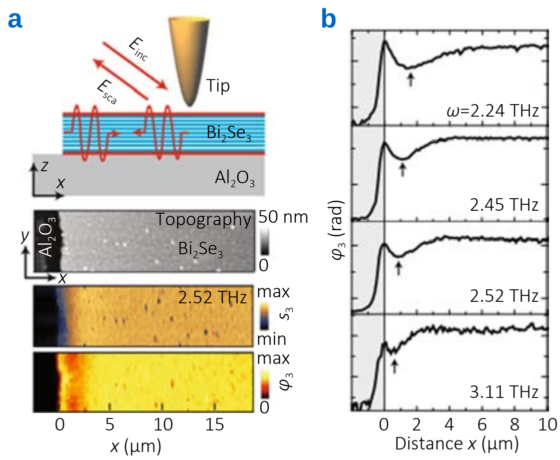

Fig. 72 | Near-field real-space imaging of surface plasmon-polaritons in bismuth selenide. (a) Schematic of polariton mapping alongside the topography, near-field amplitude, and phase images of a 25-nm-thick Bi_2Se_3 film at 2.52 THz, and (b) corresponding near-field phase line profiles at various frequencies. Figure reproduced with permission from ref.[361], under a Creative Commons Attribution License.

thickness-reconstruction algorithm that enabled full three-dimensional morphological recovery of the protein layer[371], as shown in Fig. 78.

Extensive further investigations have employed terahertz near-field platforms to resolve carrier-dynamics processes in materials at micro- and nanometre scales[372−376], as well as to explore novel phenomena emerging from probe-induced perturbations[369, 377−381].

6.3 Future development of terahertz near-field imagimg

Terahertz near-field microscopy has rapidly evolved into a powerful tool for probing electromagnetic-matter interactions at deeply sub-wavelength scales, with demonstrated successes in material characterization, surface-plasmon mapping, phase-change dynamics, biological imaging, and even label-free single-cell diagnostics. By converting evanescent terahertz fields into far-field signals via aperture, photoconductive or scattering-type probes, researchers have routinely broken the Rayleigh limit—reaching spatial resolutions from tens of micrometres (aperture- and photoconductive-probe systems) down to tens of nanometres (THz s-SNOM). Integration with AFM feedback, lock-in demodulation and ultrafast time-domain detection has enabled both high-contrast imaging and local spectroscopy, opening new

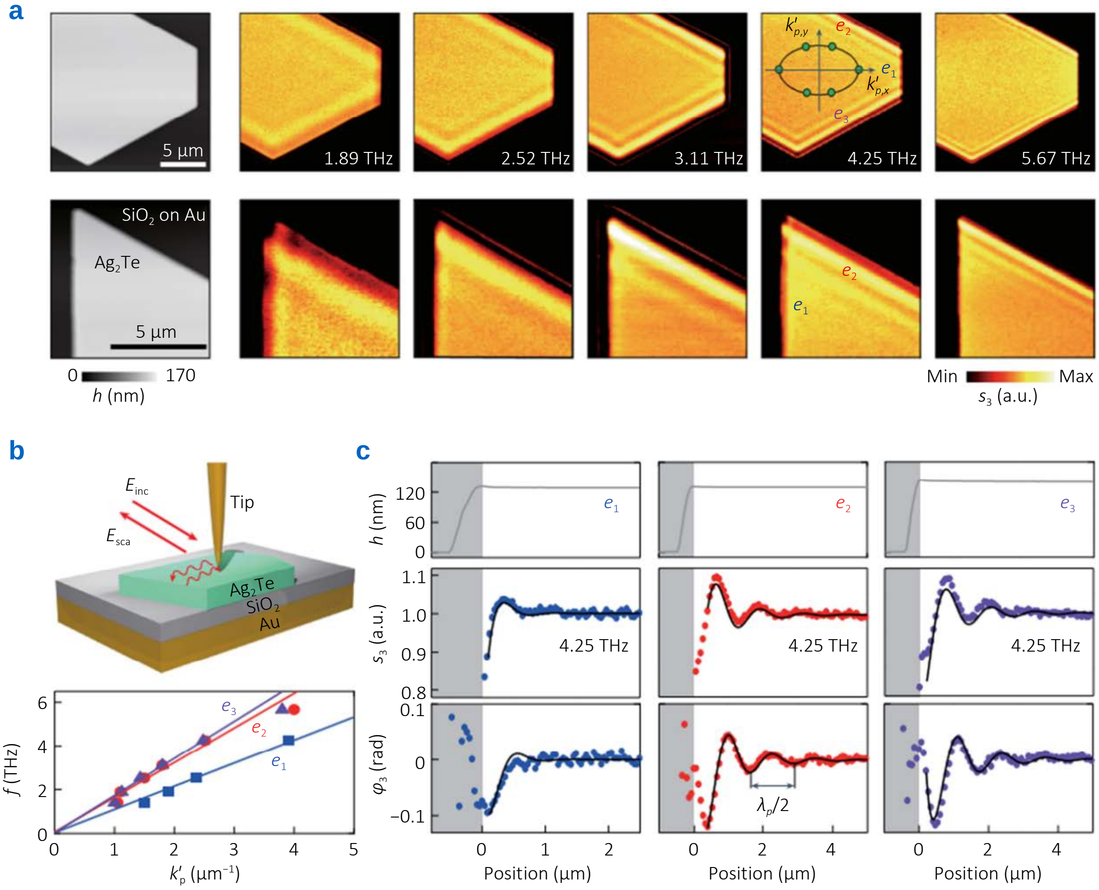

Fig. 73 | Near-field real-space imaging of acoustic surface plasmon-polaritons in silver telluride (Ag_2Te). (a) Topography and THz near-field images of an Ag_2Te platelet, (b) schematic of the experimental setup alongside the corresponding dispersion relations, and (c) extracted near-field line profiles. Figure reproduced with permission from ref.[362], Springer Nature.

windows on carrier dynamics, polariton physics, and nanoscale chemical heterogeneity.

Yet several challenges must be overcome to transition terahertz near-field microscopy from a predominantly academic technique to a broadly deployed analytical tool.

Signal-to-noise ratio: the inherently weak scattering cross-section of sub-wavelength probes demands very high-power sources, low-noise detector. This hardware burden limits sensitivity—especially for materials with low reflectivity or weak dielectric contrast—and slows acquisition times.

Broadband spectroscopy: achieving true broadband spectral coverage remains difficult. Many setups rely on single-frequency continuous-wave sources (e.g., QCLs) or narrow-band electronic multipliers, constraining the accessible spectral window. Pulsed THz-TDS approaches offer wider bandwidth but suffer from lower peak power and require complex phase-stabilized optics.

Quantitative reconstruction: extracting absolute material parameters (e.g., complex permittivity) requires sophisticated probe–sample interaction models and careful calibration. Probe-induced perturbations, dispersion in the optical path and sample topography all introduce uncertainties that

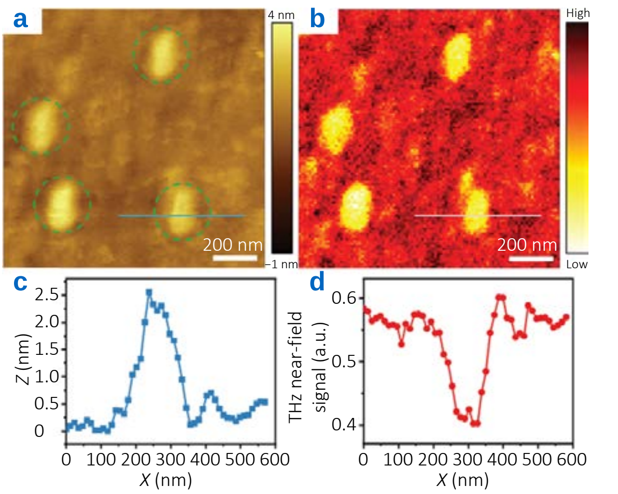

Fig. 74 | Near-field imaging of immunoglobulin molecules using a THz-TDS scattering-type scanning near-field optical microscope (s-SNOM) system. (a) Topography and (b) corresponding THz near-field amplitude images of individual IgG molecules on graphene, alongside (c, d) their respective section profiles. Figure reproduced with permission from ref.[351], John Wiley and Sons.

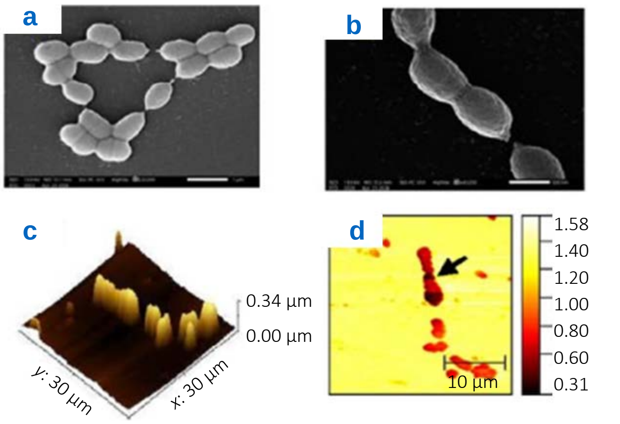

Fig. 75 | Imaging of oral streptococcus by SEM and THz-TDS s-SNOM. (a, b) Scanning electron microscopy (SEM) images at different magnifications, alongside (c) AFM topography and (d) corresponding THz near-field images of Streptococcus salivarius. Figure reproduced with permission from ref.[364], Sage Publications.

must be unraveled by advanced inversion algorithms.

Imaging speed and field of view: raster scanning with nanometre-scale tips is inherently slow, limiting throughput and practical imaging area. Developing high-speed micro-electromechanical scanners or parallel probe arrays will be essential for larger-scale or in vivo applications.

Looking ahead, terahertz near-field microscopy could be revolutionized by on-chip integration, embedding both the time-domain emitter and detector at the tip of the cantilever to enable fully self-aligned measurements. Advances in hybrid-material coatings and nanostructured probes promise to dramatically boost scattering efficiency and improve SNR, while AI-driven algorithms—such as deep-learning–based denoising and quantitative inversion—will allow real-time reconstruction of near-field images. These practical innovations will transform terahertz nanoscopy into an analytical platform for materials science, biomedical diagnostics, and industrial non-destructive testing.

7 Conclusions and outlooks

Terahertz imaging has evolved into a versatile and powerful technology, leveraging the unique properties of terahertz radiation—such as its non-ionizing nature, sensitivity to polar molecules, and material-specific spectral fingerprints—to enable applications across security, biomedicine, industrial inspection, and cultural heritage preservation. This review has surveyed major imaging modalities, including continuous-wave holography, ptychography, computed tomography, focal-plane imaging, single-pixel imaging, and near-field imaging, each offering distinct advantages in resolution, speed, and functionality.

Significant progress has been made in improving imaging performance. Continuous-wave terahertz digital holography achieves submillimeter resolution and video-rate imaging through synthetic aperture and common-path geometries. Terahertz ptychography enables large-field-of-view phase imaging with robust probe and object recovery. Computed tomography benefits from advanced reconstruction algorithms, super-oscillatory lenses, and sparse-angle sampling to enhance quality, resolution, and speed. Focal-plane imaging has overcome early signal-to-noise limitations to support real-time wavefront characterization and

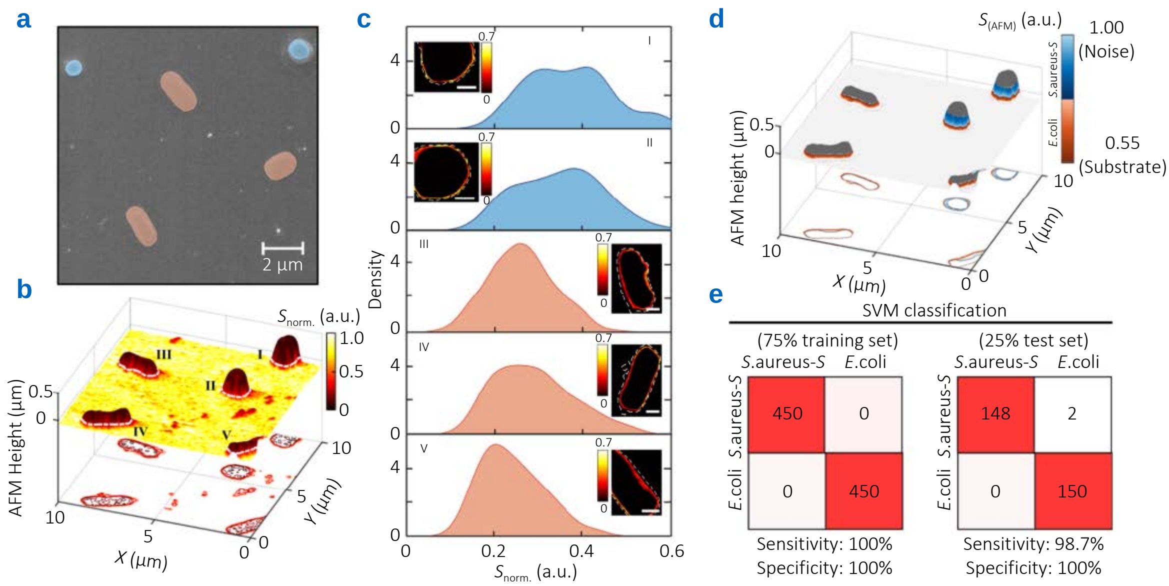

Fig. 76 | Single-bacterium identification using terahertz near-field microscopy. (a) SEM image and (b) near-field intensity overlaid on topography of a pooled bacterial sample. (c) Near-field intensity distributions within a specific height range, (d) height-processed THz nanoimage for noise filtering, and (e) SVM classification error matrix. Figure reproduced with permission from ref.[367], American Chemical Society.

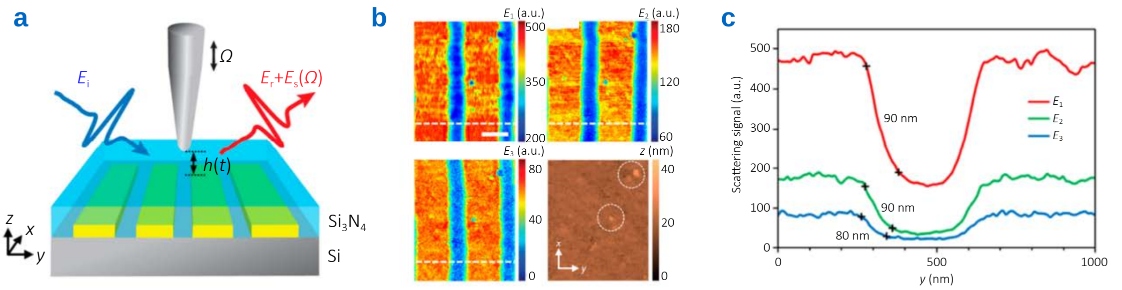

Fig. 77 | Near-field imaging of a silicon-nitride-covered gold grating using a THz-TDS s-SNOM system. (a) Schematic of the THz s-SNOM setup. (b) AFM topography and corresponding THz near-field peak intensity images, alongside (c) extracted near-field profiles revealing topographic artifacts at surface protrusions. Figure reproduced with permission from ref.[77], American Chemical Society.

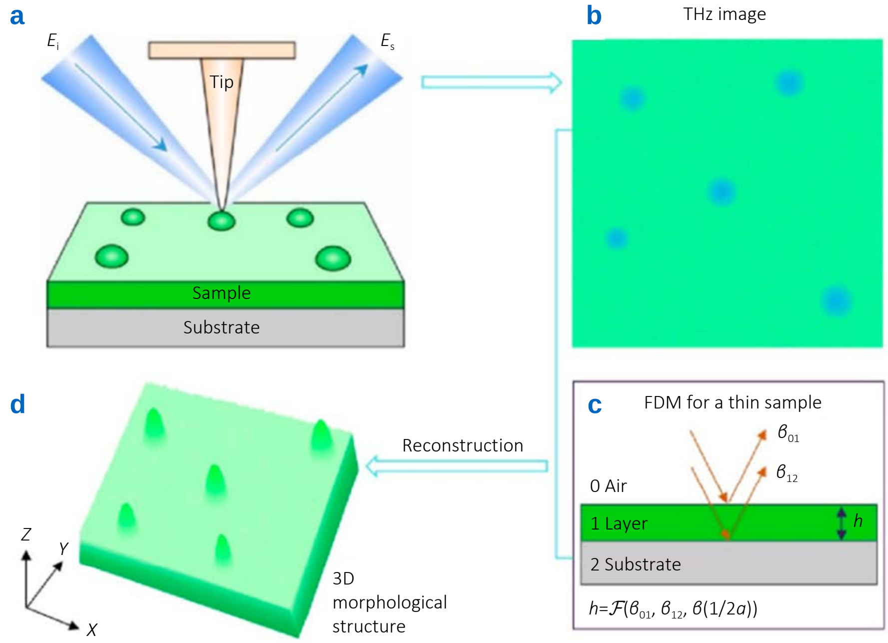

Fig. 78 | Three-dimensional morphological reconstruction of a protein layer using a THz-TDS s-SNOM system. (a) Schematic of the THz s-SNOM setup alongside (b) the acquired near-field amplitude image, (c) the theoretical model for local thickness retrieval, and (d) the final reconstructed 3D morphology. Figure reproduced with permission from ref.[371], American Chemical Society.

meta-surface validation. Single-pixel imaging provides a cost-effective alternative to array detectors, enabling high-resolution and hyperspectral imaging even with limited hardware. Near-field techniques, particularly scattering-type SNOM, have broken the diffraction limit, achieved nanoscale resolution and revealed insights into plasmonic, biological, and material systems. Table 1 presents a comparison of mentioned methods.

Despite these advances, challenges remain. SNRs, hardware integration, imaging speed, and environmental sensitivity continue to limit widespread adoption. Reconstruction artifacts, limited detector dynamic range, and the high cost of sources and modulators also pose barriers to practical deployment. Looking ahead, several trends will shape the future of terahertz imaging:

• Algorithm and AI integration: deep learning and compressed sensing will further optimize reconstruction quality, reduce sampling requirements, and enable real-time imaging.

• Hardware miniaturization and innovation: the development of compact, high-power quantum cascade lasers, sensitive array detectors, and reconfigurable spatial light modulators will enhance portability and performance.

• Multi-modal and multi-spectral imaging: combining terahertz imaging with other modalities (e.g., optical coherence tomography, X-ray, or Raman spectroscopy) will provide complementary information for comprehensive sample analysis.

• Near-field and hyperspectral expansion: advances in near-field probes and broadband sources will enable deeper nanoscale analysis and material-specific identification across wider spectral ranges.

• Application-specific systems: tailored systems for biom-

Table 1 | Comparison of terahertz imaging technologies.

Imaging method	Characteristic resolution	Imaging speed	Information dimension	System complexity	Application fields
Continuous-wave terahertz digital holography	Sub-mm (e. g., 0.1 mm)	Video rate	Amplitude, phase, quantitative phase contrast	Medium	Biomedical sensing, non-destructive testing, security screening
Terahertz ptychography	Lateral: ~2λ, Axial: ~0.03λ	Slow (requires scanning & iteration)	Complex amplitude, large FOV phase contrast	Low (simple optical path)	Label-free in-vivo medical imaging, material analysis
Terahertz computed tomography	~0.5λ (with super-oscillatory lenses)	Medium	3D absorption coefficient	High (requires rotation scanning &complex algorithms)	Cultural heritage preservation, industrial non-destructive testing
Terahertz focal-plane imaging	μm to sub-mm	High-speed (e.g., 69 f/s)	Spatio-temporal distribution, amplitude, phase, polarization	High (requires femtosecond laser & EO crystal)	Wavefront characterization, metasurface verification, chemical/ biological spectral imaging
Terahertz pulse time-domain holography	Wavelength-level	Medium (single-scan full wavefront)	Spatio-temporal, spatio-spectral, complex electric field	High (coherent detection &numerical reconstruction)	Material property retrieval, wavefront metrology, dynamic event analysis
Terahertz single-pixel imaging	μm to sub-mm	Real-time (e.g., 6 f/s)	2D spatial, spectral (with THz-TDS)	Low to medium (depends on modulator type)	Real-time dynamic imaging, spectral Identification
Terahertz near-field imaging	Nanoscale (tens of nm)	Slow (limited by probe scanning)	Nanoscale field distribution, amplitude, phase, spectral	Very high (integrates AFM &terahertz source)	Nanomaterial characterization, plasmonics, biological single-cell imaging

edical diagnostics, pharmaceutical quality control, semiconductor inspection, and cultural heritage preservation will drive commercialization and industrial adoption.

With ongoing innovations in laser sources, detector technology, computational algorithms, and system design, terahertz imaging is poised to transition from laboratory research to real-world applications, offering unprecedented capabilities for non-destructive, label-free, and high-resolution imaging across science and industry.

References

1. Hu BB, Nuss MC. Imaging with terahertz waves. *Opt Lett* **20**, 1716–1718 (1995).
2. Mittleman DM, Jacobsen RH, Nuss MC. T-ray imaging. *IEEE J Sel Top Quant Electr* **2**, 679–692 (1996).
3. Mittleman DM, Gupta M, Neelamani R et al. Recent advances in terahertz imaging. *Appl Phys B Lasers Opt* **68**, 1085–1094 (1999).
4. Zhang XC. Terahertz wave imaging: horizons and hurdles. *Phys Med Biol* **47**, 3667–3677 (2002).
5. Chan WL, Deibel J, Mittleman DM. Imaging with terahertz radiation. *Rep Prog Phys* **70**, 1325–1379 (2007).
6. Mittleman DM. Twenty years of terahertz imaging [invited]. *Opt Express* **26**, 9417–9431 (2018).
7. Li XR, Li JX, Li YH et al. High-throughput terahertz imaging: progress and challenges. *Light Sci Appl* **12**, 233 (2023).
8. Lu Y, Wang XK, Sun WF et al. Reflective single-pixel terahertz imaging based on compressed sensing. *IEEE Trans Terahertz Sci Technol* **10**, 495–501 (2020).
9. Yang ZM, Zhang L, Lu ZJ et al. Robust photonic terahertz vector imaging scheme using an optical frequency comb. *J Lightwave Technol* **40**, 2717–2723 (2022).
10. Fang X, Zhang L, Yang ZM et al. Photonic terahertz hyperspectral imaging with swept-frequency dual combs. *Laser Photonics Rev* **19**, 2400696 (2025).
11. Fang X, Zhang L, Li TY et al. Rapid photonic THz continuous wave compressive imaging with super-resolution over a large field of view. *Optica* **12**, 1800–1810 (2025).
12. Heimbeck MS, Kim MK, Gregory DA et al. Terahertz digital holography using angular spectrum and dual wavelength reconstruction methods. *Opt Express* **19**, 9192–9200 (2011).
13. Xue K, Li Q, Li YD et al. Continuous-wave terahertz in-line digital holography. *Opt Lett* **37**, 3228–3230 (2012).
14. Rong L, Latychevskaia T, Wang DY et al. Terahertz in-line digital holography of dragonfly hindwing: amplitude and phase reconstruction at enhanced resolution by extrapolation. *Opt Express* **22**, 17236–17242 (2014).
15. Zolliker P, Hack E. THz holography in reflection using a high resolution microbolometer array. *Opt Express* **23**, 10957–10967 (2015).
16. Hu JQ, Li Q, Chen GH. Reconstruction of double-exposed terahertz hologram of non-isolated object. *J Infrared, Millimeter, Terahertz Waves* **37**, 328–339 (2016).
17. Huang HC, Wang DY, Li WH et al. Continuous-wave terahertz multi-plane in-line digital holography. *Opt Las Eng* **94**, 76–81 (2017).
18. Yamagiwa M, Ogawa T, Minamikawa T et al. Real-time amplitude and phase imaging of optically opaque objects by combining full-field off-axis terahertz digital holography with angular spectrum reconstruction. *J Infrared, Millimeter, Terahertz Waves* **39**, 561–572 (2018).
19. Wang DY, Zhang YY, Rong L et al. Continuous-wave terahertz self-referencing digital holography based on Fresnel's mirrors. *Opt Lett* **45**, 913–916 (2020).
20. Zhang YY, Zhao J, Wang DY et al. Lensless Fourier-transform terahertz digital holography for real-time full-field phase imaging. *Photonics Res* **10**, 323–331 (2022).
21. Wang DY, Ma DX, Li KL et al. Dynamic full-field refractive index distribution measurements using total internal reflection terahertz digital holography. *Photonics Res* **10**, 289–296 (2022).
22. Jin XY, Zhao J, Wang DY et al. Continuous-wave terahertz in-line holographic diffraction tomography with the scattering fields reconstructed by a physics-enhanced deep neural network. *Photonics Res* **11**, 2149–2158 (2023).
23. Valzania L, Feurer T, Zolliker P et al. Terahertz ptychography. *Opt*

Lett **43**, 543–546 (2018).
24. Rong L, Tang C, Wang DY et al. Probe position correction based on overlapped object wavefront cross-correlation for continuous-wave terahertz ptychography. *Opt Express* **27**, 938–950 (2019).
25. Wang DY, Li B, Rong L et al. Multi-layered full-field phase imaging using continuous-wave terahertz ptychography. *Opt Lett* **45**, 1391–1394 (2020).
26. Rong L, Tang C, Zhao YC et al. Continuous-wave terahertz reflective ptychography by oblique illumination. *Opt Lett* **45**, 4412–4415 (2020).
27. Rong L, Tan FR, Wang DY et al. High-resolution terahertz ptychography using divergent illumination and extrapolation algorithm. *Opt Lasers Eng* **147**, 106729 (2021).
28. Xiang FD, Yu M, Zhang MT et al. Terahertz ptychography using a long-distance diffraction-free beam as the probe. *Opt Lett* **47**, 238–241 (2022).
29. Recur B, Younus A, Salort S et al. Investigation on reconstruction methods applied to 3D terahertz computed tomography. *Opt Express* **19**, 5105–5117 (2011).
30. Recur B, Balacey H, Sleiman JB et al. Ordered subsets convex algorithm for 3D terahertz transmission tomography. *Opt Express* **22**, 23299–23309 (2014).
31. Perraud JB, Chopard A, Guillet JP et al. A versatile illumination system for real-time terahertz imaging. *Sensors* **20**, 3993 (2020).
32. Zhong FS, Niu LT, Wu WW et al. Dictionary learning-based image reconstruction for terahertz computed tomography. *J Infrared, Millimeter, Terahertz Waves* **42**, 829–842 (2021).
33. Wang DY, Ning R, Li GC et al. 3D image reconstruction of terahertz computed tomography at sparse angles by total variation minimization. *Appl Opt* **61**, B1–B7 (2022).
34. Fosodeder P, Hubmer S, Ploier A et al. Phase-contrast THz-CT for non-destructive testing. *Opt Express* **29**, 15711–15723 (2021).
35. Wang TY, Wang KJ, Zou KG et al. Virtual unrolling technology based on terahertz computed tomography. *Opt Lasers Eng* **151**, 106924 (2022).
36. Ning R, Wang DY, Zhao J et al. High accuracy terahertz computed tomography using a 3D printed super-oscillatory lens. *Opt Lasers Eng* **167**, 107610 (2023).
37. Ning R, Wang DY, Zhang YZ et al. Optimized galvanometric illumination for terahertz full-field imaging and computed tomography. *Opt Lasers Eng* **185**, 108714 (2025).
38. Wu Q, Hewitt TD, Zhang XC. Two-dimensional electro-optic imaging of THz beams. *Appl Phys Lett* **69**, 1026–1028 (1996).
39. Jiang ZP, Xu XG, Zhang XC. Improvement of terahertz imaging with a dynamic subtraction technique. *Appl Opt* **39**, 2982–2987 (2000).
40. Yasuda T, Yasui T, Araki T et al. Real-time two-dimensional terahertz tomography of moving objects. *Opt Commun* **267**, 128–136 (2006).
41. Pradarutti B, Müller R, Freese W et al. Terahertz line detection by a microlens array coupled photoconductive antenna array. *Opt Express* **16**, 18443–18450 (2008).
42. Wang XK, Cui Y, Hu D et al. Terahertz quasi-near-field real-time imaging. *Opt Commun* **282**, 4683–4687 (2009).
43. Wang XK, Cui Y, Sun WF et al. Terahertz real-time imaging with balanced electro-optic detection. *Opt Commun* **283**, 4626–4632 (2010).
44. Wang XK, Cui Y, Sun WF et al. Terahertz polarization real-time imaging based on balanced electro-optic detection. *J Opt Soc Am A* **27**, 2387–2393 (2010).
45. Blanchard F, Doi A, Tanaka T et al. Real-time terahertz near-field microscope. *Opt Express* **19**, 8277–8284 (2011).
46. Wang XK, Shi J, Sun WF et al. Longitudinal field characterization of converging terahertz vortices with linear and circular polarizations. *Opt Express* **24**, 7178–7190 (2016).
47. Wu Z, Wang XK, Sun WF et al. Vector characterization of zero-order terahertz Bessel beams with linear and circular polarizations. *Sci Rep* **7**, 13929 (2017).
48. Li HT, Wang XK, Wang S et al. Vector measurement and performance tuning of a terahertz bottle beam. *Sci Rep* **8**, 13177 (2018).
49. Li JT, Wang GC, Yue Z et al. Dynamic phase assembled terahertz metalens for reversible conversion between linear polarization and arbitrary circular polarization. *Opto-Electron Adv* **5**, 210062 (2022).
50. Zhao H, Wang XK, Liu ST et al. Highly efficient vectorial field manipulation using a transmitted tri-layer metasurface in the terahertz band. *Opto-Electron Adv* **6**, 220012 (2023).
51. Wang GC, Hu B, Zhao H et al. Pump-wavelength sensitive terahertz spatiotemporal metasurface. *Adv Opt Mater* **12**, 2301994 (2024).
52. Nan T, Zhao H, Guo JY et al. Generation of structured light beams with polarization variation along arbitrary spatial trajectories using tri-layer metasurfaces. *Opto-Electron Sci* **3**, 230052 (2024).
53. Li C, Xiang XC, Wang P et al. Imaging-based terahertz pixelated metamaterials for molecular fingerprint sensing. *Opt Express* **32**, 27473–27481 (2024).
54. Yang SX, Ding L, Wang S et al. Studying oral tissue via real-time high-resolution terahertz spectroscopic imaging. *Phys Rev Appl* **19**, 034033 (2023).
55. Dong JL, You P, Tomasino A et al. Single-shot ultrafast terahertz photography. *Nat Commun* **14**, 1704 (2023).
56. Zhang Y, Zhou W, Wang X et al. Terahertz digital holography. *Strain* **44**, 380–385 (2008).
57. Petrov NV, Kulya MS, Tsypkin AN et al. Application of terahertz pulse time-domain holography for phase imaging. *IEEE Trans Terahertz Sci Technol* **6**, 464–472 (2016).
58. Kulya MS, Balbekin NS, Gredyuhina IV et al. Computational terahertz imaging with dispersive objects. *J Mod Opt* **64**, 1283–1288 (2017).
59. Kulya MS, Semenova VA, Bespalov VG et al. On terahertz pulsed broadband Gauss-Bessel beam free-space propagation. *Sci Rep* **8**, 1390 (2018).
60. Kulya M, Semenova V, Gorodetsky A et al. Spatio-temporal and spatiospectral metrology of terahertz broadband uniformly topologically charged vortex beams. *Appl Opt* **58**, A90–A100 (2019).
61. Kulya M, Petrov NV, Tsypkin A et al. Hyperspectral data denoising for terahertz pulse time-domain holography. *Opt Express* **27**, 18456–18476 (2019).
62. Kulya M, Petrov NV, Katkovnik V et al. Terahertz pulse time-domain holography with balance detection: complex-domain sparse imaging. *Appl Opt* **58**, G61–G70 (2019).
63. Kulya MS, Odlyanitskiy EL, Cassar Q et al. Fast terahertz spectroscopic holographic assessment of optical properties of diabetic blood plasma. *J Infrared, Millimeter, Terahertz Waves* **41**, 1041–1056 (2020).
64. Petrov NV, Kulya MS, Gorodetsky AA et al. On the features of the interference of a set of broadband uniformly topologically charged beams. *Proc SPIE* **11499**, 114990I (2020).
65. Grachev YV, Kokliushkin VA, Petrov NV. Open-source 3D-printed terahertz pulse time-domain holographic detection module. *Appl Opt* **61**, B307–B313 (2022).
66. Petrov NV, Sokolenko B, Kulya MS et al. Design of broadband terahertz vector and vortex beams: I. Review of materials and compo-

nents. *Light Adv Manuf* **3**, 43 (2022).
67. Petrov NV, Sokolenko B, Kulya MS et al. Design of broadband terahertz vector and vortex beams: II. Holographic assessment. *Light Adv Manuf* **3**, 44 (2022).
68. Tsiplakova EG, Grachev YV, Petrov NV. Overcoming the trade-off between signal-to-noise ratio and resolution in holographic registration of pulsed terahertz Gauss-Bessel beams. *Appl Phys Lett* **125**, 091108 (2024).
69. Kwak N. Principal component analysis based on L1-norm maximization. *IEEE Trans Pattern Anal Mach Intell* **30**, 1672–1680 (2008).
70. Mandal P, Speck A, Ko C et al. Terahertz spectroscopy studies on epitaxial vanadium dioxide thin films across the metal-insulator transition. *Opt Lett* **36**, 1927–1929 (2011).
71. Watts CM, Shrekenhamer D, Montoya J et al. Terahertz compressive imaging with metamaterial spatial light modulators. *Nat Photonics* **8**, 605–609 (2014).
72. Stantchev RI, Sun BQ, Hornett SM et al. Noninvasive, near-field terahertz imaging of hidden objects using a single-pixel detector. *Sci Adv* **2**, e1600190 (2016).
73. Malevich Y, Ergoktas MS, Bakan G et al. Video-speed graphene modulator arrays for terahertz imaging applications. *ACS Photonics* **7**, 2374–2380 (2020).
74. Vallés A, He JH, Ohno S et al. Broadband high-resolution terahertz single-pixel imaging. *Opt Express* **28**, 28868–28881 (2020).
75. Stantchev RI, Yu X, Blu T et al. Real-time terahertz imaging with a single-pixel detector. *Nat Commun* **11**, 2535 (2020).
76. Li WL, Hu XM, Wu JB et al. Dual-color terahertz spatial light modulator for single-pixel imaging. *Light Sci Appl* **11**, 191 (2022).
77. Moon K, Park H, Kim J et al. Subsurface nanoimaging by broadband terahertz pulse near-field microscopy. *Nano Lett* **15**, 549–552 (2015).
78. Degl'Innocenti R, Wallis R, Wei BB et al. Terahertz nanoscopy of plasmonic resonances with a quantum cascade laser. *ACS Photonics* **4**, 2150–2157 (2017).
79. Dai GB, Geng GS, Zhang XX et al. W-band near-field microscope. *IEEE Access* **7**, 48060–48067 (2019).
80. Moon K, Do Y, Park H et al. Computed terahertz near-field mapping of molecular resonances of lactose stereo-isomer impurities with sub-attomole sensitivity. *Sci Rep* **9**, 16915 (2019).
81. Chen C, Chen S, Lobo RPSM et al. Terahertz nanoimaging and nanospectroscopy of chalcogenide phase-change materials. *ACS Photonics* **7**, 3499–3506 (2020).
82. Jing R, Shao YM, Fei ZY et al. Terahertz response of monolayer and few-layer WTe_2 at the nanoscale. *Nat Commun* **12**, 5594 (2021).
83. Xu XX, Zhang XQY, Zhang TY et al. Near-field observation of enhanced resonance in metasurface by cavity mode coupling. *Opt Express* **33**, 14048–14060 (2025).
84. Garcia-Sucerquia J, Xu WB, Jericho SK et al. Digital in-line holographic microscopy. *Appl Opt* **45**, 836–850 (2006).
85. Wang XK, Cui Y, Sun WF et al. Terahertz digital holography. *Proc SPIE* **8330**, 833003 (2012).
86. Wang XK, Wang S, Sun WF et al. Visualization of terahertz surface waves propagation on metal foils. *Sci Rep* **6**, 18768 (2016).
87. Gabor D. A new microscopic principle. *Nature* **161**, 777–778 (1948).
88. Chen GH, Li Q. Markov chain Monte Carlo sampling based terahertz holography image denoising. *Appl Opt* **54**, 4345–4351 (2015).
89. Li Q, Xue K, Li YD et al. Experimental research on terahertz Gabor inline digital holography of concealed objects. *Appl Opt* **51**, 7052–7058 (2012).
90. Hu JQ, Li Q, Zhou Y. Support-domain constrained phase retrieval algorithms in terahertz in-line digital holography reconstruction of a nonisolated amplitude object. *Appl Opt* **55**, 379–386 (2016).
91. Cheng KY, Li Q. Application of acquiring region of interest based on the $YOLOv_5$ model in terahertz digital holography. *Appl Opt* **62**, 3589–3597 (2023).
92. Li ZY, Yan Q, Qin Y et al. Sparsity-based continuous wave terahertz lens-free on-chip holography with sub-wavelength resolution. *Opt Express* **27**, 702–713 (2019).
93. Liu YM, Fan FF, Li JW et al. Total variation extrapolation algorithm for high-fidelity terahertz in-line digital holography. *Opt Lasers Eng* **193**, 109048 (2025).
94. Jin XY, Zhao J, Wang DY et al. Iterative denoising phase retrieval method for twin-image elimination in continuous-wave terahertz in-line digital holography. *Opt Lasers Eng* **152**, 106986 (2022).
95. Hislop G, Li L, Hellicar A. Phase retrieval for millimeter- and submillimeter-wave imaging. *IEEE Trans Antennas Propagat* **57**, 286–290 (2009).
96. Petrov NV, Perraud JB, Chopard A et al. Terahertz phase retrieval imaging in reflection. *Opt Lett* **45**, 4168–4171 (2020).
97. Tsiplakova EG, Perraud JB, Guillet JP et al. Terahertz diffractive imaging with saturated data inpainting. *Opt Lett* **48**, 5463–5466 (2023).
98. Tsiplakova EG, Chopard A, Balbekin NS et al. An algorithm of unordered wavefront propagation in terahertz phase retrieval with dense multiplane data acquisition. *Comput Opt* **47**, 901–912 (2023).
99. Latychevskaia T, Fink HW. Resolution enhancement in digital holography by self-extrapolation of holograms. *Opt Express* **21**, 7726–7733 (2013).
100. Latychevskaia T, Fink HW. Coherent microscopy at resolution beyond diffraction limit using post-experimental data extrapolation. *Appl Phys Lett* **103**, 204105 (2013).
101. Rong L, Latychevskaia T, Chen CH et al. Terahertz in-line digital holography of human hepatocellular carcinoma tissue. *Sci Rep* **5**, 8445 (2015).
102. Huang HC, Qiu PY, Panezai S et al. Continuous-wave terahertz high-resolution imaging via synthetic hologram extrapolation method using pyroelectric detector. *Opt Laser Technol* **120**, 105683 (2019).
103. Li ZY, Yan Q, Qin Y et al. Resolution enhancement in terahertz digital in-line holography by sparsity-based extrapolation. *J Infrared, Millimeter, Terahertz Waves* **42**, 479–492 (2021).
104. Wang Y, Li Q. High-resolution terahertz digital holography based on frequency-domain diagonal extension imaging. *Opt Quant Electron* **55**, 235 (2023).
105. Li ZY, Li L, Qin Y et al. Resolution and quality enhancement in terahertz in-line holography by sub-pixel sampling with double-distance reconstruction. *Opt Express* **24**, 21134–21146 (2016).
106. Huang HC, Rong L, Wang DY et al. Synthetic aperture in terahertz in-line digital holography for resolution enhancement. *Appl Opt* **55**, A43–A48 (2016).
107. Deng QH, Li WH, Wang XM et al. High-resolution terahertz inline digital holography based on quantum cascade laser. *Opt Eng* **56**, 113102 (2017).
108. Li ZY, Zou RJ, Kong WP et al. Terahertz synthetic aperture in-line holography with intensity correction and sparsity autofocusing reconstruction. *Photonics Res* **7**, 1391–1399 (2019).
109. Huang HC, Wang DY, Rong L et al. Application of autofocusing

methods in continuous-wave terahertz in-line digital holography. *Opt Commun* **346**, 93–98 (2015).

110. Huang HC, Wang DY, Rong L et al. Continuous-wave off-axis and in-line terahertz digital holography with phase unwrapping and phase autofocusing. *Opt Commun* **426**, 612–622 (2018).
111. Huang HC, Yang MH, Li ZJ et al. Terahertz holographic detection for high-resolution sensing of axially diverse targets. *Meas Sci Technol* **36**, 055210 (2025).
112. Li YD, Li Q, Hu JQ et al. Compressive sensing algorithm for 2D reconstruction of THz digital holography. *Chin Opt Lett* **13**, S11101 (2015).
113. Li Q, Li YD. Continuous-wave 2.52 terahertz Gabor inline compressive holographic tomography. *Appl Phys B* **117**, 585–596 (2014).
114. Mahon R, Murphy A, Lanigan W. Terahertz holographic image reconstruction and analysis. In *Infrared and Millimeter Waves, Conference Digest of the 2004 Joint 29th International Conference on 2004 and 12th International Conference on Terahertz Electronics* 749–750 (IEEE, 2004). http://doi.org/10.1109/ICIMW.2004.1422309.
115. Mahon RJ, Murphy JA, Lanigan W. Digital holography at millimetre wavelengths. *Opt Commun* **260**, 469–473 (2006).
116. Ding SH, Li Q, Li YD et al. Continuous-wave terahertz digital holography by use of a pyroelectric array camera. *Opt Lett* **36**, 1993–1995 (2011).
117. Li Q, Ding SH, Li YD et al. Research on reconstruction algorithms in 2.52 THz off–axis digital holography. *J Infrared, Millimeter, Terahertz Waves* **33**, 1039–1051 (2012).
118. Li Q, Ding SH, Li YD et al. Experimental research on resolution improvement in CW THz digital holography. *Appl Phys B* **107**, 103–110 (2012).
119. Sobczyk A, Makowski M, Kowalczyk A et al. Polarization-maintaining diffractive elements for off-axis terahertz digital holography. *J Infrared, Millimeter, Terahertz Waves* **44**, 212–219 (2023).
120. Kirkove M, Zhao YC, Leblanc O et al. ADMM-inspired image reconstruction for terahertz off-axis digital holography. *J Opt Soc Am A Opt Image Sci Vis* **41**, A1–A14 (2024).
121. Hack E, Zolliker P. Terahertz holography for imaging amplitude and phase objects. *Opt Express* **22**, 16079–16086 (2014).
122. Heimbeck MS, Ng WR, Golish DR et al. Terahertz digital holographic imaging of voids within visibly opaque dielectrics. *IEEE Trans Terahertz Sci Technol* **5**, 110–116 (2015).
123. Locatelli M, Ravaro M, Bartalini S et al. Real-time terahertz digital holography with a quantum cascade laser. *Sci Rep* **5**, 13566 (2015).
124. Zhao YC, Vandenrijt J, Kirkove M et al. Imaging quality and resolution enhancement by iterative phase retrieval in THz off-axis digital holography. In *Digital Holography and Three-Dimensional Imaging 2019* Th4B. 3 (Optica Publishing Group, 2019). http://doi.org/10.1364/DH.2019.Th4B.3.
125. Zhao YC, Kirkove M, Georges MP. Inverse-problem based algorithm for THz off-axis digital holography reconstruction. In *Imaging and Applied Optics Congress* HF4G. 6 (Optica Publishing Group, 2020). http://doi.org/10.1364/DH.2020.HF4G.6.
126. Valzania L, Zolliker P, Hack E. Topography of hidden objects using THz digital holography with multi-beam interferences. *Opt Express* **25**, 11038–11047 (2017).
127. Ibrahim DGA. Steep large film thickness measurement with off-axis terahertz digital holography reconstructed by a direct Fourier and Hermite polynomial. *Appl Opt* **57**, 2533–2538 (2018).
128. Humphreys M, Grant JP, I. Escorcia-Carranza I et al. Video-rate terahertz digital holographic imaging system. *Opt Express* **26**, 25805–25813 (2018).
129. Wan M, Wang DY, Rong L et al. Continuous-wave terahertz reflective off-axis digital holography. *Proc SPIE* **10157**, 101571U (2016).
130. Wang DY, Zhao YL, Rong L et al. Expanding the field-of-view and profile measurement of covered objects in continuous-wave terahertz reflective digital holography. *Opt Eng* **58**, 023111 (2019).
131. Zolliker P, Hack E. Resolution limits of terahertz holography using a QCL. In *2014 39th International Conference on Infrared, Millimeter, and Terahertz waves (IRMMW-THz)* 1–2 (IEEE, 2014). http://doi.org/10.1109/IRMMW-THz.2014.6956018.
132. Wang YX, Zhao ZR, Chen ZQ et al. Continuous-wave terahertz phase imaging using a far-infrared laser interferometer. *Appl Opt* **50**, 6452–6460 (2011).
133. Yamagiwa M, Minamikawa T, Minamiji F et al. Visualization of internal structure and internal stress in visibly opaque objects using full-field phase-shifting terahertz digital holography. *Opt Express* **27**, 33854–33868 (2019).
134. Siemion A, Minkevičius L, Jokubauskis D et al. Terahertz digital holography: two- and four-step phase shifting technique in two plane image recording. *AIP Adv* **11**, 105212 (2021).
135. Penketh H, Ergoktas MS, Lawrence CR et al. Real-time millimeter wave holography with an arrayed detector. *Opt Express* **32**, 5783–5792 (2024).
136. Mrnka M, Penketh H, Phillips DB et al. Rapid terahertz beam profiling and antenna characterization with phase-shifting holography. *Sci Rep* **14**, 21056 (2024).
137. Wang XK, Hou L, Zhang Y. Continuous-wave terahertz interferometry with multiwavelength phase unwrapping. *Appl Opt* **49**, 5095–5102 (2010).
138. Petrov NV, Bespalov VG, Volkov MV. Phase retrieval of THz radiation using set of 2D spatial intensity measurements with different wavelengths. *Proc SPIE* **8281**, 82810J (2012).
139. Zhang YY, Zhao J, Wang DY et al. Lensless Fourier-transform terahertz digital holography for full-field reflective imaging. *Front Phys* **9**, 818130 (2022).
140. Shi HF, Wang KJ, Chen WL et al. Generation of a terahertz quasi-Pearcey beam and its investigation in ptychography. *Opt Express* **32**, 2607–2618 (2024).
141. Recur B. Terahertz radiation for tomographic inspection. *Opt Eng* **51**, 091609 (2012).
142. Tepe J, Schuster T, Littau B. A modified algebraic reconstruction technique taking refraction into account with an application in terahertz tomography. *Inverse Probl Sci Eng* **25**, 1448–1473 (2016).
143. Mohr T, Herdt A, Elsässer W. 2D tomographic terahertz imaging using a single pixel detector. *Opt Express* **26**, 3353–3367 (2018).
144. Gu L, Zhou T, Tan ZY et al. Computed tomography using a terahertz quantum cascade laser and quantum well photo-detector. *J Opt* **15**, 105701 (2013).
145. Zhou T, Zhang R, Yao C et al. Terahertz three-dimensional imaging based on computed tomography with photonics-based noise source. *Chin Phys Lett* **34**, 084206 (2017).
146. Chen LY, Wang YY, Xu DG et al. Terahertz computed tomography of high-refractive-index objects based on refractive index matching. *IEEE Photonics J* **10**, 5900813 (2018).
147. Fosodeder P, Van Frank S, Rankl C. Highly accurate THz-CT including refraction effects. *Opt Express* **30**, 3684–3699 (2022).
148. May KH, Keil A, Von Freymann G et al. The conjugate gradient least square algorithm in terahertz tomography. *IEEE Access* **9**, 142168–142178 (2021).
149. Hung YC, Chao TH, Yu P et al. Terahertz spatio-temporal deep learning computed tomography. *Opt Express* **30**, 22523–22537

(2022).
150. Bitman A, Goldring S, Moshe I et al. Computed tomography using broadband Bessel THz beams and phase contrast. *Opt Lett* **39**, 1925–1928 (2014).
151. Niu LT, Wu Q, Wang KJ et al. THz computed tomography system with zero-order Bessel beam. *Proc SPIE* **10623**, 1062303 (2018).
152. Ok G, Choi SW, Park K et al. Foreign object detection by sub-terahertz quasi-Bessel beam imaging. *Sensors* **13**, 71–85 (2013).
153. Wang DY, Li B, Rong L et al. Extended depth of field in continuous-wave terahertz computed tomography based on Bessel beam. *Opt Commun* **432**, 20–26 (2019).
154. Ruan DS, Li ZY, Du LH et al. Realizing a terahertz far-field sub-diffraction optical needle with sub-wavelength concentric ring structure array. *Appl Opt* **57**, 7905–7909 (2018).
155. Yang MY, Ruan DS, Du LH et al. Subdiffraction focusing of total electric fields of terahertz wave. *Opt Commun* **458**, 124764 (2020).
156. Wu P, Sun X, Yao N et al. Experimental study of terahertz superfocusing with super-oscillation phenomenon. *Opt Commun* **515**, 128185 (2022).
157. Iba A, Domier CW, Ikeda M et al. Subdiffraction focusing with a long focal length using a terahertz-wave super-oscillatory lens. *Opt Lett* **46**, 4912–7915 (2021).
158. Minkevičius L, Indrišiūnas S, Šniaukas R et al. Terahertz multilevel phase Fresnel lenses fabricated by laser patterning of silicon. *Opt Lett* **42**, 1875–1878 (2017).
159. Jokubauskis D, Minkevičius L, Karaliūnas M et al. Fibonacci terahertz imaging by silicon diffractive optics. *Opt Lett* **43**, 2795–2798 (2018).
160. Minkevičius L, Jokubauskis D, Kašalynas I et al. Bessel terahertz imaging with enhanced contrast realized by silicon multi-phase diffractive optics. *Opt Express* **27**, 36358–36367 (2019).
161. Li Q, Li YD, Ding SH et al. Terahertz computed tomography using a continuous-wave gas laser. *J Infrared, Millimeter, Terahertz Waves* **33**, 548–558 (2012).
162. Jewariya M, Abraham E, Kitaguchi T et al. Fast three-dimensional terahertz computed tomography using real-time line projection of intense terahertz pulse. *Opt Express* **21**, 2423–2433 (2013).
163. Ok G, Park K, Kim HJ et al. High-speed terahertz imaging toward food quality inspection. *Appl Opt* **53**, 1406–1412 (2014).
164. Ok G, Park K, Chun HS et al. High-performance sub-terahertz transmission imaging system for food inspection. *Biomed Opt Express* **6**, 1929–1941 (2015).
165. Rothbart N, Richter H, Wienold M et al. Fast 2-D and 3-D terahertz imaging with a quantum-cascade laser and a scanning mirror. *IEEE Trans Terahertz Sci Technol* **3**, 617–624 (2013).
166. Li B, Wang DY, Zhou X et al. Continuous-wave terahertz digital holographic tomography with a pyroelectric array detector. *Opt Eng* **55**, 053106 (2016).
167. Rong L, Zhang YZ, Ge L et al. Uniformity optimization of galvanometric illumination. *Opt Laser Technol* **181**, 111665 (2025).
168. Mittleman DM, Hunsche S, Boivin L et al. T-ray tomography. *Opt Lett* **22**, 904–906 (1997).
169. Wu Q, Zhang XC. Free-space electro-optic sampling of terahertz beams. *Appl Phys Lett* **67**, 3523–3525 (1995).
170. Wu Q, Sun FG, Campbell P et al. Dynamic range of an electro-optic field sensor and its imaging applications. *Appl Phys Lett* **68**, 3224–3226 (1996).
171. Planken PCM, Nienhuys HK, Bakker HJ et al. Measurement and calculation of the orientation dependence of terahertz pulse detection in ZnTe. *J Opt Soc Am B* **18**, 313–317 (2001).
172. van der Valk NCJ, Wenckebach T, Planken PCM. Full mathematical description of electro-optic detection in optically isotropic crystals. *J Opt Soc Am B* **21**, 622–631 (2004).
173. Zhang RX, Cui Y, Sun WF et al. Polarization information for terahertz imaging. *Appl Opt* **47**, 6422–6427 (2008).
174. Hebling J, Yeh KL, Hoffmann MC et al. Generation of high-power terahertz pulses by tilted-pulse-front excitation and their application possibilities. *J Opt Soc Am B* **25**, B6–B19 (2008).
175. Blanchard F, Tanaka K. Improving time and space resolution in electro-optic sampling for near-field terahertz imaging. *Opt Lett* **41**, 4645–4648 (2016).
176. Winnerl S, Hubrich R, Mittendorff M et al. Universal phase relation between longitudinal and transverse fields observed in focused terahertz beams. *New J Phys* **14**, 103049 (2012).
177. Seo MA, Adam AJL, Kang JH et al. Fourier-transform terahertz near-field imaging of one-dimensional slit arrays: mapping of electric-field-, magnetic-field-, and Poynting vectors. *Opt Express* **15**, 11781–11789 (2007).
178. Wang XK, Wang S, Xie ZW et al. Full vector measurements of converging terahertz beams with linear, circular, and cylindrical vortex polarization. *Opt Express* **22**, 24622–24634 (2014).
179. Schirmer M, Fujio M, Minami M et al. Biomedical applications of a real-time terahertz color scanner. *Biomed Opt Express* **1**, 354–366 (2010).
180. Jiang ZP, Zhang XC. 2D measurement and spatio-temporal coupling of few-cycle THz pulses. *Opt Express* **5**, 243–248 (1999).
181. Zhan QW. Properties of circularly polarized vortex beams. *Opt Lett* **31**, 867–869 (2006).
182. Nanni EA, Huang WR, Hong KH et al. Terahertz-driven linear electron acceleration. *Nat Commun* **6**, 8486 (2015).
183. Nagatsuma T, Ducournau G, Renaud CC. Advances in terahertz communications accelerated by photonics. *Nat Photonics* **10**, 371–379 (2016).
184. Wang XK, Sun WF, Cui Y et al. Complete presentation of the Gouy phase shift with the THz digital holography. *Opt Express* **21**, 2337–2346 (2013).
185. Shang YJ, Wang XK, Sun WF et al. Polarization determination based on the longitudinal field of a converging terahertz wave. *Opt Lett* **43**, 5508–5511 (2018).
186. Brossard M, Sauvage JF, Perrin M et al. Terahertz adaptive optics with a deformable mirror. *Opt Lett* **43**, 1594–1597 (2018).
187. Yu NF, Genevet P, Kats MA et al. Light propagation with phase discontinuities: generalized laws of reflection and refraction. *Science* **334**, 333–337 (2011).
188. Hu D, Wang XK, Feng SF et al. Ultrathin terahertz planar elements. *Adv Opt Mater* **1**, 186–191 (2013).
189. Wang B, Quan BG, He JW et al. Wavelength de-multiplexing metasurface hologram. *Sci Rep* **6**, 35657 (2016).
190. Zhao H, Quan BG, Wang XK et al. Demonstration of orbital angular momentum multiplexing and demultiplexing based on a metasurface in the terahertz band. *ACS Photonics* **5**, 1726–1732 (2018).
191. Guo JY, Wang XK, He JW et al. Generation of radial polarized Lorentz beam with single layer metasurface. *Adv Opt Mater* **6**, 1700925 (2018).
192. Li HT, Wang XK, Wang S et al. Realization and characterization of terahertz surface plasmon light capsules. *Appl Phys Lett* **114**, 091110 (2019).
193. Usami M, Yamashita M, Fukushima K et al. Terahertz wideband spectroscopic imaging based on two-dimensional electro-optic sampling technique. *Appl Phys Lett* **86**, 141109 (2005).
194. Zhong H, Redo-Sanchez A, Zhang XC. Identification and classification of chemicals using terahertz reflective spectroscopic focal-

plane imaging system. Opt Express **14**, 9130–9141 (2006).
195. Yasuda T, Kawada Y, Toyoda H et al. Fast frequency-resolved terahertz imaging. Rev Sci Instrum **82**, 034708 (2011).
196. Guo LH, Wang XK, Han P et al. Observation of dehydration dynamics in biological tissues with terahertz digital holography [invited]. Appl Opt **56**, F173–F178 (2017).
197. Feurer T, Vaughan JC, Nelson KA. Spatiotemporal coherent control of lattice vibrational waves. Science **299**, 374–377 (2003).
198. Wu Q, Werley CA, Lin KH et al. Quantitative phase contrast imaging of THz electric fields in a dielectric waveguide. Opt Express **17**, 9219–9225 (2009).
199. Werley CA, Wu Q, Lin KH et al. Comparison of phase-sensitive imaging techniques for studying terahertz waves in structured $LiNbO_3$. J Opt Soc Am B **27**, 2350–2359 (2010).
200. Li XR, Mengu D, Yardimci NT et al. Plasmonic photoconductive terahertz focal-plane array with pixel super-resolution. Nat Photonics **18**, 139–148 (2024).
201. Tamaki R, Kasai T, Asai G et al. Pulse-to-pulse detection of terahertz radiation emitted from the femtosecond laser ablation process. Opt Express **30**, 23622–23630 (2022).
202. Chizhov PA, Komlenok MS, Kononenko VV et al. Photoconductive terahertz generation in nitrogen-doped single-crystal diamond. Opt Lett **47**, 86–89 (2022).
203. Lee G, Son B, Ko DK et al. High efficiency interdigitated terahertz photoconductive antenna integrated with cylindrical lens array. IEEE Trans Terahertz Sci Technol **13**, 671–677 (2023).
204. Tangen IC, Valdivia-Berroeta GA, Heki LK et al. Comprehensive characterization of terahertz generation with the organic crystal BNA. J Opt Soc Am B **38**, 2780–2785 (2021).
205. Carnio BN, Zhang M, Schunemann PG et al. Emission and sensing of high-frequency terahertz electric fields using a GaSe crystal. Opt Express **31**, 3304–3314 (2023).
206. Kim H, Kang C, Jang D et al. Ionizing terahertz waves with 260 MV/cm from scalable optical rectification. Light Sci Appl **13**, 118 (2024).
207. Ruan HH, Tan ZY, Chen LT et al. Efficient sub-pixel convolutional neural network for terahertz image super-resolution. Opt Lett **47**, 3115–3118 (2022).
208. Deng YQ, She RB, Liu WQ et al. High-efficiency terahertz single-pixel imaging based on a physics-enhanced network. Opt Express **31**, 10273–10286 (2023).
209. Lee SH, Shin S, Roh Y et al. Label-free brain tissue imaging using large-area terahertz metamaterials. Biosens Bioelectron **170**, 112663 (2020).
210. Ha T, Yoo D, Heo C et al. Subwavelength terahertz resonance imaging (STRING) for molecular fingerprinting. Nano Lett **22**, 10200–10207 (2022).
211. Petrov NV, Gorodetsky AA, Bespalov VG. Holography and phase retrieval in terahertz imaging. Proc SPIE **8846**, 88460S (2013).
212. Semenova VA, Kulya MS, Petrov NV et al. Amplitude-phase imaging of pulsed broadband terahertz vortex beams generated by spiral phase plate. In *2016 41st International Conference on Infrared, Millimeter, and Terahertz Waves (IRMMW-THz)* 1–2 (IEEE, 2016). http://doi.org/10.1109/IRMMW-THz.2016.7758823.
213. Petrov NV, Bespalov VG, Kulya MS. Terahertz pulse time-domain holography for studying of broadband beams propagation dynamics. In *Imaging and Applied Optics 2018 (3D, AO, AIO, COSI, DH, IS, LACSEA, LS&C, MATH, pcAOP)* DTu2F. 7 (Optica Publishing Group, 2018). http://doi.org/10.1364/DH.2018.DTu2F.7.
214. Liu X, Kulya MS, Petrov NV et al. Spectral Fresnel filter for pulsed broadband terahertz radiation. AIP Adv **10**, 125104 (2020).
215. Kulya MS, Sokolenko B, Gorodetsky A et al. Propagation dynamics of ultrabroadband terahertz beams with orbital angular momentum for wireless data transfer. Proc SPIE **11307**, 113070J (2020).
216. Kulya MS, Balbekin NS, Gorodetsky AA et al. Vectorial terahertz pulse time-domain holography for broadband optical wavefront sensing. Proc SPIE **11279**, 112790D (2020).
217. Balbekin NS, Kulya MS, Belashov AV et al. Increasing the resolution of the reconstructed image in terahertz pulse time-domain holography. Sci Rep **9**, 180 (2019).
218. Elias E, Sideris S, McDonnell C et al. Generating angular-varying time delays of THz pulses via direct space-to-time mapping of metasurface structures. ACS Appl Opt Mater **1**, 1783–1790 (2023).
219. Wang Q, Zhang XQ, Plum E et al. Polarization and frequency multiplexed terahertz meta-holography. Adv Opt Mater **5**, 1700277 (2017).
220. Shen ZX, Tang MJ, Chen P et al. Planar terahertz photonics mediated by liquid crystal polymers. Adv Opt Mater **8**, 1902124 (2020).
221. Shen ZX, Zhou SH, Li XA et al. Liquid crystal integrated metalens with tunable chromatic aberration. Adv Photonics **2**, 036002 (2020).
222. Grachev YV, Kokliushkin VA, Petrov NV. An open-source 3D-printed terahertz pulse time-domain holographic detection module for broadband beam inspection. In *2020 45th International Conference on Infrared, Millimeter, and Terahertz Waves (IRMMW-THz)* 1–2 (IEEE, 2020). http://doi.org/10.1109/IRMMW-THz46771.2020.9370701.
223. Chen BW, Yang SX, Chen J et al. Directional terahertz holography with thermally active Janus metasurface. Light Sci Appl **12**, 136 (2023).
224. Wang GY, Wu RX, Zhang LL et al. Coherent detection of pulsed terahertz waves in solid, gaseous, and liquid media. Fundam Res **5**, 516–525 (2025).
225. Kulya MS, Petrov NV, Tcypkin AN et al. Influence of raster scan parameters on the image quality for the THz phase imaging in collimated beam with a wide aperture. J Phys Conf Ser **536**, 012010 (2014).
226. Bespalov VG, Krylov VN, Putilin SE et al. Lasing in the far IR spectral range under femtosecond optical excitation of the InAs semiconductor in a magnetic field. Opt Spectrosc **93**, 148–152 (2002).
227. Balbekin NS, Kulya MS, Rogov PY et al. The modeling peculiarities of diffractive propagation of the broadband terahertz two-dimensional field. Phys Procedia **73**, 49–53 (2015).
228. Balbekin NS, Cassar Q, Smolyanskaya OA et al. Terahertz pulse time-domain holography method for phase imaging of breast tissue. Proc SPIE **10887**, 108870G (2019).
229. Pariente G, Gallet V, Borot A et al. Space–time characterization of ultra-intense femtosecond laser beams. Nat Photonics **10**, 547–553 (2016).
230. Borot A, Quéré F. Spatio-spectral metrology at focus of ultrashort lasers: a phase-retrieval approach. Opt Express **26**, 26444–26461 (2018).
231. Sheridan JT, Kostuk RK, Gil AF et al. Roadmap on holography. J Opt **22**, 123002 (2020).
232. Tsiplakova EG, Kulya MS, Gorodetsky A et al. Interference enabled binary data encoding within broadband uniformly topologically charged terahertz beams. In *Digital Holography and Three-*

Dimensional Imaging DTh5C. 5 (Optica Publishing Group, 2021). http://doi.org/10.1364/DH.2021.DTh5C.5.
233. Nikolaev DA, Tsysar SA, Khokhlova VA et al. Holographic extraction of plane waves from an ultrasound beam for acoustic characterization of an absorbing layer of finite dimensions. *J Acoust Soc Am* **149**, 386–404 (2021).
234. Edgar MP, Gibson GM, Padgett MJ. Principles and prospects for single-pixel imaging. *Nat Photonics* **13**, 13–20 (2019).
235. Schori A, Shwartz S. X-ray ghost imaging with a laboratory source. *Opt Express* **25**, 14822–14828 (2017).
236. Yu H, Lu RH, Han SS et al. Fourier-transform ghost imaging with hard X rays. *Phys Rev Lett* **117**, 113901 (2016).
237. Greenberg J, Krishnamurthy K, Brady D. Compressive single-pixel snapshot x-ray diffraction imaging. *Opt Lett* **39**, 111–114 (2014).
238. Radwell N, Mitchell KJ, Gibson GM et al. Single-pixel infrared and visible microscope. *Optica* **1**, 285–289 (2014).
239. Edgar MP, Gibson GM, Bowman RW et al. Simultaneous real-time visible and infrared video with single-pixel detectors. *Sci Rep* **5**, 10669 (2015).
240. Zanotto L, Piccoli R, Dong JL et al. Single-pixel terahertz imaging: a review. *Opto-Electronic Adv* **3**, 200012 (2020).
241. Chen SC, Du LH, Zhu LG. THz wave computational ghost imaging: principles and outlooks. *Opto-Electronic Eng* **47**, 200024 (2020).
242. Shapiro JH. Computational ghost imaging. *Phys Rev A* **78**, 061802 (2008).
243. Pittman TB, Shih YH, Strekalov DV et al. Optical imaging by means of two-photon quantum entanglement. *Phys Rev A* **52**, R3429–R3432 (1995).
244. Bennink RS, Bentley SJ, Boyd RW. "Two-photon" coincidence imaging with a classical source. *Phys Rev Lett* **89**, 113601 (2002).
245. Duarte MF, Davenport MA, Takhar D et al. Single-pixel imaging via compressive sampling. *IEEE Sign Proc Mag* **25**, 83–91 (2008).
246. Dudley D, Duncan WM, Slaughter J. Emerging digital micromirror device (DMD) applications. *Proc SPIE* **4985**, 14–25 (2003).
247. Candès EJ, Romberg J, Tao T. Robust uncertainty principles: exact signal reconstruction from highly incomplete frequency information. *IEEE Trans Inf Theory* **52**, 489–509 (2006).
248. Candes EJ, Tao T. Near-optimal signal recovery from random projections: universal encoding strategies. *IEEE Trans Inf Theory* **52**, 5406–5425 (2006).
249. Donoho DL. Compressed sensing. *IEEE Trans Inf Theory* **52**, 1289–1306 (2006).
250. Chan WL, Charan K, Takhar D et al. A single-pixel terahertz imaging system based on compressed sensing. *Appl Phys Lett* **93**, 121105 (2008).
251. Gatesman AJ, Danylov A, Goyette TM et al. Terahertz behavior of optical components and common materials. *Proc SPIE* **6212**, 62120E (2006).
252. Liang GZ, Liu T, Wang QJ. Recent developments of terahertz quantum cascade lasers. *IEEE J Sel Top Quant Electr* **23**, 1200118 (2017).
253. Zhong K, Shi W, Xu DG et al. Optically pumped terahertz sources. *Sci Chin Technol Sci* **60**, 1801–1818 (2017).
254. Neu J, Schmuttenmaer CA. Tutorial: an introduction to terahertz time domain spectroscopy (THz-TDS). *J Appl Phys* **124**, 231101 (2018).
255. Cherkasova O, Vrazhnov D, Knyazkova A et al. Terahertz time-domain spectroscopy of glioma patient blood plasma: diagnosis and treatment. *Appl Sci* **13**, 5434 (2023).
256. Zhang Y, Han J, Wang D et al. Application of THz time-domain spectroscopy to diagnose gastric cancer tissues in surgical resected specimens. *J Infrared, Millimeter, Terahertz Waves* **42**, 802–812 (2021).
257. Fan WH, Burnett A, Upadhya PC et al. Far-infrared spectroscopic characterization of explosives for security applications using broadband terahertz time-domain spectroscopy. *Appl Spectr* **61**, 638–643 (2007).
258. Choi J, Ryu SY, Kwon WS et al. Compound explosives detection and component analysis via terahertz time-domain spectroscopy. *J Opt Soc Kor* **17**, 454–460 (2013).
259. Kong SG, Wu DH. Terahertz time-domain spectroscopy for explosive trace detection. In *2006 IEEE International Conference on Computational Intelligence for Homeland Security and Personal Safety* 47–50 (IEEE, 2006). http://doi.org/10.1109/CIHSPS.2006.313311.
260. Ferguson B, Zhang XC. Materials for terahertz science and technology. *Nat Mater* **1**, 26–33 (2002).
261. Rogalin VE, Kaplunov IA, Kropotov GI. Optical materials for the THz range. *Opt Spectr* **125**, 1053–1064 (2018).
262. Oka A, Tominaga K. Terahertz spectroscopy of polar solute molecules in non-polar solvents. *J Non-Crystall Sol* **352**, 4606–4609 (2006).
263. Krotkus A. Semiconductors for terahertz photonics applications. *J Phys D Appl Phys* **43**, 273001 (2010).
264. Leibov L, Ismagilov A, Zalipaev V et al. Speckle patterns formed by broadband terahertz radiation and their applications for ghost imaging. *Sci Rep* **11**, 20071 (2021).
265. Ismagilov A, Lappo-Danilevskaya A, Grachev Y et al. Ghost imaging via spectral multiplexing in the broadband terahertz range. *J Opt Soc Am B* **39**, 2335–2340 (2022).
266. Gray AX, Hoffmann MC, Jeong J et al. Ultrafast terahertz field control of electronic and structural interactions in vanadium dioxide. *Phys Rev B* **98**, 045104 (2018).
267. Shen H, Gan L, Newman N et al. Spinning disk for compressive imaging. *Opt Lett* **37**, 46–48 (2012).
268. Zhang ZB, Wang XY, Zheng GA et al. Hadamard single-pixel imaging versus Fourier single-pixel imaging. *Opt Express* **25**, 19619–19639 (2017).
269. Hillger P, Grzyb J, Jain R et al. Terahertz imaging and sensing applications with silicon-based technologies. *IEEE Trans Terahertz Sci Technol* **9**, 1–19 (2019).
270. Bergen MH, Holzman JF. Terahertz time-domain spectroscopy for ultrafast and quasi-static characterizations of germanium. *IEEE Trans Terahertz Sci Technol* **11**, 54–61 (2021).
271. Kaplunov IA, Kolesnikov AI, Kropotov GI et al. Optical properties of single-crystal germanium in the THz Range. *Opt Spectr* **126**, 191–194 (2019).
272. Cavalleri A, Tóth C, Siders CW et al. Femtosecond structural dynamics in VO_2 during an ultrafast solid-solid phase transition. *Phys Rev Lett* **87**, 237401 (2001).
273. Havaux M, Bonfils JP, Lütz C et al. Photodamage of the photosynthetic apparatus and its dependence on the leaf developmental stage in the npq1 Arabidopsis mutant deficient in the xanthophyll cycle enzyme violaxanthin de-epoxidase. *Plant Physiol* **124**, 273–284 (2000).
274. Zanotto L, Balistreri G, Rovere A et al. Terahertz scanless hypertemporal imaging. *Laser Photonics Rev* **17**, 2200936 (2023).
275. Teo SM, Ofori-Okai BK, Werley CA et al. Single-shot THz detec-

tion techniques optimized for multidimensional THz spectroscopy. *Rev Sci Instrum* **86**, 051301 (2015).

276. Liang JX, Zhang JQ, Wang ZH et al. Photoactive polymer-silicon heterostructures for terahertz spatial light modulation and video-rate single-pixel compressive imaging. *Adv Funct Mater* **35**, 2422478 (2025).
277. Huber AJ, Keilmann F, Wittborn J et al. Terahertz near-field nanoscopy of mobile carriers in single semiconductor nanodevices. *Nano Lett* **8**, 3766–3770 (2008).
278. Cocker TL, Jelic V, Gupta M et al. An ultrafast terahertz scanning tunnelling microscope. *Nat Photonics* **7**, 620–625 (2013).
279. Kawano Y, Ishibashi K. An on-chip near-field terahertz probe and detector. *Nat Photonics* **2**, 618–621 (2008).
280. Stantchev RI, Phillips DB, Hobson P et al. Compressed sensing with near-field THz radiation. *Optica* **4**, 989–992 (2017).
281. Chen SC, Du LH, Meng K et al. Terahertz wave near-field compressive imaging with a spatial resolution of over λ/100. *Opt Lett* **44**, 21–24 (2019).
282. Gavini A, Kwan CCY. Optical properties of semiconducting VO_2 films. *Phys Rev B* **5**, 3138 (1972).
283. She RB, Liu WQ, Lu YF et al. Fourier single-pixel imaging in the terahertz regime. *Appl Phys Lett* **115**, 021101 (2019).
284. Weis P, Garcia-Pomar JL, Höh M et al. Spectrally wide-band terahertz wave modulator based on optically tuned graphene. *ACS Nano* **6**, 9118–9124 (2012).
285. Zhang ZB, Ma X, Zhong JG. Single-pixel imaging by means of Fourier spectrum acquisition. *Nat Commun* **6**, 6225 (2015).
286. Zhang ZB, Wang XY, Zheng GA et al. Fast Fourier single-pixel imaging via binary illumination. *Sci Rep* **7**, 12029 (2017).
287. Yang XY, Tian Z, Chen XY et al. Terahertz single-pixel near-field imaging based on active tunable subwavelength metallic grating. *Appl Phys Lett* **116**, 241106 (2020).
288. Novitsky A, Ivinskaya AM, Zalkovskij M et al. Non-resonant terahertz field enhancement in periodically arranged nanoslits. *J Appl Phys* **112**, 074318 (2012).
289. Shi SF, Zeng B, Han HL et al. Optimizing broadband terahertz modulation with hybrid graphene/metasurface structures. *Nano Lett* **15**, 372–377 (2015).
290. Olivieri L, Totero Gongora JS, Pasquazi A et al. Time-resolved nonlinear ghost imaging. *ACS Photonics* **5**, 3379–3388 (2018).
291. Olivieri L, Gongora JST, Peters L et al. Hyperspectral terahertz microscopy via nonlinear ghost imaging. *Optica* **7**, 186–191 (2020).
292. Olivieri L, Peters L, Cecconi V et al. Terahertz nonlinear ghost imaging via plane decomposition: toward near-field micro-volumetry. *ACS Photonics* **10**, 1726–1734 (2023).
293. Chen SC, Feng Z, Li J et al. Ghost spintronic THz-emitter-array microscope. *Light Sci Appl* **9**, 99 (2020).
294. Valenzuela SO, Tinkham M. Direct electronic measurement of the spin Hall effect. *Nature* **442**, 176–179 (2006).
295. Sinova J, Valenzuela SO, Wunderlich J et al. Spin hall effects. *Rev Mod Phys* **87**, 1213–1260 (2015).
296. Seifert T, Jaiswal S, Martens U et al. Efficient metallic spintronic emitters of ultrabroadband terahertz radiation. *Nat Photonics* **10**, 483–488 (2016).
297. Zhao JP, E YW, Williams K et al. Spatial sampling of terahertz fields with sub-wavelength accuracy via probe-beam encoding. *Light Sci Appl* **8**, 55 (2019).
298. Shen YC, Gan L, Stringer M et al. Terahertz pulsed spectroscopic imaging using optimized binary masks. *Appl Phys Lett* **95**, 231112 (2009).
299. Jin YS, Jeon SG, Kim GJ et al. Fast scanning of a pulsed terahertz signal using an oscillating optical delay line. *Rev Sci Instrum* **78**, 023101 (2007).
300. Guerboukha H, Markov A, Qu H et al. Time resolved dynamic measurements at THz frequencies using a rotary optical delay line. *IEEE Trans Terahertz Sci Technol* **5**, 564–572 (2015).
301. Zhai ZH, Zhong SC, Li J et al. Time-resolved single-shot terahertz time-domain spectroscopy for ultrafast irreversible processes. *Rev Sci Instrum* **87**, 095101 (2016).
302. Couture N, Cui W, Lippl M et al. Single-pulse terahertz spectroscopy monitoring sub-millisecond time dynamics at a rate of 50 kHz. *Nat Commun* **14**, 2595 (2023).
303. Vaz PG, Amaral D, Requicha Ferreira LF et al. Image quality of compressive single-pixel imaging using different Hadamard orderings. *Opt Express* **28**, 11666–11681 (2020).
304. Yu WK. Super sub-Nyquist single-pixel imaging by means of cake-cutting Hadamard basis sort. *Sensors* **19**, 4122 (2019).
305. Chen XY, Li J, Du LH et al. Near-field terahertz single-pixel imaging with ultralow sampling ratio. *Opt Express* **32**, 35126–35138 (2024).
306. Li CB, Yin WT, Jiang H et al. An efficient augmented Lagrangian method with applications to total variation minimization. *Comput Optim Appl* **56**, 507–530 (2013).
307. Higham CF, Murray-Smith R, Padgett MJ et al. Deep learning for real-time single-pixel video. *Sci Rep* **8**, 2369 (2018).
308. Rizvi S, Cao J, Zhang KY et al. Deringing and denoising in extremely under-sampled Fourier single pixel imaging. *Opt Express* **28**, 7360–7374 (2020).
309. Long ZY, Wang TY, You CW et al. Terahertz image super-resolution based on a deep convolutional neural network. *Appl Opt* **58**, 2731–2735 (2019).
310. Wang Y, Qi F, Wang JK. Terahertz image super-resolution based on a complex convolutional neural network. *Opt Lett* **46**, 3123–3126 (2021).
311. Zhu YS, Liu SJ, Wang XM et al. Deep learning empowered sub-diffraction terahertz backpropagation single-pixel imaging. *ACS Photonics* **12**, 5453–5463 (2025).
312. Cocker TL, Jelic V, Hillenbrand R et al. Nanoscale terahertz scanning probe microscopy. *Nat Photonics* **15**, 558–569 (2021).
313. Guo X, Bertling K, Donose BC et al. Terahertz nanoscopy: advances, challenges, and the road ahead. *Appl Phys Rev* **11**, 021306 (2024).
314. Zhao ZC, Kravtsov V, Wang ZR et al. Applications of ultrafast nano-spectroscopy and nano-imaging with tip-based microscopy. *eLight* **5**, 1 (2025).
315. Astratov VN, Ben Sahel Y, Eldar YC et al. Roadmap on label-free super-resolution imaging. *Laser Photonics Rev* **17**, 2200029 (2023).
316. Zinov'ev NN, Andrianov AV, Gallant AJ et al. Contrast and resolution enhancement in a confocal terahertz video system. *JETP Lett* **88**, 492–495 (2008).
317. Zhao Y, Chen Q, Zhou SH et al. Super-resolution imaging through scattering medium based on parallel compressed sensing. *IEEE Photonics J* **9**, 7803012 (2017).
318. Yoxall E, Schnell M, Nikitin AY et al. Direct observation of ultraslow hyperbolic polariton propagation with negative phase velocity. *Nat Photonics* **9**, 674–678 (2015).
319. Ni GX, McLeod AS, Sun Z et al. Fundamental limits to graphene

plasmonics. *Nature* **557**, 530–533 (2018).
320. Ma WL, Hu GW, Hu DB et al. Ghost hyperbolic surface polaritons in bulk anisotropic crystals. *Nature* **596**, 362–366 (2021).
321. Schnell M, Alonso-González P, Arzubiaga L et al. Nanofocusing of mid-infrared energy with tapered transmission lines. *Nat Photonics* **5**, 283–287 (2011).
322. Yakubovsky DI, Grudinin DV, Ermolaev GA et al. Optical nanoimaging of surface plasmon polaritons supported by ultrathin metal films. *Nano Lett* **23**, 9461–9467 (2023).
323. Menabde SG, Lee IH, Lee S et al. Real-space imaging of acoustic plasmons in large-area graphene grown by chemical vapor deposition. *Nat Commun* **12**, 938 (2021).
324. Nikitin AY, Alonso-González P, Vélez S et al. Real-space mapping of tailored sheet and edge plasmons in graphene nanoresonators. *Nat Photonics* **10**, 239–243 (2016).
325. Lebsir Y, Boroviks S, Thomaschewski M et al. Ultimate limit for optical losses in gold, revealed by quantitative near-field microscopy. *Nano Lett* **22**, 5759–5764 (2022).
326. Bylinkin A, Schnell M, Autore M et al. Real-space observation of vibrational strong coupling between propagating phonon polaritons and organic molecules. *Nat Photonics* **15**, 197–202 (2021).
327. Wang YY, Johnson SC, Nookala N et al. Tip-enhanced imaging and control of infrared strong light-matter interaction. *Laser Photonics Rev* **18**, 2301148 (2024).
328. Govyadinov AA, Mastel S, Golmar F et al. Recovery of permittivity and depth from near-field data as a step toward infrared nanotomography. *ACS Nano* **8**, 6911–6921 (2014).
329. Mastel S, Govyadinov AA, Maissen C et al. Understanding the image contrast of material boundaries in IR nanoscopy reaching 5 nm spatial resolution. *ACS Photonics* **5**, 3372–3378 (2018).
330. Hillenbrand R, Abate Y, Liu MK et al. Visible-to-THz near-field nanoscopy. *Nat Rev Mater* **10**, 285–310 (2025).
331. Betzig E, Trautman JK. Near-field optics: microscopy, spectroscopy, and surface modification beyond the diffraction limit. *Science* **257**, 189–195 (1992).
332. Mester L, Govyadinov AA, Chen S et al. Subsurface chemical nanoidentification by nano-FTIR spectroscopy. *Nat Commun* **11**, 3359 (2020).
333. Chen XZ, Hu DB, Mescall R et al. Modern scattering-type scanning near-field optical microscopy for advanced material research. *Adv Mater* **31**, 1804774 (2019).
334. Synge EH. A suggested method for extending microscopic resolution into the ultra-microscopic region. *Philos Mag* **6**, 356–362 (1928)
335. Lu YZ, Hale LL, Zaman AM et al. Near-field spectroscopy of individual asymmetric split-ring terahertz resonators. *ACS Photonics* **10**, 2832–2838 (2023).
336. Hale LL, Keller J, Siday T et al. Near-field terahertz spectroscopy: noninvasive near-field spectroscopy of single subwavelength complementary resonators. *Laser Photonics Rev* **14**, 2070022 (2020).
337. Ash EA, Nicholls G. Super-resolution aperture scanning microscope. *Nature* **237**, 510–512 (1972).
338. Bitzer A, Merbold H, Thoman A et al. Terahertz near-field imaging of electric and magnetic resonances of a planar metamaterial. *Opt Express* **17**, 3826–3834 (2009).
339. Acuna G, Heucke SF, Kuchler F et al. Surface plasmons in terahertz metamaterials. *Opt Express* **16**, 18745–18751 (2008).
340. Mitrofanov O, Khromova I, Siday T et al. Near-field spectroscopy and imaging of subwavelength plasmonic terahertz resonators. *IEEE Trans Terahertz Sci Technol* **6**, 382–388 (2016).
341. Van Hoof NJJ, Abujetas DR, Ter Huurne SET et al. Unveiling the symmetry protection of bound states in the continuum with terahertz near-field imaging. *ACS Photonics* **8**, 3010–3016 (2021).
342. Ter Huurne S, Abujetas DR, Van Hoof N et al. Direct observation of lateral field confinement in symmetry-protected THz bound states in the continuum. *Adv Opt Mater* **11**, 2202403 (2023).
343. Wächter M, Nagel M, Kurz H. Tapered photoconductive terahertz field probe tip with subwavelength spatial resolution. *Appl Phys Lett* **95**, 041112 (2009).
344. Li ZX, Yan SH, Zang ZY et al. Single cell imaging with near-field terahertz scanning microscopy. *Cell Proliferation* **53**, e12788 (2020).
345. Geng GS, Dai GB, Li DD et al. Imaging brain tissue slices with terahertz near-field microscopy. *Biotechnol Prog* **35**, e2741 (2019).
346. Wang YY, Zhang TY, Ma K et al. Terahertz nanoscopy on low-dimensional materials: toward ultrafast physical phenomena. *ACS Appl Mater Interfaces* **17**, 2736–2755 (2025).
347. Guo X, He X, Degnan Z et al. Terahertz nanospectroscopy of plasmon polaritons for the evaluation of doping in quantum devices. *Nanophotonics* **12**, 1865–1875 (2023).
348. Tranca DE, Stanciu SG, Hristu R et al. Nanoscale mapping of refractive index by using scattering-type scanning near-field optical microscopy. *Nanomed Nanotechnol Biol Med* **14**, 47–50 (2018).
349. Stanciu SG, Tranca DE, Pastorino L et al. Characterization of nanomaterials by locally determining their complex permittivity with scattering-type scanning near-field optical microscopy. *ACS Appl Nano Mater* **3**, 1250–1262 (2020).
350. Stinson HT, Sternbach A, Najera O et al. Imaging the nanoscale phase separation in vanadium dioxide thin films at terahertz frequencies. *Nat Commun* **9**, 3604 (2018).
351. Yang ZB, Tang DY, Hu J et al. Near-field nanoscopic terahertz imaging of single proteins. *Small* **17**, 2005814 (2021).
352. Ma PC, Kölbel J, Pizzuto A et al. Terahertz near-field imaging for buried structures. In *The 48th International Conference on Infrared, Millimeter, and Terahertz Waves* 1–2 (IEEE, 2023). http://doi.org/10.1109/IRMMW-THz57677.2023.10299085.
353. Taubner T, Keilmann F, Hillenbrand R. Nanoscale-resolved subsurface imaging by scattering-type near-field optical microscopy. *Opt Express* **13**, 8893–8899 (2005).
354. Jing R, Shao Y, Fei Z et al. Terahertz response of monolayer and few-layer WTe2 at the nanoscale. *Nat. Commun* 1**2**, 5594 (2021).
355. Zhang JW, Chen XZ, Mills S et al. Terahertz nanoimaging of graphene. *ACS Photonics* **5**, 2645–2651 (2018).
356. Zhang XQY, Zhang X, Zhang ZC et al. Time-domain-filtered terahertz nanoscopy of intrinsic light-matter interactions. *Nano Lett* **24**, 15008–15015 (2024).
357. Sulollari N, Keeley J, Park S et al. Coherent terahertz microscopy of modal field distributions in micro-resonators. *APL Photonics* **6**, 066104 (2021).
358. Thomas L, Hannotte T, Santos CN et al. Imaging of THz photonic modes by scattering scanning near-field optical microscopy. *ACS Appl Mater Interfaces* **14**, 32608–32617 (2022).
359. Hale LL, Siday T, Mitrofanov O. Near-field imaging and spectroscopy of terahertz resonators and metasurfaces [invited]. *Opt Mater Express* **13**, 3068–3086 (2023).
360. Alonso-González P, Nikitin AY, Gao YD et al. Acoustic terahertz graphene plasmons revealed by photocurrent nanoscopy. *Nat Nanotechnol* **12**, 31–35 (2017).

361. Chen S, Bylinkin A, Wang ZTY et al. Real-space nanoimaging of THz polaritons in the topological insulator Bi_2Se_3. *Nat Commun* **13**, 1374 (2022).
362. Chen S, Leng PL, Konečná A et al. Real-space observation of ultraconfined in-plane anisotropic acoustic terahertz plasmon polaritons. *Nat Mater* **22**, 860–866 (2023).
363. Duan JH, Chen JN. Recent progress of near-field studies of two-dimensional polaritonics. *Acta Phys Sin* **68**, 110701 (2019).
364. Zhang A, Lei L, Cheng L et al. Terahertz imaging detects oral cariogenic microbial domains characteristics. *J Dental Res* **103**, 1428–1436 (2024).
365. Wang J, Peng L, Han DX et al. Label-free detection and identification of single bacteria via terahertz near-field imaging. *Front Microbiol* **14**, 1195448 (2023).
366. Xiao F, Zhang XQY, Xu XX et al. Unveiling enamel demineralization mechanisms by sensitive dielectric differentiation based on terahertz nanospectroscopy. *Biomed Opt Express* **15**, 5229–5237 (2024).
367. Zhou J, Zhang XQY, Xu XX et al. Single-bacterium diagnosis via terahertz near-field dielectric nanoimaging. *ACS Appl Mater Interfaces* **17**, 18074–18082 (2025).
368. Liewald C, Mastel S, Hesler J et al. All-electronic terahertz nanoscopy. *Optica* **5**, 159–163 (2018).
369. Tang F, Zhong QY, Zhang XQY et al. Angle-controlled nanospectrum switching from Lorentzian to Fano lineshapes. *Nanomaterials* **14**, 1932 (2024).
370. Xiao F, Zhang XQY, Wang YY et al. Angle-controlled strong and weak coupling in photon molecules. *Sci Rep* **15**, 1794 (2025).
371. Yang ZB, Li DD, Chen LG et al. Near-field terahertz morphological reconstruction nanoscopy for subsurface imaging of protein layers. *ACS Nano* **18**, 10104–10112 (2024).
372. Eisele M, Cocker TL, Huber MA et al. Ultrafast multi-terahertz nano-spectroscopy with sub-cycle temporal resolution. *Nat Photonics* **8**, 841–845 (2014).
373. Siday T, Sandner F, Brem S et al. Ultrafast nanoscopy of high-density exciton phases in WSe_2. *Nano Lett* **22**, 2561–2568 (2022).
374. Pizzuto A, Castro-Camus E, Wilson W et al. Nonlocal time-resolved terahertz spectroscopy in the near field. *ACS Photonics* **8**, 2904–2911 (2021).
375. Meineke C, Schlosser J, Zizlsperger M et al. Ultrafast exciton dynamics in the atomically thin van der Waals magnet CrSBr. *Nano Lett* **24**, 4101–4107 (2024).
376. Zizlsperger M, Nerreter S, Yuan Q et al. In situ nanoscopy of single-grain nanomorphology and ultrafast carrier dynamics in metal halide perovskites. *Nat Photonics* **18**, 975–981 (2024).
377. Chen XZ, Liu X, Guo XD et al. THz Near-field imaging of extreme subwavelength metal structures. *ACS Photonics* **7**, 687–694 (2020).
378. Zhang ZC, Wang YY, Zhang XQY et al. Tip-sample interactions in terahertz scattering scanning near-field optical microscopy and its influences. *Acta Phys Sin* **70**, 248703 (2021).
379. Pizzuto A, Chen XZ, Hu H et al. Anomalous contrast in broadband THz near-field imaging of gold microstructures. *Opt Express* **29**, 15190–15198 (2021).
380. Babicheva VE, Gamage S, Stockman MI et al. Near-field edge fringes at sharp material boundaries. *Opt Express* **25**, 23935–23944 (2017).
381. Zhang ZC, Hu M, Zhang XQY et al. Direct observation of tip-gap interactions in THz scattering-type scanning near-field optical microscopy. *Appl Phys Express* **14**, 102004 (2021).

Acknowledgements

This work was supported by the National Natural Science Foundation of China (62175004, 62275175, 62588201, 62401113, 92463308, 12574421, and 12174271).

Competing interests

Yan Zhang serves as an Editor for the Journal, and no other author has reported any competing interests.

Published by Editorial Office of *Opto-Electronic Technology*, Institute of Optics and Electronics, Chinese Academy of Sciences.